Strategies for Rapid MR Imaging

A Thesis

Submitted for the Degree of

Doctor of Philosophy

in the Faculty of Engineering

by

Neelam Sinha

Department of Electrical Engineering
Indian Institute of Science
Bangalore – 560 012

April 2008

Synopsis

In MR imaging, techniques for acquisition of reduced data (Rapid MR imaging) are being explored to obtain high-quality images to satisfy the conflicting requirements of simultaneous high spatial and temporal resolution, required for functional studies. The term "rapid" is used because reduction in the volume of data acquisition leads to faster scans. The objective is to obtain high acceleration factors, since it indicates the ability of the technique to yield high-quality images with reduced data (in turn, reduced acquisition time). Reduced data acquisition in conventional (sequential) MR scanners, where a single receiver coil is used, can be achieved either by acquiring only certain k-space regions or by regularly undersampling the entire data in k-space. In parallel MR scanners, where multiple receiver coils are used to acquire high-SNR data, reduced data acquisition is typically accomplished using regular undersampling.

Optimal region selection in the $3D$ k-space (restricted to $k_y - k_z$ plane, since k_x is the readout direction) needs to satisfy "maximum energy compaction" and "minimum acquisition" requirements. In this thesis, a novel star-shaped truncation window is proposed to increase the achievable acceleration factor. The proposed window monotonically cuts down the acquisition of the number of k-space samples with lesser energy. The truncation window samples data within a star-shaped region centered around the origin in the $k_y - k_z$ plane. The missing values are extrapolated using generalized series modeling-based methods. The proposed method is applied to several real and synthetic data sets. The superior performance of the proposed method is illustrated using the standard measures of error images and uptake curve comparisons. Average values of slope error in estimating the enhancement curve are obtained over 5 real data sets of breast and abdomen images, for an acceleration factor of 8. The proposed method results in a slope error of 5%, while the values obtained using rectangular and elliptical windows are 12% and 10%, respectively.

k-t BLAST, a popular method used in cardiac and functional brain imaging, involves regular undersampling. However, the method suffers from drawbacks such as separate

training scan, blurred training estimates and aliased phase maps. In this thesis, variations to *k-t BLAST* have been proposed to overcome the drawbacks. The proposed improved *k-t BLAST* incorporates variable-density sampling scheme, phase information from the training map and utilization of generalized-series extrapolated training map. The advantage of using a variable density sampling scheme is that the training map is obtained from the actual acquisition instead of a separate pilot scan. Besides, phase information from the training map is used, in place of phase from the aliased map; generalized series extrapolated training map is used instead of the zero-padded training map, leading to better estimation of the unacquired values. The existing technique and the proposed variations are applied on real fMRI data volumes. Improvement in PSNR of activation maps of up to 10 dB. Besides, a reduction of 10% in RMSE is obtained over the entire time series of fMRI images. The peak improvement of the proposed method over *k-t BLAST* is 35%, averaged over 5 data sets.

Most image reconstruction techniques in parallel MR imaging utilize the knowledge of coil sensitivities for image reconstruction, along with assumptions of image reconstruction functions. The thesis proposes an image reconstruction technique that neither needs to estimate coil sensitivities nor makes any assumptions on the image reconstruction function. The proposed cartesian parallel imaging using neural networks, called "Composite image Reconstruction And Unaliasing using Neural Networks" (CRAUNN), is a novel approach based on the observation that the aliasing patterns remain the same irrespective of whether the *k*-space acquisition consists of only low frequencies or the entire range of *k*-space frequencies. In the proposed approach, image reconstruction is obtained using the neural network framework. Data acquisition follows a variable-density sampling scheme, where low *k*-space frequencies are densely sampled, while the rest of the *k*-space is sparsely sampled. The blurred, unaliased images obtained using the densely sampled low *k*-space data are used to train the neural network. Image is reconstructed by feeding to the trained network, the aliased images, obtained using the regularly undersampled *k*-space containing the entire range of *k*-space frequencies. The proposed approach has been applied to the Shepp-Logan phantom as well as real brain MRI data sets. A visual

error measure for estimating the image quality used in compression literature, called SSIM (Structural SIMilarity) index is employed. The average SSIM for the noisy Shepp-Logan phantom (SNR = 10 dB) using the proposed method is 0.68, while those obtained using GRAPPA and SENSE are 0.6 and 0.42, respectively. For the case of the phantom superimposed with fine grid-like structure, the average SSIM index obtained with the proposed method is 0.7, while those for GRAPPA and SENSE are 0.5 and 0.37, respectively.

Image reconstruction is more challenging with reduced data acquired using non-cartesian trajectories since aliasing introduced is not localized. Popular technique for non-cartesian parallel imaging CGSENSE suffers from drawbacks like sensitivity to noise and requirement of good coil estimates, while radial/spiral GRAPPA requires complete identical scans to obtain reconstruction kernels for specific trajectories. In our work, the proposed neural network based reconstruction method, CRAUNN, has been shown to work for general non-cartesian acquisitions such as spiral and radial too. In addition, the proposed method does not require coil estimates, or trajectory-specific customized reconstruction kernels. Experiments are performed using radial and spiral trajectories on real and synthetic data, and compared with CGSENSE. Comparison of error images shows that the proposed method has far lesser residual aliasing compared to CGSENSE. The average SSIM index for reconstructions using CRAUNN with spirally and radially undersampled data, are comparable at 0.83 and 0.87, respectively. The same measure for reconstructions using CGSENSE are 0.67 and 0.69, respectively. The average RMSE for reconstructions using CRAUNN with spirally and radially undersampled data, are comparable at 11.1 and 6.1, respectively. The same measure for reconstructions using CGSENSE are 16 and 9.18, respectively.

Acknowledgements

I express my gratitude to my advisors Dr. Manojkumar Saranathan and Prof. A. G. Ramakrishnan. I am grateful to everybody in the department for being so helpful and nice.

My heartfelt thanks, specially, to each of my lab-members for their support.

Many names that I can't even begin to enlist, my grateful thanks to all my friends who have all made my tenure at IISc so memorable.

I want to acknowledge the warmth of both my families, the one I was born into and the one I am married into.

Many thanks to all the researchers who have so unselfishly put up their codes, ideas and data on the web, for use by the research community.

Contents

List of Figures

List of Tables

Chapter 1

Introduction

1.1 Magnetic resonance imaging

Magnetic resonance imaging (MRI) is a noninvasive imaging modality which has come to be widely used in clinical practice over the past decade, for imaging the central nervous and the musculo-skeletal systems. Early MR imaging focus only on imaging the structural details of the anatomy of interest. Later on, techniques for dynamic imaging emerged to study the continuous changes in the imaged organ, as in functioning of brain, using functional MR imaging (fMRI). Of late, techniques based on diffusion of water molecules such as diffusion weighted imaging and diffusion tensor imaging have also been used to study the orientation of fine structures in the brain. Diffusion-based imaging is useful to diagnose vascular strokes, study diseases of the white matter and determine the connectivity in the brain.

MR Imaging utilizes the phenomenon of nuclear magnetic resonance (NMR) to generate 2D/3D images of the distribution of the Hydrogen protons in the subject. A typical MR scanner consists of the following :

- A large cylindrical superconducting electro-magnet that generates a homogenous steady magnetic field, whose strength is in the order of a few Tesla.

- RF coils to transmit and receive magnetic fields that oscillate at the prescribed radio

Figure 1.1: A typical clinical MR scanner (Source: [1])

frequency.

- Gradient coils to spatially distinguish the MR signals, by generating spatially varying magnetic fields.

A typical MR scanner is shown in Fig. 1.1. The subject is slid inside the bore of the magnet, causing the Hydrogen protons in various molecules such as fat, water and muscle to align with the strong field and exhibit NMR phenomenon. MRI offers rich soft-tissue contrast, unlike other medical imaging modalities such as x-ray and computed tomography. It offers great flexibility to the imaging technician, since there are a number of parameters that can be controlled, enabling selective enhancement or suppression of tissues. It also offers the flexibility of choosing arbitrary imaging planes. The main drawback of MRI is the expensive hardware, especially the superconductor magnet. Also, MRI involves scan times of several minutes, at times requiring the already suffering patient to hold breath. Due to the high strength of the magnetic field involved, subjects with metallic implants, rods and pacemakers cannot be imaged using MRI.

1.2 Nuclear magnetic resonance

MR imaging is based on the NMR phenomenon, exhibited by atoms with odd number of protons (such as Hydrogen) that possess nuclear spin angular momentum. MR technique is chiefly used to image the distribution of Hydrogen protons in the water molecules, which is abundant in living beings. The phenomenon of NMR occurs when protons such as Hydrogen (other protons that exhibit NMR are ^{19}F, ^{13}C and ^{31}P) are subjected to a strong magnetic field. The acronym NMR can be explained as :

- Nuclear (N): The spin inherent in the nucleus of elements such as ^{1}H, ^{19}F, ^{13}C and ^{31}P
- Magnetic (M): The applied strong magnetic field, typically of the order of a few Tesla
- Resonance (R): Matching the (radio) frequency of the oscillating magnetic field with the frequency of the precessing protons.

The following explanation is based on the material in [44]. A nucleus with spin can be visualized as a charged sphere that rotates about its axis, resulting in a magnetic field. Under ordinary circumstances, there is no resulting net magnetic field because the spins are randomly oriented. In the presence of a strong external magnetic field ($\mathbf{B_0} = B_0\hat{z}$, say magnitude B_0 applied along Z-axis), the spins begin to precess about the external field, with frequency that directly varies with the strength of the applied magnetic field. The spins can be shown to precess about B_0 with a characteristic frequency $\omega_0 = \gamma B_0$, called Larmor frequency, where γ is the gyromagnetic constant that depends on the nucleus type. For instance, when the applied magnetic field $\mathbf{B_0}$ is 1.5T, then the Hydrogen protons have a precessional frequency of 63 MHz. A phenomenon called Zeeman effect is observed, wherein some of the spins align along the applied magnetic field $\mathbf{B_0}$, whereas the remaining spins align against it. The split in the number of spins aligning along and against the applied field is governed by Boltzmann's distribution. The spins aligned along

the applied field are slightly more in population and at a lower energy level compared to those aligned against. The energy gap between the two levels is given by $\Delta E = h\frac{\gamma \mathbf{B_0}}{\mathbf{2}\pi}$, where h is Planck's constant.

The difference in energy levels corresponds to the Larmor frequency of the precessing protons. The difference in the population of spins gives rise to a net magnetic field M along the direction of the applied magnetic field (which happens to be along Z-axis here). This is the NMR signal, which depends on the strength of the applied magnetic field B_0 as well as the proton density. At equilibrium, it is given by, $M = \frac{N\gamma^2 h^2 I_z(I_z+1)}{3kT}$, where N is the number of nuclear spins per unit volume and I_z is the spin operator. The evolution of $M(t)$ in the presence of a time-varying magnetic field B(t) is given by the Bloch equation, $\frac{dM(t)}{dt} = \gamma M(t) \times B$.

1.2.1 RF perturbation

A second applied magnetic field $\mathbf{B_1} = B_1\hat{x}$, that oscillates at the Larmor frequency ω_0, brings about resonance in the system, tipping the net magnetization M away from its equilibrium position, towards the XY plane. According to the Bloch equation, $M(t)$ precesses around $(B_1 + B_0)$ (see Fig. 1.2). An easier way to conceptualize this is to use a rotating reference frame that rotates about the Z-axis at the Larmor frequency. In this frame, M(t) executes a precession about B_1 which is essentially a simple rotation. This results in a net magnetization in the XY plane. The phenomenon is that of resonance; the energy required to be applied to bring about a change in the system is the same as the energy difference between the states. An RF coil placed in the XY plane will be induced with a voltage due to the rotating magnetic field. As per the principles of quantum mechanics, the application of the RF field results in equalizing the population of spins in the two directions resulting in zero net field along Z-axis. The RF field is applied only for a short duration and hence often referred to as a RF pulse. The net magnetization M along the XY plane can be modified both spatially and temporally using external time-varying

magnetic fields and is the basis of MRI. Hence M(**r**,t) is a more appropriate notation, where **r** is either a two-dimensional vector for planar imaging, or a three-dimensional vector for volumetric imaging. M(**r**,t) can be resolved into two components, longitudinal magnetization $M_z(t)$ and the transverse magnetization $M_{xy}(t)$. After the application of the oscillating magnetic field $B_1(t)$, it can be seen that the longitudinal component $M_z(t)$ vanishes and only the rotating field $M_{xy}(t)$ remains. In Fig. 1.2, the rotation of M(t) is shown about the Z-axis. The angle of rotation is called the tip or flip angle, which depends on the strength and the duration of $B_1(t)$. The RF coil, which can be used for excitation as well as reception, will record a signal oscillating at the Larmor frequency, induced by M(t) precessing in XY-plane. This phase of perturbation is followed by relaxation after the RF magnetic field is switched off. As time goes by, the signal strength begins to decay, due to the inherent relaxation mechanisms. This decaying signal, called Free Induction Decay (FID) signal, is collected by the MR scanner. The following section describes how the system relaxes in two different ways in order to restore equilibrium.

1.2.2 Relaxation

Of the relaxation mechanisms, the longitudinal or spin-lattice relaxation is responsible for the restoration of longitudinal magnetization $M_z(t)$ to its equilibrium value. The recovery can be modeled as an exponential with time constant T_1. The equation governing this behavior as a function of time is given by, $M_z(t) = M_0(1-e^{\frac{-t}{T_1}})$, where M_0 is the initial magnetization. In other words, T_1 is the time taken by the longitudinal magnetization (M_z) to change by the factor e. The second relaxation mechanism is due to the dephasing of the spins caused by non-uniformities in the main magnetic field. The received signal decays exponentially whose time constant is denoted as T_2 . This relaxation mechanism is called transverse or spin-spin relaxation. This time constant describes the return to equilibrium of the transverse magnetization, M_{xy}, and is given by $M_{xy} = M_{xy_0}e^{(\frac{-t}{T_2})}$. However, in real situations, the parameter encountered is ${T_2}^*$, which includes dephasing

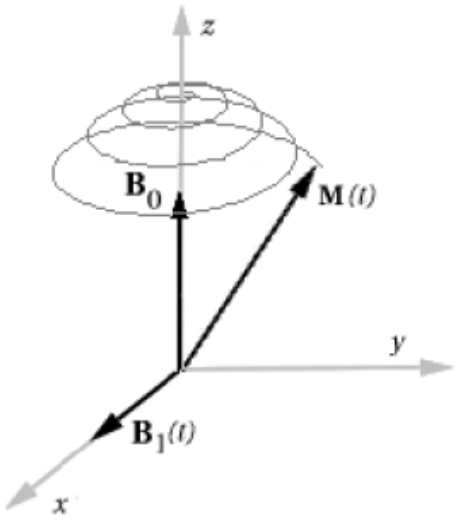

Figure 1.2: Illustration of tipping of the longitudinal magnetization vector M by the oscillating magnetic field B_1. B_0 is the static strong magnetic field

caused by both magnetic field inhomogeneities and susceptibility effects. This also causes variations in the magnetic field experienced by nuclear spins. This changes their frequency of precession even more, and they move out of phase much faster leading to faster loss of signal, and hence ${T_2}^* < T_2$.

Thus, a magnet with good field homogeneity will allow ${T_2}^*$ values to be closer to the true T_2 values of tissues. A magnet with poor field homogeneity will cause ${T_2}^*$ to be much shorter than T_2, causing faster-decaying signal intensity and affecting image contrast. Besides, it also turns out that T_2 is always less than or equal to T_1, since the T_2 relaxation process also depends on the z-component field fluctuations. The net magnetization in the XY-plane goes to zero and then the longitudinal magnetization grows till it reaches M_0 along Z-axis. Both T_1 and T_2 are different for various types of tissues and are both manipulated, along with proton density, to generate contrast in MR images. Typical values of these parameters are tabulated in Table 1.1 [3].

1.3 Imaging

Table 1.1: Values of mean proton density, T_1 and T_2 relaxation times for different tissues (Source: [3])

Tissue	Proton density	T_1(ms)	T_2(ms)
CSF	1.0	2400	500
Gray Matter	0.85	920	100
White Matter	0.7	780	90
Adipose Head	1.23	260	85
Adipose Abdomen	1.54	260	85
Spleen	1.15	780	62
Kidney	0.99	650	58
Liver	1.0	490	43
Tumor	1.0	500	100

In MR imaging, spatial localization is achieved by applying linear magnetic field gradients. To select a slice of interest along the Z direction, a gradient called slice selection gradient is applied, which varies linearly as a function of position along Z. Since the Larmor frequency is a function of the local $B(z)$ field, this will result in a linear distribution of Larmor frequencies of the spins which are extracted using a simple Fourier transform (FT). The RF excitation pulses are also tailored to excite this precise frequency range (which is dependent on the slice thickness). This is the basis of $1D$ localization. Similarly, to localize in $2D$ (i.e. plane) gradients are applied along X and Y axes usually referred to as readout and phase encoding gradients, respectively. The pre-FT raw signal is often referred to as k-space signal, since it is in the k-domain (space of Fourier transform of the image). The sequence in Fig. 1.3 illustrates the accumulation of k-space samples and the subsequent processing to obtain the desired image.

1.3.1 Image contrast

The MR physical parameters such as proton density, T_1 and T_2 values that distinguish between tissues have previously been discussed. These differences can be accentuated using imaging sequences, the principal parameters of which are briefed below.

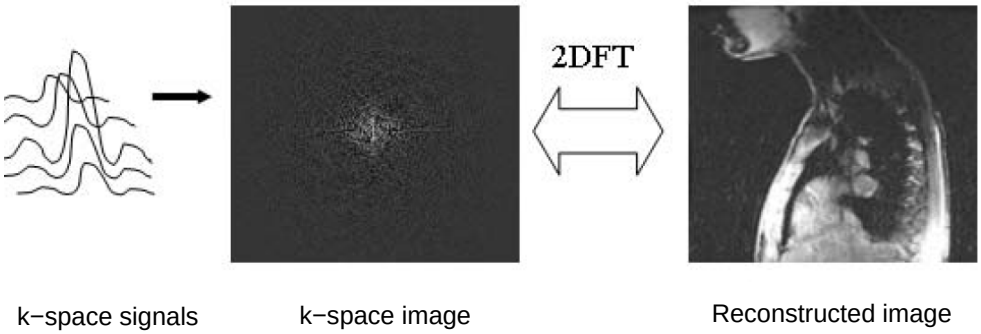

Figure 1.3: $1D$ k-space signals accumulated and Fourier transformed to result in the desired image. (Source : [62])

- θ : This is the excitation tip angle, and refers to the angle by which the longitudinal magnetization vector tips towards the XY-plane. RF pulses are designed to create specific values of tip-angles depending on the application.

- TE : TE stands for the gradient echo time. This is the time taken by the spins in the XY-plane to reverse in direction. Typically, the resulting image represents the magnitude of the transverse magnetization at the time of the gradient echo when the origin of k-space is sampled.

- TR : TR is the repetition time. The time taken from the start of the RF pulse to the end of data acquisition (i.e. time to read the FID) is called TR. Typical readout durations vary from 5 -10 ms depending on the number of samples and the sampling bandwidth. TR is one of the critical factors, which determine the total scan time of image.

The values of the parameters discussed above can be manipulated by the operator in order to highlight the source of contrast that would prove most beneficial for a given application. The most-commonly used weightings in MR imaging are :

T_1-weighted imaging utilizes the difference between the spin-lattice relaxation times of two materials by pinning the 90 degree RF signal to an adequate time interval (TR,

repetition time) that facilitates signal detection when the difference between the two T_1 relaxation curves is maximal.

T_2-weighted imaging utilizes the difference between the spin-lattice relaxation times of two materials by pinning the 180 degree RF echo signal to an adequate time interval (TE, time to echo) that facilitates signal detection when the difference between the two T_2 relaxation curves is maximal.

Proton density weighted imaging utilizes the difference in proton densities of two materials and is utilized when T_1 and T_2 characteristics are similar. By suppressing the signal effects of T_1 and T_2 similarities, signal strength disparities are isolated to proton density differences.

The combination of RF pulses and gradient pulses that form the basis of MRI is referred to as a pulse sequence. There are various types of pulse sequences such as spin-echo sequence and gradient-echo sequence, depending upon the application of MR imaging.

1.4 Signal interpretation

The received signal $s_r(t)$ is derived from the contributions of all precessing transverse magnetization in the volume.

$$s_r(t) = \int_x \int_y \int_z M(x, y, z, t) dx dy dz \tag{1.1}$$

Ignoring constant phase factors, gain factors and the relaxation term, we arrive at,

$$s(t) = \int_x \int_y m(x, y) e^{-i2\pi[k_x(t)x + k_y(t)y]} dx dy \tag{1.2}$$

Here, $m(x, y)$ is the total planar magnetization within the excited z-slice, and $k_x(t)$ and

$k_y(t)$ are the time integrals of the gradient waveforms, given by,

$$\begin{aligned} k_x(t) &= \tfrac{\gamma}{2\pi}\int_0^t G_x(\tau)d\tau \\ k_y(t) &= \tfrac{\gamma}{2\pi}\int_0^t G_y(\tau)d\tau \end{aligned}$$

Also we know that,

$$\mathcal{M}(k_x, k_y) = \int_x \int_y m(x,y)e^{-i2\pi(k_x x + k_y y)}dxdy \tag{1.3}$$

Comparing Eq. (1.2) with Eq. (1.3), we find the most important relationship in MR imaging. At any time t, $s(t)$ equals the value of the $2D$ Fourier transform of $m(x,y)$ at some spatial frequency, given by :

$$s(t) = \mathcal{M}\left(k_x(t), k_y(t)\right) \tag{1.4}$$

The total recorded signal $s(t)$ maps directly to a trajectory through spatial frequency space (k-space) as determined by the time-integrals of the applied gradient waveforms $G_x(t)$ and $G_y(t)$, given by :

$$s(t) = \mathcal{M}\left(\frac{\gamma}{2\pi}\int_0^t G_x(\tau)d\tau, \frac{\gamma}{2\pi}\int_0^t G_y(\tau)d\tau\right) \tag{1.5}$$

Hence by applying suitable gradients, we can maneuver through k-space along the trajectory $k(t)$ to collect Fourier data samples. Once a sufficient number of samples are acquired, the object image can be reconstructed by taking inverse Fourier transform of the k-space data. In theory, the entire spatial frequency information of the object can be read out in one shot. In practice, it is limited by the effects of relaxation discussed previously.

1.4.1 Field of view (FOV)

FOV is the area that contains the object to be imaged. The smaller the FOV, the higher the resolution and the smaller the voxel size but the lower the measured signal. The criterion for sampling k-space must be such that the required FOV is the most faithful representation of the corresponding area of the object being imaged. The constraints on sampling are most easily explained for the case of Cartesian sampling, where k-space is sampled along straight lines parallel to the k_x-axis. Image reconstruction involves a simple $2D$ IFFT of the acquired data. Besides, the phenomenon of aliasing due to undersampling along Cartesian trajectories is easy to handle since it occurs as localized peaks. Figure 1.4 shows that if the FOV is of dimensions $FOV_x \times FOV_y$, then the spacing between samples along the two axes must satisfy the Nyquist requirements in order to be alias-free. The FOV depends on the k-space sampling intervals given by,

$$\begin{aligned} FOV_x &\leq \tfrac{1}{\Delta k_x} \\ FOV_y &\leq \tfrac{1}{\Delta k_y} \end{aligned} \tag{1.6}$$

where,

$$\begin{aligned} \Delta_{k_x} &= \tfrac{\gamma}{2\pi} G_x \Delta t \\ \Delta_{k_y} &= \tfrac{\gamma}{2\pi} G_y \tau_y \end{aligned} \tag{1.7}$$

Here G_x is the gradient along X, G_y is the gradient along Y, Δt is the time-resolution of the analog to digital converter and τ_y is the time for which the gradient along Y is applied.

On the other hand, the spatial resolution along X and Y, namely δ_x and δ_y achieved depend on the widths of k-space coverage along the respective axes (say, W_{k_x} along k_x and W_{k_y} along k_y), and are given by,

$$\begin{aligned} \delta_x &= \tfrac{1}{W_{k_x}} \\ \delta_y &= \tfrac{1}{W_{k_y}} \end{aligned} \tag{1.8}$$

Note that in MR, there is no aliasing in the frequency encoding or readout direction due to the anti-aliasing filter preceding the digitization step. The spatial resolution depends

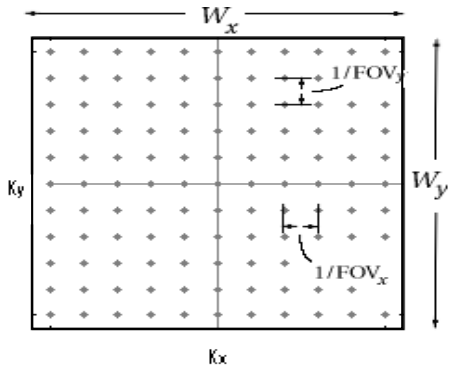

Figure 1.4: Constraints on Cartesian sampling of k-space in MR imaging. (Source : [69])

on the amount of high frequency content sampled bringing in the classic tradeoff between spatial and temporal resolution (speed of acquisition) in MRI. Sampling a finite extent of k-space can be thought of as the convolution of the object with a sinc function (i.e., low-pass filtering) in the image domain.

1.5 Sampling trajectories

A very important factor that determines the SNR of the data acquisition, time taken, quality of image reconstructed and the computations involved in the process of image reconstruction, is the sampling trajectory utilized [61, 36]. A variety of sampling trajectories have been explored, of which Cartesian is the simplest, and has already been discussed above. The most popular non-Cartesian trajectories are radial and spiral. The radial trajectory shown in Fig. 1.5(a) consists of a collection of spokes that are the radii of an imaginary circle in k-space. The advantage of this trajectory is that the energy-rich DC point is sampled in each of the scans. The low k-space which has high energy is more densely sampled than the high k-space, making the SNR of the acquisition high. In spiral trajectory, shown in Fig. 1.5(b), the points are sampled along a spiral centered at the origin of the k-space. Single or multiple spirals (interleaves) may be used depending on the desired application. The advantage of spiral trajectory lies in its insensitivity to

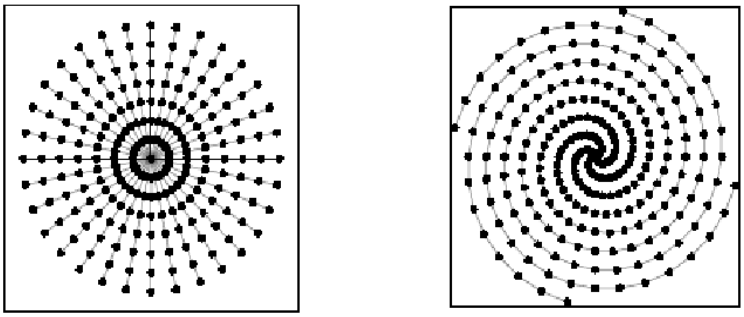

(a) (b)

Figure 1.5: Typical Non-Cartesian trajectories for sampling of k-space in MR acquisition. (a) Radial (b) Spiral

motion and flow-induced phase errors. Spiral trajectory is found to be the most efficient of all the trajectories since it covers a desired region with the smallest number of points. The high SNR of spiral acquisition comes from oversampling the centre of the k-space.

Besides, there are a large number of other trajectories such as circular, rosette and random trajectories. Significant developments in flexible gradient systems has allowed the MRI community to try non-Cartesian trajectories [61, 36, 69]. These acquisition patterns are all capable of generating MR images, but differ in attributes, such as speed, spectral off-resonance behavior, and flow and motion sensitivity.

1.6 Rapid imaging

Rapid imaging is being studied thoroughly by researchers as it is very relevant in medical engineering today [21, 62]. The imaging speed of conventional MRI is primarily limited by the sequential data acquisition scheme where the Fourier-encoded data in k-space is acquired one point at a time. However, in applications such as dynamic imaging, a sequence of images is acquired in order to monitor changes in tissue characteristics (structure) over time. The most popular applications of dynamic MRI include the observation of the flow of contrast agent to detect tumors, cardiac imaging and functional imaging of

the brain to detect BOLD (Brain Oxygen Level Dependent) response. These applications demand adequate temporal and spatial resolution, simultaneously. To accelerate image acquisition for the same k-space coverage, conventional MRI requires stronger magnetic field gradients, faster gradient switching rates and/or more frequently applied RF pulses (which would result in higher RF power deposition). Unfortunately, these approaches can pose increasing risks of damaging the underlying biological tissues. A safe alternative strategy to accelerate image acquisition is to come up with optimal data acquisition schemes that selectively collect samples in k-space. One approach is to follow selective k-space sample collection schemes that generally prioritize the associated k-space energy; The other approach is to regularly undersample the k-space and unfold the ensuing aliasing. In this thesis, we deal with strategies that aim at good quality images with sparsely sampled k-space.

1.7 Parallel imaging

The modern approach to accelerated MR imaging is a new hardware set-up, with entirely different concepts from what was discussed above in the context of conventional MR scanners, and is being thoroughly investigated [54, 8, 27]. The new set-up, called parallel MR scanner, is discussed in this section. Conventional MR scanners use a single homogeneous receiver coil for data acquisition. In contrast, parallel MR scanners use locally sensitive multiple receivers. Historically, parallel imaging was meant to obtain images with higher SNR. But later advancements [23, 53] showed that it could be used to reduce the number of phase-encoding steps, the most time-expensive factor in MR imaging. The signal contributed by the subject to each receiver coil varies according to the relative position of the subject from the respective coil. Though every receiver coil collects the same k-space data, each one contains different information about the image. Thus Fourier encoding as well as spatial encoding are simultaneously achieved. An illustration of the image obtained using coils with different spatial sensitivities is shown

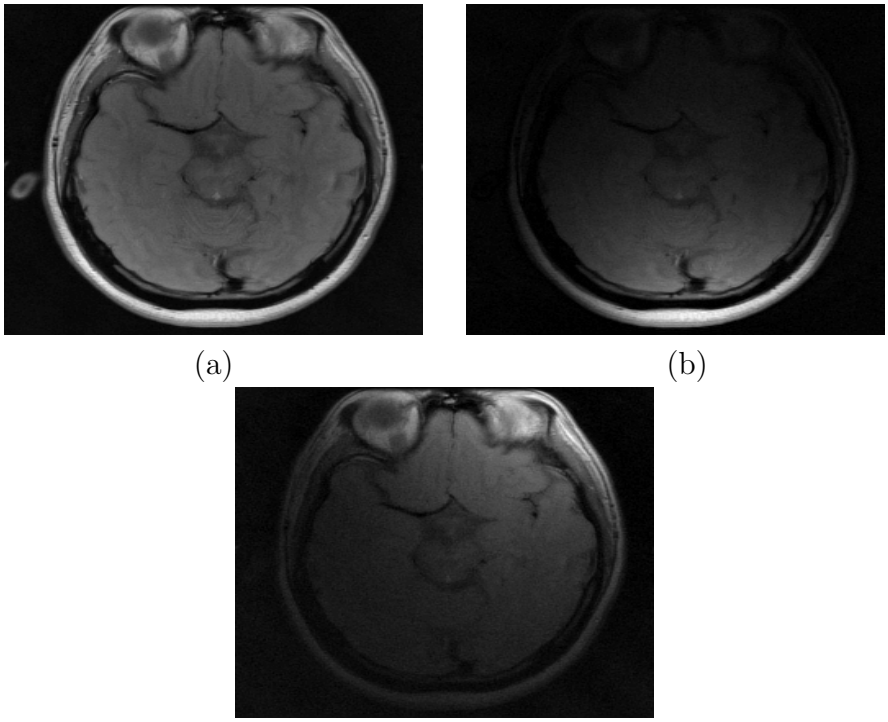

(a) (b)

(c)

Figure 1.6: Difference between images obtained by homogeneous body coil image and locally sensitive receiver coil images. (a) Body coil Image. (b) Image from one of the spatially-sensitive receiver coils. (c) Image from another coil with different spatial sensitivity

in Fig. 1.6. The image of the true object S, at location (x, y) acquired from the l^{th} coil, S_l is given as,

$$S_l(x, y) = C_l(x, y)S(x, y) \tag{1.9}$$

where C_l is the complex sensitivity of the l^{th} coil.

The basic concept in parallel imaging is illustrated in Fig. 1.7, depicting an ideal scenario. As shown, the object is seen differently by the two receiver coils. Each coil is characterized by its spatial sensitivity function, which conveys information about the relative position of the origin of the received signal. The sensitivity profiles of the receiver coils are used as complementary encoding functions to phase encoding. Each receiver coil collects the same available data, but the signal acquired is modulated by the characteristics

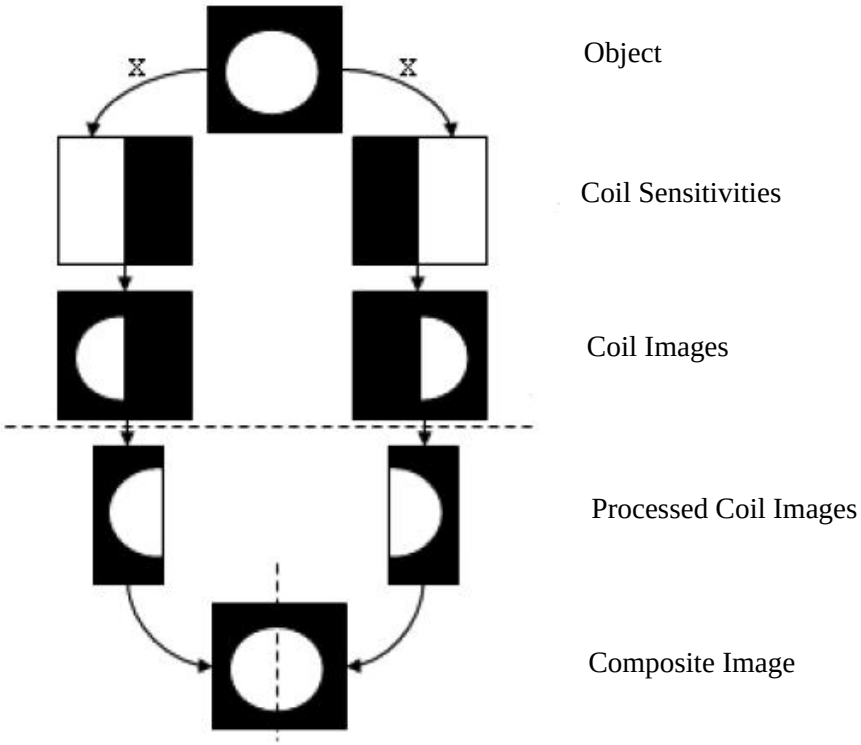

Figure 1.7: Concept of parallel imaging in MRI with multiple receiver coils having distinct coil sensitivities. (Source: [54])

of the receiver coil. Each coil provides its own weighted version of the image, all of which can eventually be combined to reconstruct the image. Each coil acquires only half of the image since it receives strong signal from areas it is closest to and low or no signal from points away from it. This effectively reduces the coil field of view (FOV) to half that of the image. If the individual coil data now were undersampled in k-space by a factor of 2, two halves of the image can be obtained simultaneously from the two coils. Once the two images are appropriately reconstructed after data acquisition, they can be combined to get the entire image. It is well-established that if each of the receiver coils could acquire the entire k-space, then the best estimate of the true k-space would be the "root of sum of squares" [35]. Typically, in parallel MRI, the data collected by each receiver element in k-space is undersampled. Hence the individual coil images obtained are aliased. In order to obtain unaliased images, either the coil images can be unfolded in the image domain or the missing coil k-space lines can be estimated. These coil images can either

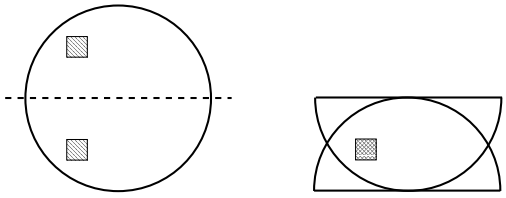

Figure 1.8: Illustration of the effect of downsampling. (a) True image. (b) Aliased image obtained due to downsampling by 2.

be unfolded in the image domain or the missing k-space lines are estimated, in order to obtain unaliased images. The unaliased coil images are eventually combined to yield the final image. The effect of subsampling the k-space is equivalent to reducing the effective FOV. Aliasing in image domain caused by subsampling in k-space by a factor of 2, is illustrated in Fig. 1.8.

In most of the existing techniques for image reconstruction in parallel MR, the information of the coil-sensitivities is crucial in obtaining the final reconstruction. Coil-sensitivities could vary with the object being imaged, and hence it is preferred to be estimated for each new scan.

The drawback in parallel MR imaging is the computational overhead incurred in the process of image reconstruction. The computational complexities depend on the sampling trajectory used, the estimation of coil sensitivities and the subsampling factor used. The case of data acquisition using Cartesian trajectories is well studied. Besides, the phenomenon of aliasing in the Cartesian case is easily understood due to its localised nature. Methods like SENSE [51], kt-SENSE [67], SMASH [64, 26], PILS [13], GRAPPA [12], kt-GRAPPA [56] have been in existence, that deal exclusively with Cartesian trajectories. Of late, non-Cartesian trajectories are being explored because of the many advantages they offer. However, they involve additional computational burden due to the requirements of density compensation and re-gridding along Cartesian grids. Some of the Cartesian reconstruction schemes are reportedly adapted for the non-Cartesian data acquisition as well. The well-known non-Cartesian reconstruction schemes include CGSENSE [50], POCS [60] and spiral/radial GRAPPA [16, 11]. In this thesis, we propose a novel method to unfold

images in the context of parallel MR imaging, with data acquired using both Cartesian and non-Cartesian trajectories.

1.7.1 Issues in parallel imaging

The image domain based SENSE and the k-space based GRAPPA have been the most popular and robust parallel image reconstruction methods. These methods allow high acceleration factors in principle [33], but practically they can be used only for moderate image acceleration factors (about 3-4) with acceptable image quality. SENSE and its variants suffer from numerical instability problems in the case of noisy acquisitions. On the other hand, GRAPPA results in multiple image reconstructions depending on the neighborhoods considered, and is computationally expensive. Besides, to be able to utilize GRAPPA for a given trajectory, it is necessary to obtain customized reconstruction kernels. This requires an additional scan with the same trajectory of data acquisition. It is necessary to develop image reconstruction techniques that can be applied to general trajectories. The reconstruction techniques must preferably avoid additional data acquisition, while being computationally feasible. In this thesis, strategies and concepts are explored to address these issues.

1.8 Organization of the thesis

Chapter 2 describes a data-truncation window-based method to achieve rapid imaging. Data truncation windows like rectangular, elliptical and rhomboid suffer from the drawback that many high frequency samples containing very less energy also get acquired resulting in lower acceleration factors. In this chapter, a novel star-shaped truncation window is proposed to increase the acceleration factor obtained. The proposed window monotonically cuts down the number of samples acquired in k-space regions with lesser energy. The data is sampled within a star-shaped region centered around the origin in the k_y-k_z plane. The missing values are extrapolated using generalized series modeling-based methods. The proposed method is applied to several real and synthetic data sets.

In chapter 3, a popular method for dynamic imaging that uses regular undersampling, called *k-t BLAST* is investigated. The method suffers from drawbacks such as separate training scan, blurred training estimates and aliased phase maps. In this chapter, variations to *k-t BLAST* have been proposed to overcome the drawbacks. The proposed improved *k-t BLAST* incorporates variable-density sampling scheme, phase information from the training map and utilization of generalized-series extrapolated training map. The existing technique and the proposed variations are applied on real fMRI data volumes.

Chapter 4 deals with parallel imaging using Cartesian trajectories and a novel method is proposed for image reconstruction in the framework of neural networks (NNs). This method is based on the observation that the aliasing patterns remain the same irrespective of whether the k-space acquisition consists of only low frequencies or all the frequencies. In the proposed approach, aliased coil images obtained using regularly undersampled data at each of the receiver coils are processed using the neural network framework. The technique, called as composite reconstruction and unaliasing using neural networks (CRAUNN) has been applied to phantom as well as real brain MRI data sets.

Chapter 5 extends the CRAUNN approach to non-Cartesian trajectories like spiral and radial. Neural networks are used as machine learning tools to learn the transformation needed to reconstruct the alias-free composite image from the aliased coil images, using acquisitions consisting of densely sampled low frequency k-space data. These NNs are then used to obtain the desired alias-free image from acquisitions containing sparsely sampled low and high frequencies. Experiments are performed using radial and spiral trajectories on real and synthetic data.

Chapter 6 contains the concluding remarks.

Chapter 2

Dynamic MR imaging using generalized series modeling

Abstract

Dynamic MR Imaging can be achieved by sampling only selected regions in k-space. Optimal region selection in the 3D k-space needs to satisfy "maximum energy capture" and "minimum acquisition" requirements. In this chapter, a novel star-shaped truncation window is proposed to increase the achievable acceleration factor. The proposed window monotonically eliminates the acquisition of the low energy k-space samples. The window removes the data outside a star-shaped region centered around the origin of the k_y-k_z plane. For the same fraction of k-space acquired, this window captures more k-space energy than all the other existing windows. The missed samples are predicted by generalized series modeling. The proposed technique is applied to several real and synthetic data sets. Its superior performance is illustrated using the standard measures of error images and uptake curve comparisons. Average values of slope error in estimating the enhancement curve are obtained over 5 real data sets of breast and abdomen images, for an acceleration factor of 8. The proposed method achieves a slope error of 5%, while the values obtained using rectangular and elliptical windows are 12% and 10%, respectively.

2.1 Dynamic contrast enhanced (DCE) MRI

Dynamic Magnetic Resonance Imaging is increasingly being used for functional studies where the organ being studied undergoes continuous change as in functioning of the brain, cardiac activity and contrast agent uptake by suspected tumors. A very important application of dynamic imaging is DCE-MRI. It is used for detection and diagnosis of cancer. In DCE-MRI, a bolus of a paramagnetic contrast agent (typically, gadolinium chelate) is injected intravenously. The agent shortens the relaxation times (T_1, T_2, and T_2^*) of the Hydrogen protons that are in its vicinity.

Generally T_1-weighted imaging sequences are preferred. Shorter T_1 values make the lesions appear brighter than the remaining tissues. Because of their high vascularity, the rate of contrast agent uptake by malignant lesions is significantly different from that of normal tissues. Malignant lesions can hence be detected by monitoring the rate of contrast agent uptake and their washout characteristics. This wash-in and wash-out phenomena are monitored by a time series of images of the region of interest. Typical imaging protocols work as follows : Initially, a data set (pre-contrast data) is acquired with high spatial resolution. Subsequently, a contrast agent such as Gd-DTPA is injected followed by saline flush. The injections are immediately followed by the acquisition of 4 or more post-contrast data sets, which takes a few minutes. The pre-contrast and the post-contrast image sets are acquired with identical acquisition parameters. The signal intensity through the different types of tissues follow distinct characteristics as shown in Fig. 2.1.

2.2 Issues in DCE-MRI

The rate of uptake of contrast agent, called “enhancement rate”, distinguishes malignant from benign tissues. The established way of measuring this rate is to calculate the slope of initial enhancement typically obtained by imaging the area of interest up to the time of peak enhancement (approximately 1.5 minutes), following the contrast injection. Beyond

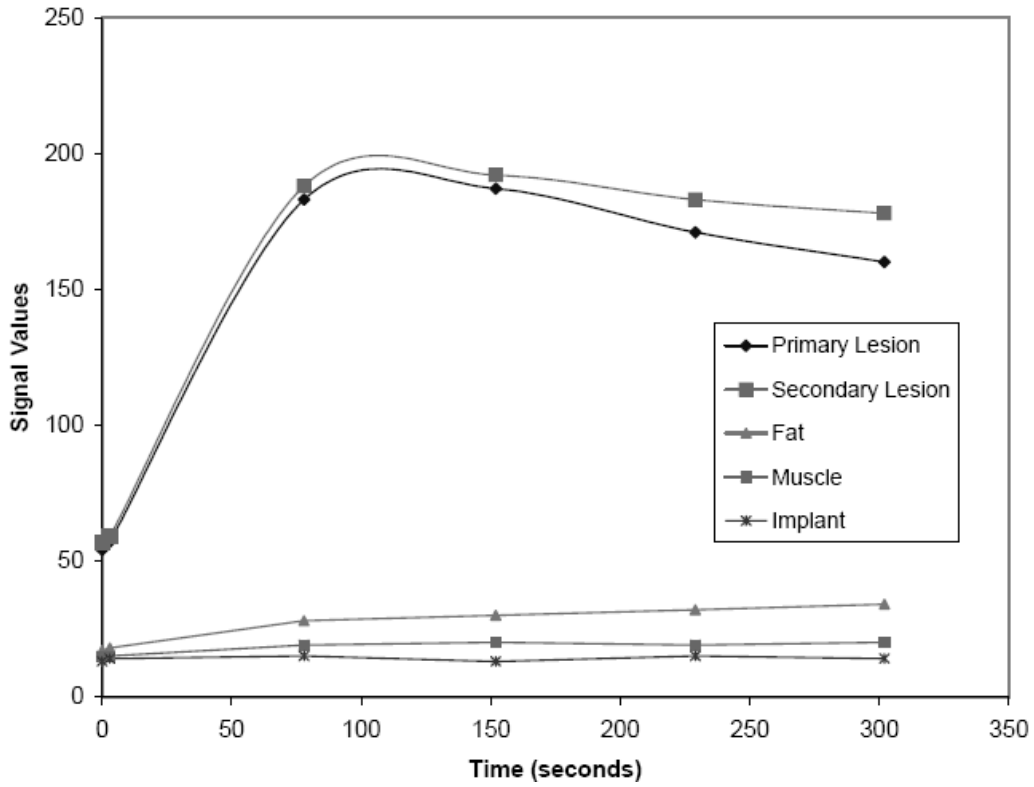

Figure 2.1: Contrast uptake for different types of tissues (Source: [19])

that time, signal intensity of normal tissues, which enhance slowly in the beginning, will begin to approach that of malignant tissue. In order to differentiate between malignant and benign tissues using the initial slope of enhancement, at least 4 samples must be obtained in 1.5 minutes, implying a temporal resolution requirement of about 20 seconds. The exact temporal resolution required is determined by the time course of contrast agent uptake. In malignant lesions, peak contrast enhancement typically occurs at about 90 seconds after injection, and hence to accurately determine lesions, we need to acquire data sets well within that duration.

As discussed earlier, the number of k-space points acquired determines the quality of the image obtained. Acquisition of fewer number of data points speeds up the process of data capture, but leads to Gibbs ringing and spatial blurring that significantly degrade the spatial resolution. On the other hand, acquiring many points in k-space leads to good image quality, but results in poor temporal resolution, that may not adequately capture

the uptake characteristics. Thus we need to obtain good quality images with reduced data in order to satisfy the conflicting requirements of good spatial and temporal resolution. Reduction in the volume of data acquisition leads to faster scans. The objective of any dynamic imaging technique is to obtain as high an acceleration factor as possible, since it indicates the ability of the technique to yield high-quality images with reduced data (lower acquisition time). Typically in DCE-MRI, the quality of image reconstruction is measured by the fidelity in the reproduction of the uptake curve through the region of interest. For this application, the error measures popular in image processing, namely error images and RMSE are not as important as the uptake slope error.

2.3 Techniques for DCE-MRI

Reduced data acquisition in conventional (sequential) MR scanners, where a single receiver coil is used, can be achieved either by acquiring only certain k-space regions or by regularly undersampling the entire data in k-space. In this chapter, our focus is on methods that follow the former approach. The two defining aspects in this approach are:

1. Optimal choice of k-space samples to be acquired

2. Technique to estimate the unacquired values

The required criteria for optimal selection of samples in k-space are "maximum energy capture" and "minimum acquisition". Partial data acquisition-based techniques hinge on the fact that if a small number of k-space samples containing a significant fraction of the total k-space energy, are captured at an adequate temporal resolution, then the dynamics of the sequence being imaged can be satisfactorily reconstructed. It is well-known that energy is concentrated at lower frequencies, and hence most acquisition schemes prioritize low frequency samples over data at higher frequencies. The ratio of the number of points acquired to the total number of available k-space points, is called the "acceleration factor". Techniques that result in higher acceleration factors are preferred because,

they capture the dynamic k-space at more number of time instants, resulting in higher temporal resolution.

The first dynamic imaging method, proposed by van Vaals [68] is called "Keyhole Imaging". According to this scheme, only the pre-contrast data acquisition, which is free of time constraints, contains the entire range of k-space frequencies. During the course of contrast uptake, only partial k-space data, within a rectangular window symmetric about the k_x axis is acquired. This rectangular window, at the center of the k_y-k_z plane is assumed to contain a significant fraction of the signal energy. Image reconstruction using keyhole acquisition simply involves substitution of unacquired dynamic k-space data with the pre-contrast data. This technique suffers from the drawback posed by discontinuities in k-space incurred by direct substitution, which manifests as artifacts in the obtained images. The accuracy is limited by the size of the enhancing object and the rate of enhancement.

An entirely different approach to dynamic imaging called "Continuous Update with Random Encoding" (CURE) has been reported in [46]. In this approach, the k-space lines are randomly acquired with the low k-space being more frequently visited. The missing k-space points are substituted using their nearest k-space neighbours. Yet another approach for rapid acquisition called "Time-Resolved Imaging of Contrast Kinetics" (TRICKS) [29], segments the k-space and not all the segments are acquired at each time point. Instead, low k-space segments are collected more frequently than the high k-space segments. The missing k-space data is estimated by interpolating between the collected data.

Variations of the keyhole method such as, keyhole with elliptical and rhomboid windows have also been in existence [62]. The drawback with rhomboid window is its maximum acceleration factor is 2. Experiments with elliptical windows have claimed better performance and higher acceleration factor due to the ability of the window to capture more k-space samples with higher signal energy. A variation of this technique is called "radial keyhole" [43]. Here, instead of a rectangular window, radial strips of data, whose centroid is the origin of k_y-k_z plane, are acquired, and the missing high k-space values are obtained by replacement. It must be noted that the above discussed methods differ

in their choice of the optimal sampling region in k-space, but are similar in their choice of estimates of the unacquired samples.

A method to estimate the unacquired samples more reliably than simple substitution has been devised using generalized series modeling by Liang [39], called RIGR (Reduced-encoding Imaging by Generalized series Reconstruction). This method is based on the fact that, in applications as in DCE-MRI, the image morphology in the time-series does not drastically change from one image to another. Hence full k-space need not be acquired at every time instant. A reference full k-space data set at pre-contrast (reference image) containing the stationary information is first obtained. This acquisition is followed by partial (rectangularly truncated) data during the contrast uptake phase. In fact, the data acquisition part is identical to that in keyhole imaging. RIGR differs in its approach to the estimation of the unacquired samples. The missing dynamic k-space data is estimated with the basis functions of a generalized series model using the reference data and the partially acquired dynamic data. In the works reported in [72, 65, 37], rectangular truncation window followed by RIGR-based extrapolation has been used. In [72], the technique is used to obtain dynamic images of liver. A full k-space post-contrast data set is used as the reference, and the reported temporal resolution is said to be greater by a factor of 3.

A variation of RIGR called "Two-reference RIGR" (TRIGR) has been proposed for improved performance [24]. Here, two full k-space images are obtained, one in the pre-contrast phase, and the second at the end of the post-contrast phase. The dynamic images between the two full k-space images (references) are reconstructed using the difference image between the two references to construct the basis functions of the generalized series model. These approaches result in reduced truncation artifacts compared to keyhole imaging. However, the drawback of these methods is that they tend to become unstable in the presence of noise, necessitating complicated regularization schemes for proper convergence.

One of the recently proposed methods is called "Dynamic Imaging with Energy Matching" (DIEM) [62]. In this method, data is acquired elliptically for each temporal phase

during post-contrast. Two full k-space reference images are acquired: one at the beginning (pre-contrast) and the other after the post-contrast phase. The peripheral k-space dynamic data is estimated using a scaled version of the second reference data instead of direct replacement with the pre-contrast reference data. The energy of an outer annulus of the central k-space data (i.e. the acquired dynamic data) is compared to that of the post contrast reference and an energy scaling factor computed as the square root of this ratio for each phase. Since the background signal causes significant errors in the computation of scaling factors, the pre-contrast reference is subtracted from the dynamic data for calculation of the energy scaling factors.

A very different approach is reported in [58], where a temporally enhancing lesion is considered as a two-dimensional space-time object possessing an associated spatio-temporal energy spectrum. The spatio-temporal space is segmented based on a threshold such that the total spectral energy in a finite number of k-space samples, constrained by the imaging experiment, is maximized. This thresholded map decides on the k-space samples to be acquired at specific time instants. The acquisition scheme is shown to be adequate for a wide range of contrast-enhancing breast lesions.

In this chapter, we propose a dynamic imaging scheme with a novel data truncation window. The proposed window aims at increasing the achievable acceleration factor. It monotonically cuts down the acquisition of the number of k-space samples with lesser energy. The truncation window samples data within a star-shaped region centered around the origin in the k_y-k_z plane. The missing values are extrapolated using generalized series modeling-based methods.

2.4 Generalized series modeling

Generalized series (GeS) model is a general framework developed for constrained image reconstruction. The explanation in this section and the notations are adapted from [39] and [24]. The dynamic imaging problem is the acquisition of a sequence of Q images, denoted as $I_1(x,y), I_2(x,y), \ldots, I_Q(x,y)$, each of which is a snapshot of the time-varying image function $I(x,y)$. Hence the corresponding Q data sets $d_1(k_x,k_y), d_2(k_x,k_y), \ldots, d_Q(k_x,k_y)$ need to be acquired in k-space at successive time instants. The following discussion assumes $1D$ signals and can be extended to the multi-dimensional cases. The q_{th} data set in k-space is related to the q_{th} image as,

$$d_q(k) = \int_{-\infty}^{\infty} I_q(x) e^{i2\pi kx} dx \tag{2.1}$$

Here, the modeled image function I_{GeS} is represented as

$$I_{GeS}(x) = \sum_n c_n \phi_n(x) \tag{2.2}$$

where, $\phi_n(x)$ are the basis functions given by $\phi_n(x) = C(x)\exp^{2i\pi n\delta x}$. $C(x)$ is the constraint function that is chosen to absorb the available apriori information. c_n are the weighting co-efficients.

The generalized series framework is utilized for dynamic image reconstruction with as few phase encodings as possible. It relies on the fact that the evolving k-space cannot change much between two successive time instants. Two extrapolation techniques are utilized in our work, based on generalized series modeling.

2.4.1 RIGR

Here, data is acquired in the same way as in keyhole. One full k-space (high-frequency resolution) data set is obtained before the injection of contrast. During the course of contrast uptake and subsequent wash-out, several partial data sets are acquired. The full

k-space data set serves as the initial estimate for the dynamically changing k-space that we set out to compute.

Here, the constraint function $C(x)$ is chosen as an initial estimate of the desired function $I(x)$ and hence the optimal reconstruction is the one that maximizes the following cross-entropy measure,

$$-\int_{-\infty}^{\infty} I(x) log \frac{I(x)}{\mathcal{C}(x)} dx$$

subject to the data consistency constraints

$$d(m\Delta k) = \int_{-\infty}^{\infty} I(x) e^{i2\pi m \Delta k x} dx \tag{2.3}$$

The solution to the above constrained problem is

$$\tilde{I}(x) = \mathcal{C}(x) \exp\left(\sum_n \lambda_n e^{i2\pi n \Delta k x}\right) \tag{2.4}$$

where, λ_n are appropriate Lagrange multipliers.

If $C(x)$ is a good estimate for $\tilde{I}(x)$, then the power series expansion of the exponential term is approximated by the first two terms, resulting in

$$\tilde{I}(x) \approx \sum_n [\delta(n) + \lambda_n] \mathcal{C}(x) e^{i2\pi n \Delta k x} \tag{2.5}$$

which turns out to be the same as the generalized series model function $I_{GeS}(x)$ in Eqn. 2.2, with $c_n = \delta(n) + \lambda_n$.

The unknown parameters c_n are determined by a system of linear equations as described later. Renaming the coefficients as $\hat{c}_0 = 1 + c_0$ and $\hat{c}_n = c_n$, for $n \neq 0$, the GeS

model is re-written as

$$I_{GeS}(x) = \mathcal{C}(x) + \mathcal{C}(x) \sum_{n} \hat{c}_n e^{i2\pi n \Delta k x} \tag{2.6}$$

or in the data acquisition domain, we get

$$d_{GeS}(k) = d_c(k) + \sum_{n} \hat{c}_n d_c(k - n\Delta k) \tag{2.7}$$

where $d_c(k)$ is the Fourier transform of $C(x)$

Equation (2.7) suggests that the high spatial-frequency data modeled by generalized series consists of two parts : The first part incorporates the prior information and the other part is adaptively adjusted through the coefficients to maintain data consistency.

The spatial resolution of $I_{GeS}(x)$ would be at least as good as that of $C(x)$. If a high spatial-resolution reference image is acquired and used to define the basis functions, high spatial-resolution dynamic images can subsequently be reconstructed using the generalized series model with only few dynamic encodings.

The q^{th} dynamic image I_q is modeled using GeS, with N_L phase encodings and $C(x)$ as the constraint function as,

$$I_q(x) = |C(x)| \sum_{n=-\frac{N_L}{2}}^{\frac{N_L}{2}-1} c_n e^{i2\pi n \Delta k x} \tag{2.8}$$

The generalized series coefficients c_n are then given by,

$$d_q(m) = \sum_{n=-\frac{N_L}{2}}^{\frac{N_L}{2}-1} c_n d_c(m-n), \quad -\frac{N_L}{2} \leq m \leq \frac{N_L}{2} - 1 \tag{2.9}$$

where N_L is the number of k-space lines acquired, $d_q(k)$ is the Fourier transform of $I_q(x)$ and $d_c(k)$ is the Fourier transform of $C(x)$.

2.4.2 TRIGR

A variation of RIGR called TRIGR, which stands for "Two-reference RIGR", was proposed in [24]. The data acquisition in TRIGR consists of a full k-space (high spatial resolution) baseline data set ($d_{baseline}$) and several partial data sets (d_{dyn}, assume that only N_L lines are acquired in the partial data sets) and one full k-space active reference (d_{active}) data set. Dynamic images are reconstructed using the generalized series model with a reference image reflecting the areas of change in the sequence of images. The difference reference image (I_{ref}) is constructed by subtracting the complex baseline ($I_{baseline}$) from the active reference (I_{active}) image.

The dynamic difference data at the q^{th} sampling instant ($d^q_{diff}(k)$) is created as:

$$d^q_{diff}(k) = d^q_{dyn}(k) - \hat{d}_{baseline}(k) \tag{2.10}$$

where, $d^q_{dyn}(k)$ is the dynamic data and $\hat{d}_{baseline}(k)$ represents the baseline reference encodings. The RIGR model then becomes

$$I^q_{diff}(x) = |I^q_{ref}(x)| \sum_{n=-\frac{N_L}{2}}^{\frac{N_L}{2}-1} c_n e^{i2\pi n\Delta kx} \tag{2.11}$$

where, $I^q_{ref}(x)$ is the difference reference image and N_L is the number of dynamic encodings.

The coefficients c_n are obtained by fitting the difference data to maintain consistency of the data, as in equation (2.9), given by:

$$d^q_{diff}(m) = \sum_{n=-\frac{N_L}{2}}^{\frac{N_L}{2}-1} c_n d^q_{ref}(m-n) \tag{2.12}$$

where, $d^q_{ref}(m-n)$ is the difference data created by subtracting the baseline and active reference data sets. The dynamic image (I^q_{dyn}) is generated by adding the complex dynamic

difference image (I^q_{diff}) to the baseline reference ($I_{baseline}$) image :

$$I^q_{dyn}(x) = I^q_{diff}(x) + I_{baseline}(x) \tag{2.13}$$

2.5 Data truncation windows

Data truncation windows are used to acquire samples within a chosen region in the k-space. Partial data acquisition is always carried out such that fewer values are captured along either k_y or k_z or both. Since signal energy is concentrated at lower frequencies acquisition schemes are designed to capture more points in low k-space.

2.5.1 Rectangular (RS) and elliptical (ELL) windows

The most commonly used data truncation window is "rectangular" in shape (RS), as shown in Fig. 2.2(a). An "elliptical" (ELL) window is also in use (shown in Fig. 2.2(b)), which prioritizes points based on the radial distance from the origin in the k_y-k_z plane. For higher fractions of k-space availability, the two masks look similar, as the curvature of the ellipse straightens. Another variation of the RS truncation window, is the "rhomboidal" window, where the four vertices of the rhombus touch the four edges of the k_y-k_z plane. Each of the windows has a trade-off between the maximum acceleration factor possible and the energy captured. Here, we explore the usage of a novel window, called the "star-shaped" window.

2.5.2 Star-shaped (SS) data truncation window

The star-shaped (SS) data truncation window, (see Fig. 2.3) consists of 4 arms all along the k_y-k_z axes. The window is so shaped that it captures greater number of points near the origin, while the number of data points tapers off as we move away from the origin. We observe that the SS data truncation window retains all those points in the k_y-k_z plane, whose one or both co-ordinates lie in the low-frequency range. Besides, as we

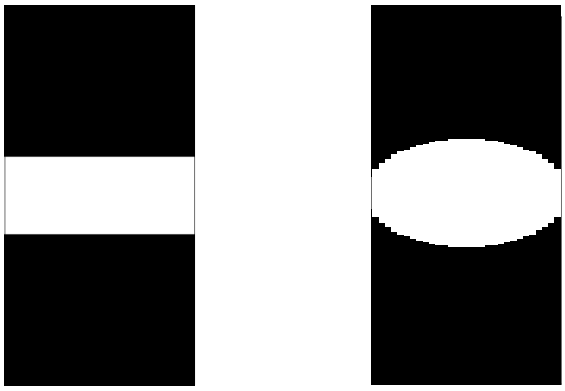

(a) (b)

Figure 2.2: Two of the widely utilized data truncation windows in k_y-k_z plane. (a) Rectangular (RS) (b) Elliptical (ELL)

increase the fraction of k-space available, the window expands near the origin, leading to acquisition of many more points in the desired low k-space. Hence, we expect this mask to be able to capture a greater fraction of the k-space energy, for a given fraction of k-space availability. For a given value of k-space fraction, the SS mask is unique. This is because the data dimension along Y is far higher than that along Z. Hence those arms of the SS window that occupy greater area are along Y, and have smaller slope than those arms that occupy smaller area lying along Z. Besides, the axes of the triangles that constitute the SS window coincide with the Y and Z axes.

In acquisitions where the data is not too noisy, it is expected that the acquisition-scheme that optimizes the "highest-energy capture" criterion results in the best image reconstruction, for a given fraction of the k-space availability.

A comparison of energy captured by the 3 masks, namely, SS, ELL and RS, is presented on a synthetic and several real data sets. We leave out the rhomboidal mask, since its acceleration factor is only 2. As can be seen from Figs. 2.4 to 2.7 the SS-mask consistently captures more energy at lower fractions of k-space availability, leading to the conjecture that it might lead to better image reconstruction. It may also be observed that the ELL mask captures more k-space energy than the RS mask for lower fractions of k-space availability. However, as the fraction of k-space chosen increases, the energy captured by RS and ELL masks become comparable.

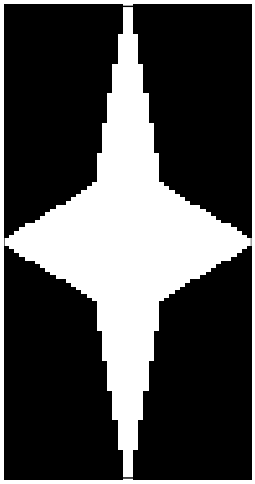

Figure 2.3: Proposed data truncation window in k_y-k_z plane : Star-shaped (SS) mask

2.6 Experiments on different MRI data sets

All simulations are carried out in MATLAB. The proposed method is applied to a synthetic phantom as well as real data volumes of breast and abdomen. In our experiments we have used both the extrapolation techniques, RIGR and TRIGR. The k-space data are extrapolated utilizing the fast versions of the algorithms as given in [40]. The partial data sets obtained by the star-shaped window as well as the rectangular and elliptical windows are utilized. The criteria used to assess the performance of the methods are:

- Faithful reproduction of enhancement curves (Error in slope calculation)
- Difference images with respect to the original ("gold-standard") image
- Comparison of the profile of scan lines

The results on each data set are presented separately.

2.6.1 Synthetic data

The proposed method is first applied on a noisy synthetic data set, for proof of concept. The phantom is constructed simulating tumors of various sizes and shapes, enhancing at different rates (see Fig. 2.4(a)). The data set is of dimensions 256 $\times$ 256 $\times$ 20 along

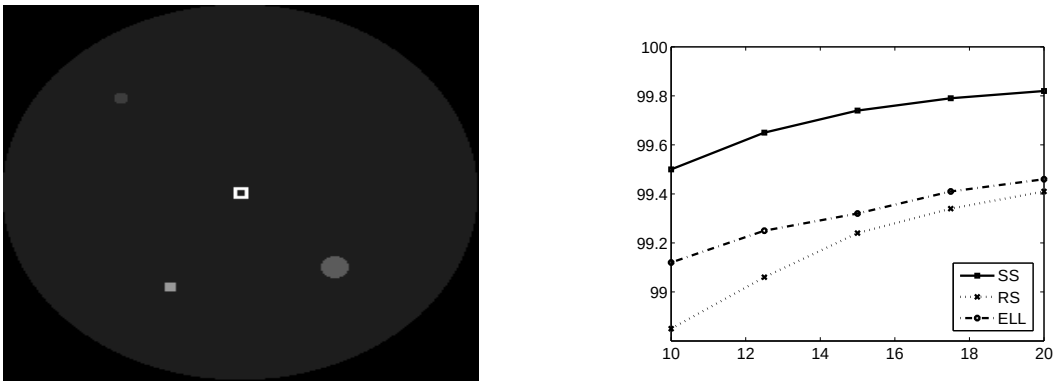

(a) (b)

Figure 2.4: Comparison of k-space energy captured from a phantom data set by the different masks studied. (a) Mid-slice of the phantom. (b) Plot of percentage of energy captured vs. percentage of k-space acquired.

X, Y and Z axes, respectively. The evolving k-space is captured at 7 time instants. To simulate reduced data sets, the respective masks are applied to the full data. Images are reconstructed after extrapolation by RIGR and TRIGR from various fractions of k-space. The objective is to look into acceleration factors of at least 4, corresponding to k-space acquisitions of 25% and below. The most-challenging part of the phantom reconstruction is the rim-enhancing (annular) tumor, seen at the center of the slice in Fig. 2.4(a).

Case (i) : RIGR reconstruction

The results are shown in Fig. 2.8 for 20% of k-space availability. A close look at the error images clearly shows the differences. It should be noted that the maximum error in the difference images occurs at the annular tumor. The error image corresponding to the SS mask shows the least amount of ripples, while the other masks result in substantial ringing at abrupt transitions. The profile through a tumor shown in Fig. 2.9, has ripples in the RS reconstruction, while the SS and ELL mask reconstructions follow the abrupt change in intensity more faithfully.

Case (ii) : TRIGR reconstruction

The results are discussed for 20% of k-space availability. The error images in Fig. 2.10 clearly show that the quality of TRIGR reconstruction is better than that of RIGR. The SS mask results in better image reconstruction than ELL and RS masks as shown by the

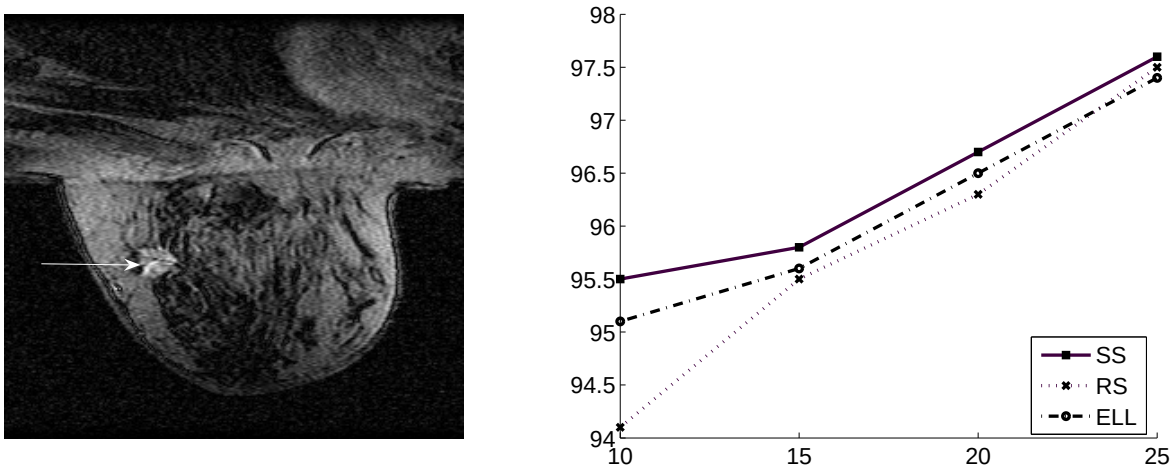

(a) (b)

Figure 2.5: Comparison of the percentage of energy captured by various masks on a real data set (breast) (a) Original image of the real data set: breast with a large tumor shown by the arrow. (b) Corresponding plot of percentage of energy vs. percentage of k-space acquired.

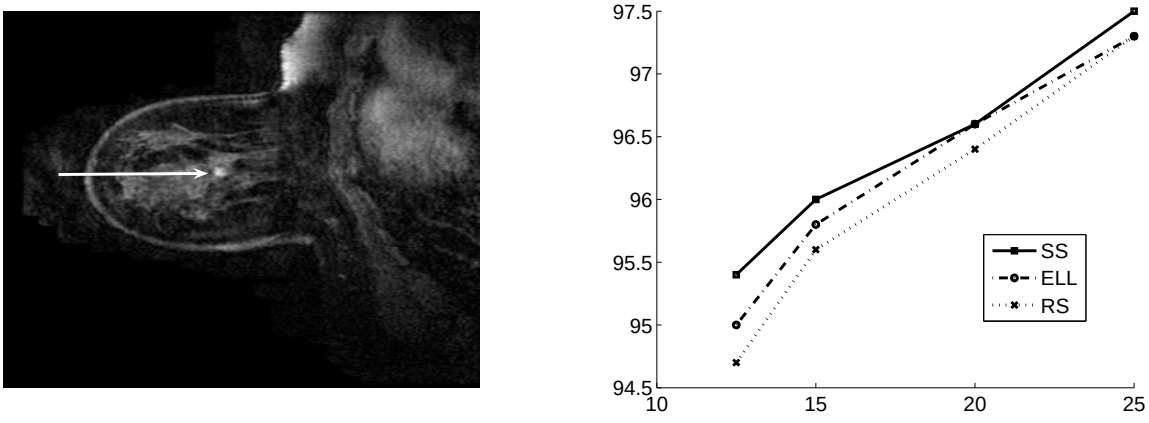

(a) (b)

Figure 2.6: Comparison of energy captured by various masks on another breast data set. (a) Original breast image, with a small tumor shown by the arrow. (b) Corresponding plot of percentage of energy captured by the window vs. percentage of k-space acquired.

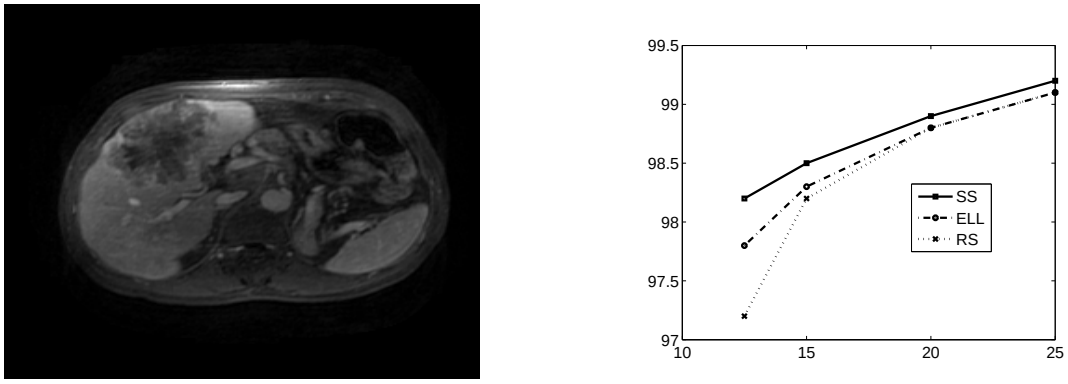

(a) (b)

Figure 2.7: Comparison of energy captured by various masks on an abdomen data set. (a) Original image. (b) Corresponding plot of percentage of energy vs. percentage of k-space acquired.

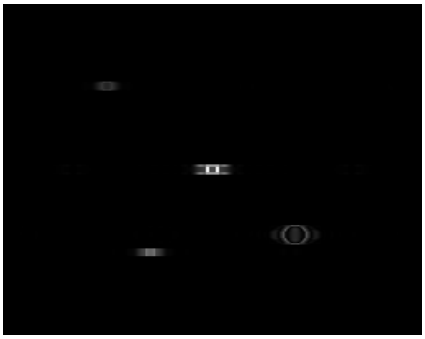

(a)

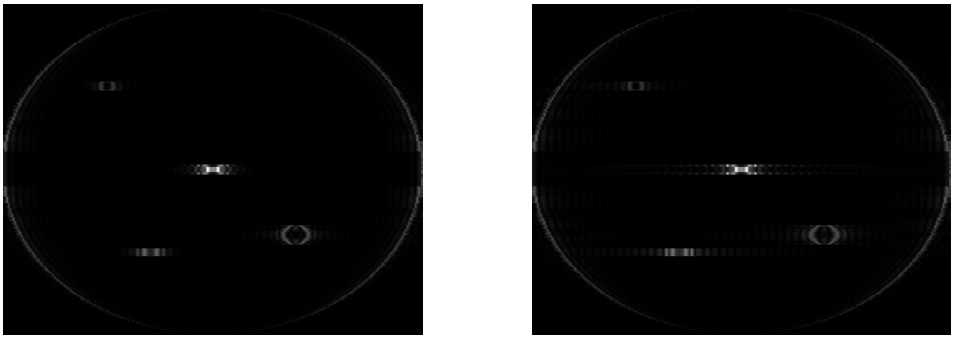

(b) (c)

Figure 2.8: Comparison of performance of different masks on the synthetic data set shown in Fig. 2.4(a) for acceleration factor 5. Error images for RIGR reconstruction using masks (a) SS (b) ELL (c) RS (color scale for all images : 0 to 16)

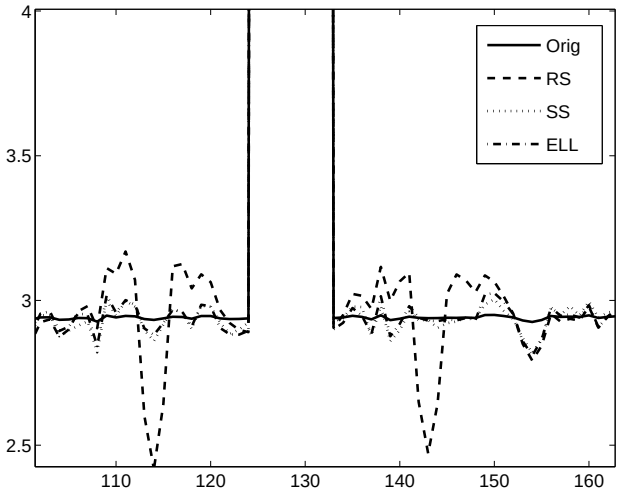

Figure 2.9: Comparison of scan lines through the annular tumor in the RIGR reconstructions obtained using different masks

profile through a tumor in Fig. 2.11. The RS reconstruction clearly shows ripples while the SS and ELL masks based reconstructions follow the abrupt change in intensity more faithfully. In this case, unlike RIGR, it must be noted that while the SS mask performs the best, the performances of RS and ELL masks are comparable.

2.6.2 Real data

Five real data volumes are analyzed: 2 breast and 3 abdomen data sets. One of the breast data sets contains a large enhancing tumor while the other has a small tumor. The abdomen data sets are all similar with no enhancing tumors, but contain enhancing blood vessels.

Breast data with large tumor

This data set is of dimensions 256 $\times$ 256 $\times$ 36. The 21^{st} slice shown in Fig. 2.5(a) has a large tumor occupying about 300 pixels out of 256 $\times$ 256, . The image shown has perceptibly high SNR. We expect the reconstruction of these images to be good, not only because of the signal quality, but also because of the large size of the tumor. The dynamic volume is available at 5 time instants.

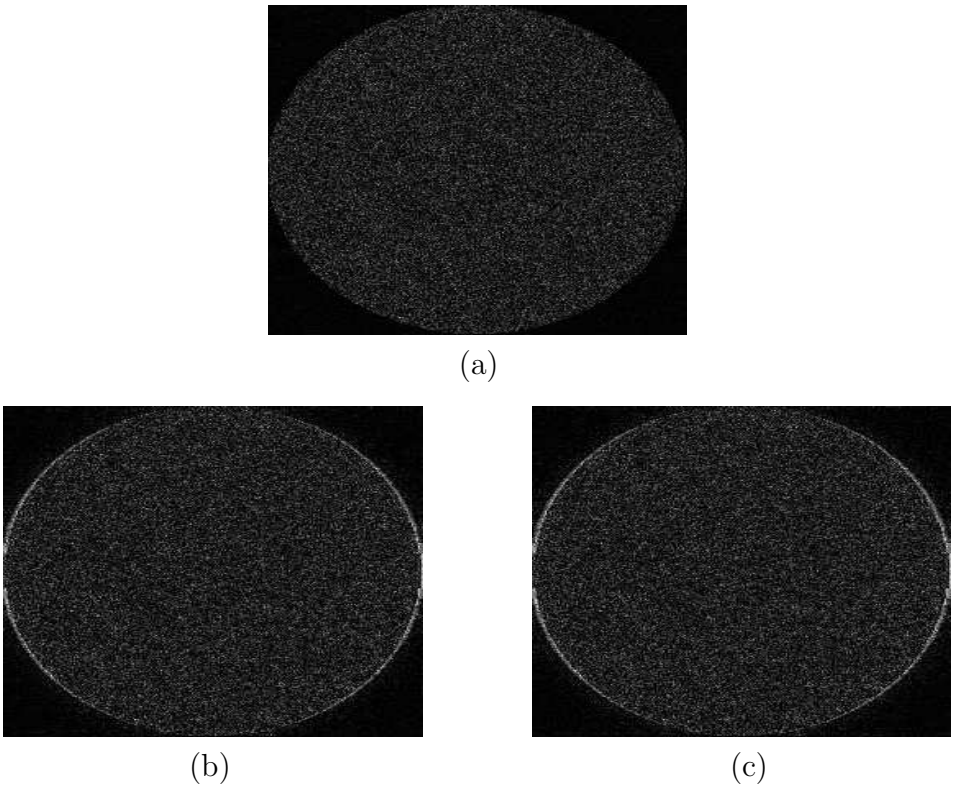

(a)

(b) (c)

Figure 2.10: Comparison of performance of different masks on the synthetic data set shown in Fig. 2.4(a) for acceleration factor 5. Error images for TRIGR reconstruction using masks (a) SS (b) ELL (c) RS (color scale for all images : 0 to 14)

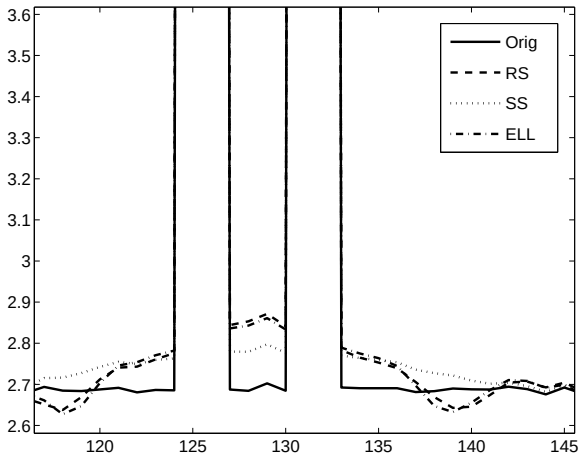

Figure 2.11: Comparison of scan lines through the annular tumor in the TRIGR reconstructions obtained using different masks

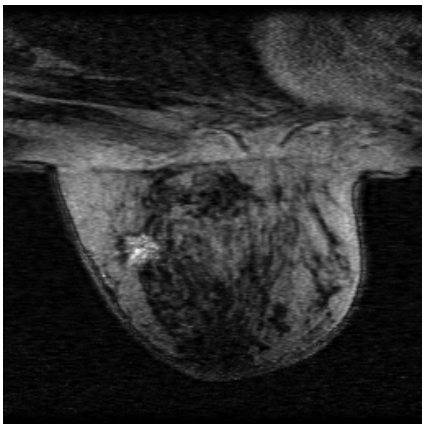

(a)

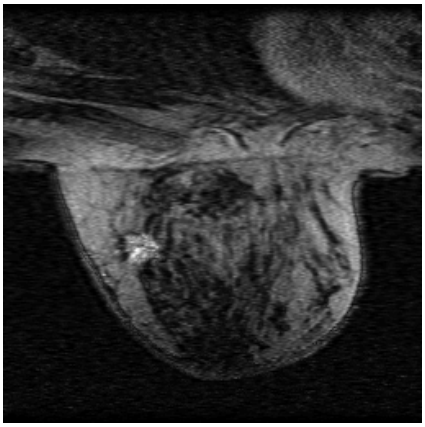

(b)

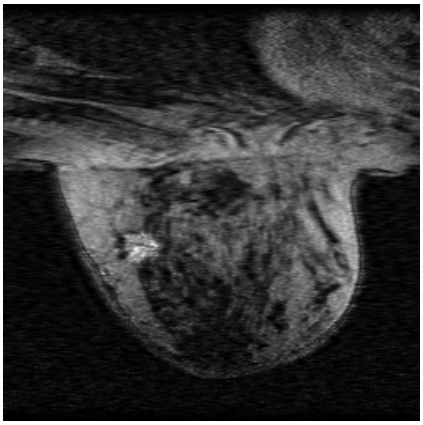

(c)

Figure 2.12: Performance on the real breast data set with large tumor (shown in Fig. 2.5(a)): Comparison of images reconstructed using RIGR with various masks : (a) SS (b) ELL (c) RS. (color scale for all images : 0 to 255)

Case (i) RIGR reconstruction : The volume at the first time instant is chosen as the high spatial-resolution data set, and the remaining 4 volumes are reduced according to the 3 masks considered. The images reconstructed from 20% of k-space sampled are shown in Fig. 2.12. All the 3 masks perform comparably well and result in satisfactory quality of reconstructed images. However, the reconstruction using RS mask looks blurred as compared to the ones obtained with other masks.

The plots shown in Fig. 2.13(a) are obtained from the images shown in Fig. 2.12. The plots suggest that all the phases are satisfactorily reconstructed. The plot in Fig. 2.13(b) clearly shows that the enhancement curve slope error is well within 10%, even for

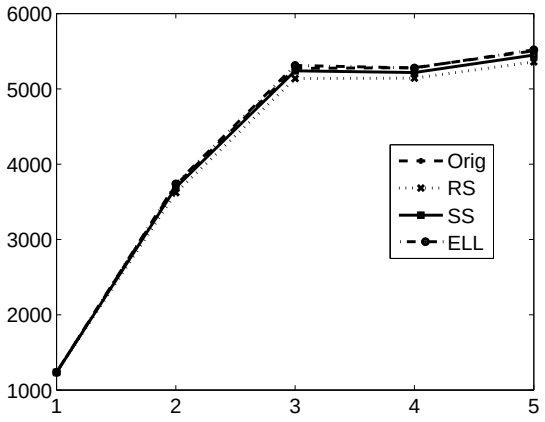

(a)

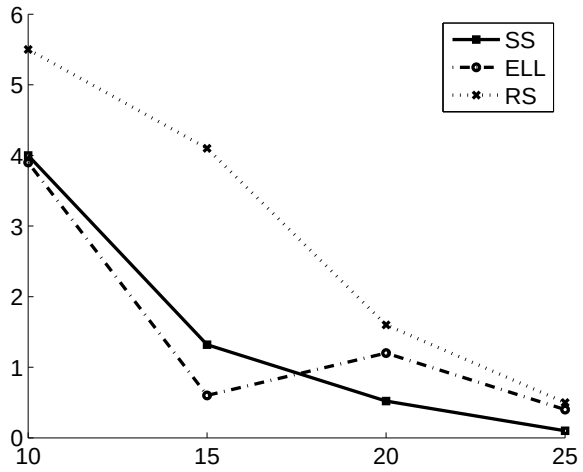

(b)

Figure 2.13: Results on breast data with large tumor (shown in Fig. 2.5(a)) with RIGR reconstruction. (a) Comparison of the enhancement curves through the tumor (b) Comparison of the percentage uptake slope error vs. percentage of k-space sampled

cases where only 10% of k-space is available. Hence, acceleration factors of even 10 can be achieved on data sets of this nature.

Case (ii) TRIGR reconstruction : The first and the last volume are chosen as the high spatial-resolution data sets, and the remaining 3 are reduced according to the 3 masks considered. The performance of both RIGR and TRIGR are comparable in such a noise-free, large tumor data. Differences in performance can be expected at very high acceleration factors. However, we do not consider cases of very high acceleration factor (8 and above) because the SNR of the data acquisition would be very low.

Breast data with small tumor

This data set is of dimensions $256 \times 256 \times 20$. The 11^{th} slice has a tumor as shown in Fig. 2.6(a). The images are noisy, and the tumor is very small, occupying about 15 pixels out of 256×256. The dynamic volume is available at 4 time instants.

Case (i) RIGR reconstruction : The first volume is chosen as the high spatial-resolution data set, and the remaining 3 are reduced separately using each of the 3 masks considered. Since the images are noisy, the regularization parameter in RIGR needs to be fine-tuned. The error images seen in Fig. 2.14 are obtained from reconstructions with 20% of k-space availability. Here it is seen that SS and RS masks perform much better than the ELL mask.

The plot in Fig. 2.15 clearly shows that the percentage slope error with SS mask is within 10%, even for k-space acquisition as low as 12.5%. Hence acceleration factor as high as 8 can be achieved with the SS mask. As also observed from the error images in Fig. 2.14, of all the masks, the ELL mask results in the highest error.

Case (ii) : TRIGR reconstruction : The first and the last volumes are chosen as the high-resolution data sets, and the remaining 2 are reduced according to each of the 3 masks separately. The plot of the error in enhancement slope versus fraction of k-space acquired shows that the performance of TRIGR is better than that of RIGR.

The plot shown in Fig. 2.16(a) is obtained after reconstruction using 25% of the k-space. The plot in Fig. 2.16(b) indicates that the enhancement curve slope error with SS

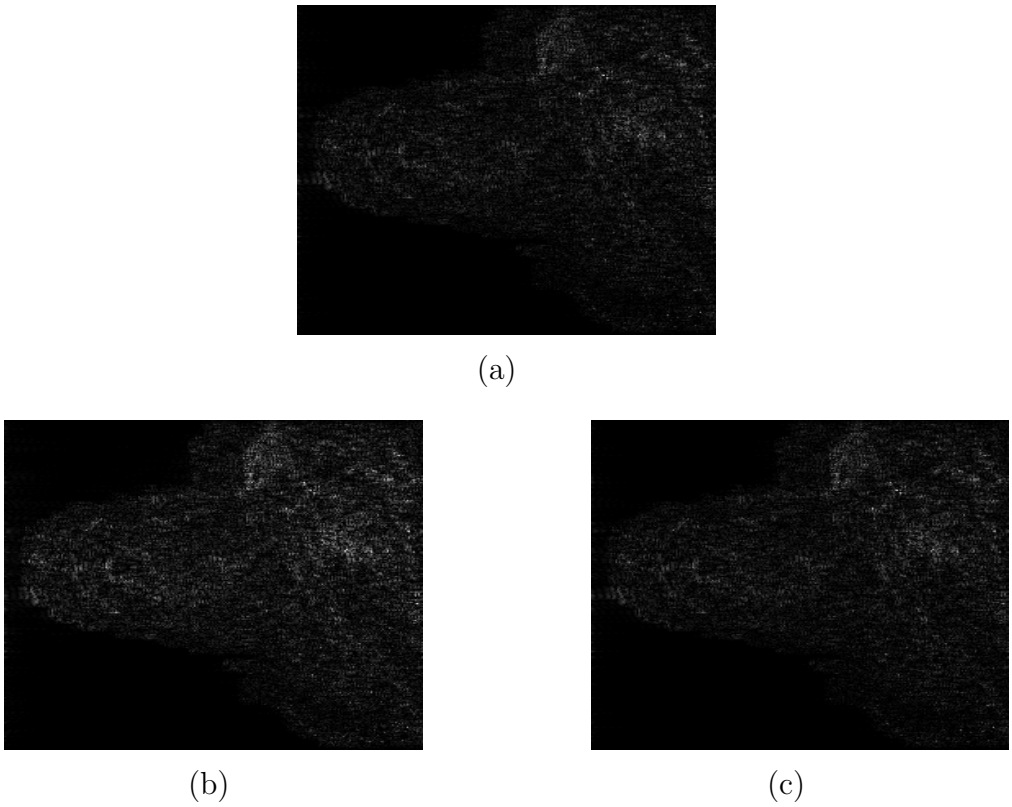

(a)

(b) (c)

Figure 2.14: Performance on the real breast data set with small tumor: Comparison of error images obtained from RIGR reconstructions using various masks : (a) SS (b) ELL (c) RS. (color scale for all images : 0 to 70)

mask is within 10%, even for fractions as small as 12.5% indicating a higher achievable acceleration factor, as compared to the technique using RIGR. Consistent with RIGR reconstructions, it is seen that the SS and RS masks perform better than the ELL mask.

Abdomen data

Three abdomen data sets are used in this experiment, of which 2 are of dimensions $256 \times 256 \times 20$, while the third is of size $256 \times 256 \times 36$. ROIs of different sizes are chosen in order to assess the accuracy and resolution of the reconstruction techniques. Enhancing structures like blood vessels are used as ROIs. Signal enhancement curves through the ROIs are used to compute errors in the slope of contrast uptake. The difference images are also examined for reconstruction quality and artifacts. Large ROIs typically occupy

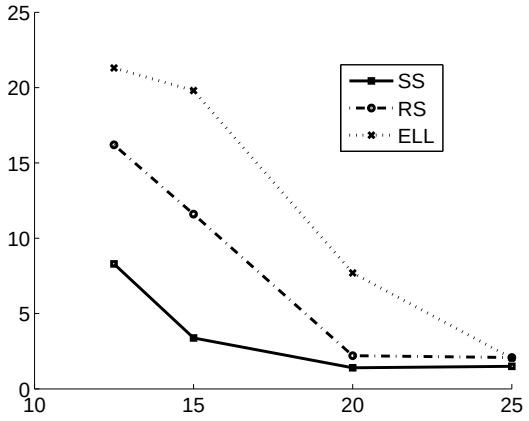

Figure 2.15: Comparison of the percentage uptake slope error vs. percentage of k-space available with RIGR reconstruction, for breast data with small tumor.

100 pixels and above, while small ROIs occupy about 20 pixels. ROIs from all the 3 data sets are analyzed, and the mean of the slope errors is calculated. A typical image in the data sets utilized is shown in Fig.2.7(a).

Case (i) : RIGR reconstruction : At k-space availability of 20% and above, all the masks perform comparably well, with the slope errors well-within bounds of 10%. However, differences can be observed in the values of slope errors for varying sizes of ROI.

Case (ii) TRIGR reconstruction : All the masks achieve slope errors less than 10% with k-space percentage of 15% and above. The errors in slope uptake curve are negligible for larger ROIs, even at high acceleration factors. However for smaller ROIs, only lesser acceleration factors are achievable.

Clearly, plots in Figs. 2.17 and 2.18, show that TRIGR outperforms RIGR. For a given acceleration factor, reconstruction using TRIGR results in far less an error than RIGR. The plot in Fig. 2.18(a) shows that if the ROI in question is known to be large before hand, then acceleration factors up to 8 are achievable with any mask, since the slope errors are negligible. But if the ROI happens to be small (see plot in Fig. 2.18(b)), then SS mask performs better. The errors in the images reconstructed using TRIGR are seen in Fig. 2.19 for 15% of k-space availability.

Average values of slope error in estimating the enhancement curve are obtained over 5

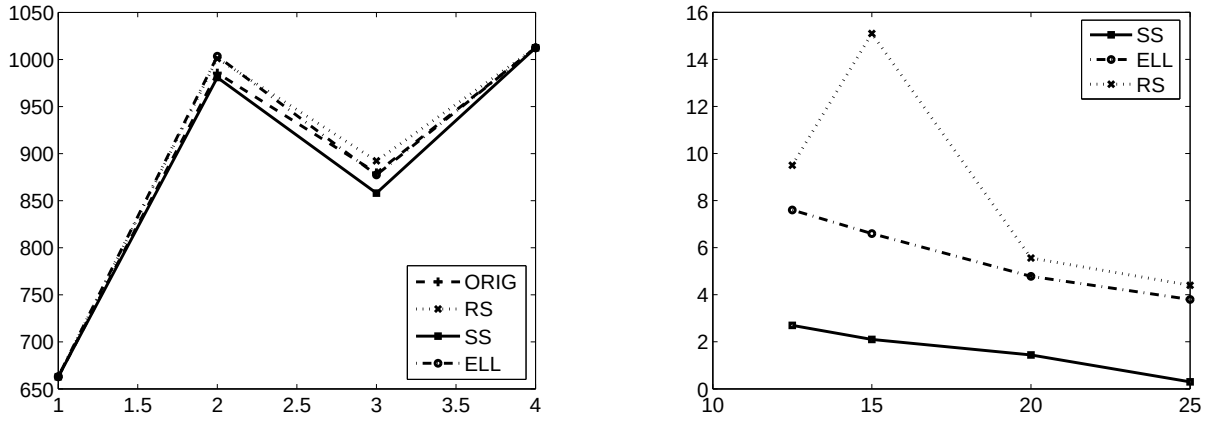

(a) (b)

Figure 2.16: (a) Comparison of the enhancement curves (signal intensity vs. sampling instants) through the tumor in the TRIGR reconstructed images of the data shown in Fig. 2.6(a). (b) Corresponding plot showing comparison of the percentage uptake slope error vs. fraction of k-space available

real data sets of breast and abdomen images, for an acceleration factor of 8. The proposed method results in a slope error of 5%, while the values obtained using rectangular and elliptical windows are 12% and 10%, respectively.

2.7 Discussion

As seen from the experiments, reconstructions using TRIGR are always better than the corresponding images obtained using RIGR. This is to be expected since TRIGR involves acquisition of 2 full k-space data sets. The error images obtained from the reconstructions and the errors in slope of contrast uptake, consistently are found to be much better with TRIGR reconstructions. It can be observed that higher acceleration factors are possible when TRIGR is utilized along with the proposed SS data truncation window. The quality of image reconstruction obtained depends on the SNR of the data acquisition and the relative size of the region of interest in the image.

In the comparison of scan lines through regions of abrupt transitions, the reconstruction using RS mask shows far greater ripples than the other two masks. Contrary to

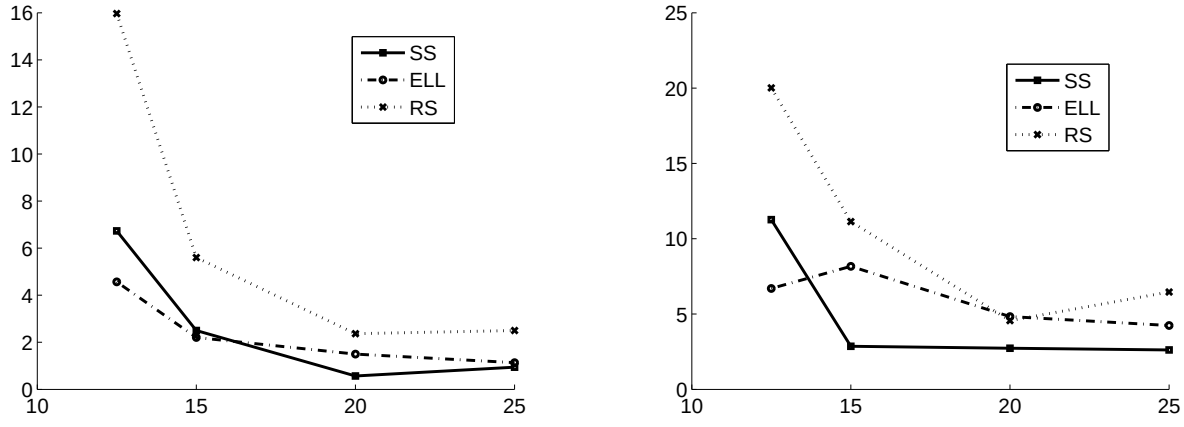

(a) (b)

Figure 2.17: Mean percentage slope errors vs. percentage of k-space sampled on real data sets of abdomen using RIGR (a) Large ROI (100 pixels) (b) Small ROI (20 pixels)

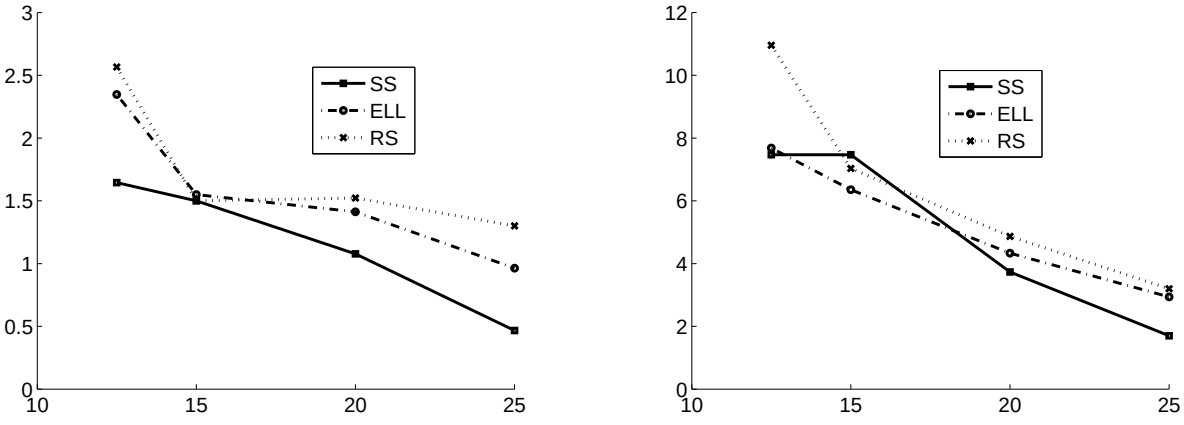

(a) (b)

Figure 2.18: Mean percentage slope errors vs. percentage of k-space sampled on real data sets of abdomen using TRIGR reconstruction (a) Large ROI (100 pixels) (b) Small ROI (20 pixels)

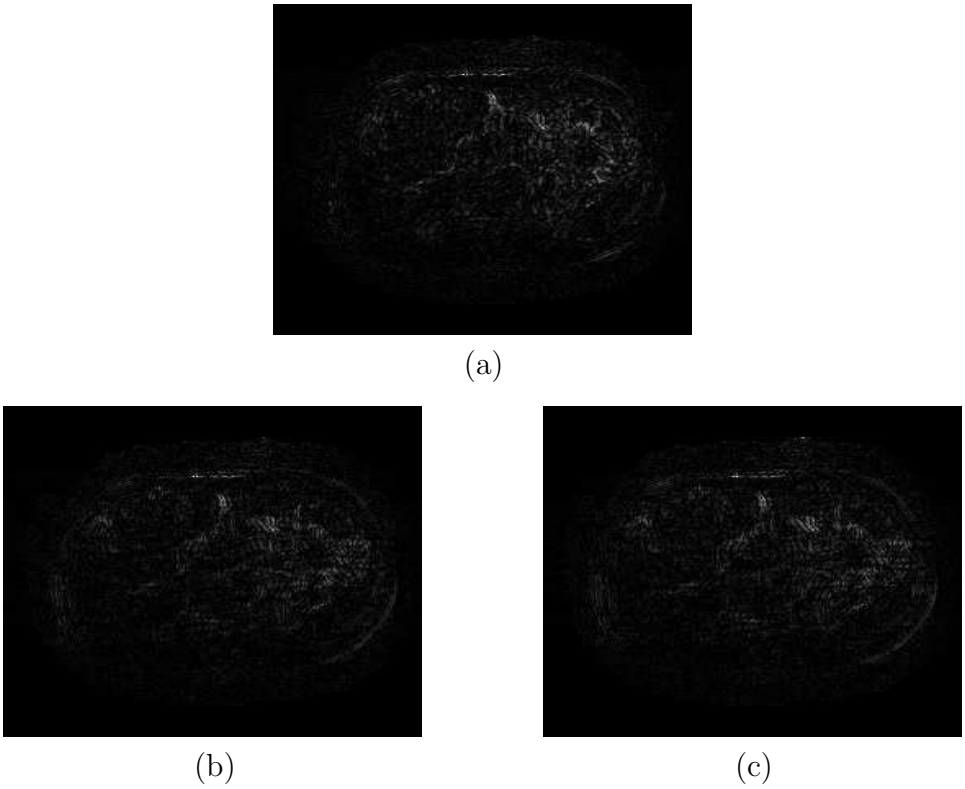

(a)

(b) (c)

Figure 2.19: Performance on a real abdomen data set: Comparison of error images computed from TRIGR reconstruction from 15% of k-space obtained with various masks (a) SS (b) ELL (c) RS (color scale for all images : 0 to 50)

expectation, it is observed that in some cases, when the fraction of acquired k-space increases, the reconstruction error also increases. This might be attributed to the possibility of increase in noise, in place of signal, in the acquisition.

The SS window is basically made of four triangles. Instead of triangles, we tried another window based on four Gaussian curves along each of the sides of the rectangle within the k_y-k_z plane, called Gaussian-shaped (GS) window. We carried out trials to make a comparative study between the two windows. For typical values of k-space fraction (0.2) and data dimensions along k_y-k_z of 256×36, the two windows are shown in Figs. 2.21(a) and (b), respectively. The GS window looks like a smoothed version of the SS window, and the two of them differ at very few locations. The similarity between the two windows is due to the skewness in the dimensions of data in k_y-k_z plane. The locations where the two windows differ are shown in Fig. 2.21(c). Here, the regions inside and outside the

marked ellipse belong to the lower and higher half frequency ranges, respectively. The SS window captures relatively greater number of points in the low-frequency region (corresponding to the white region), and lesser number of points in the high-frequency region (corresponding to the black region) than the GS window. Due to the aforementioned factor, the SS window provides more energy compaction than the GS window. The above argument holds true for any given fraction of k-space. This is because the step-size for SS-window is linear, while that for GS window is Gaussian in nature. The GS window falls rapidly from the peak along the smaller dimension (k_z), contrary to the gradual fall along the higher (k_y) dimension. We apply the two truncation windows on the real data

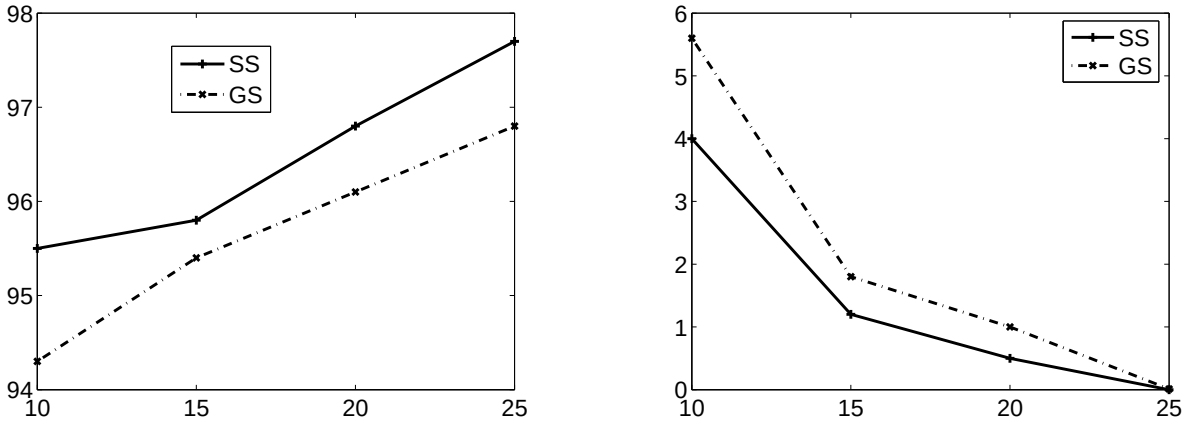

(a) (b)

Figure 2.20: Performance comparison between SS and GS windows on a real data set (a) Plot of percentage energy vs. percentage of k-space acquired (b) Plot showing comparison of the uptake slope error vs. percentage of k-space acquired

set shown in Fig. 2.5(a). Consistent with the observations made about the nature of data capture, we notice that the SS window captures greater k-space energy than the GS window, as shown in Fig. 2.20(a). The capture of greater k-space energy by the SS window leads to lower errors in uptake slope as shown in Fig. 2.20(b). Hence we observe that the smoothed version of SS window (GS window), does not result in improved performance.

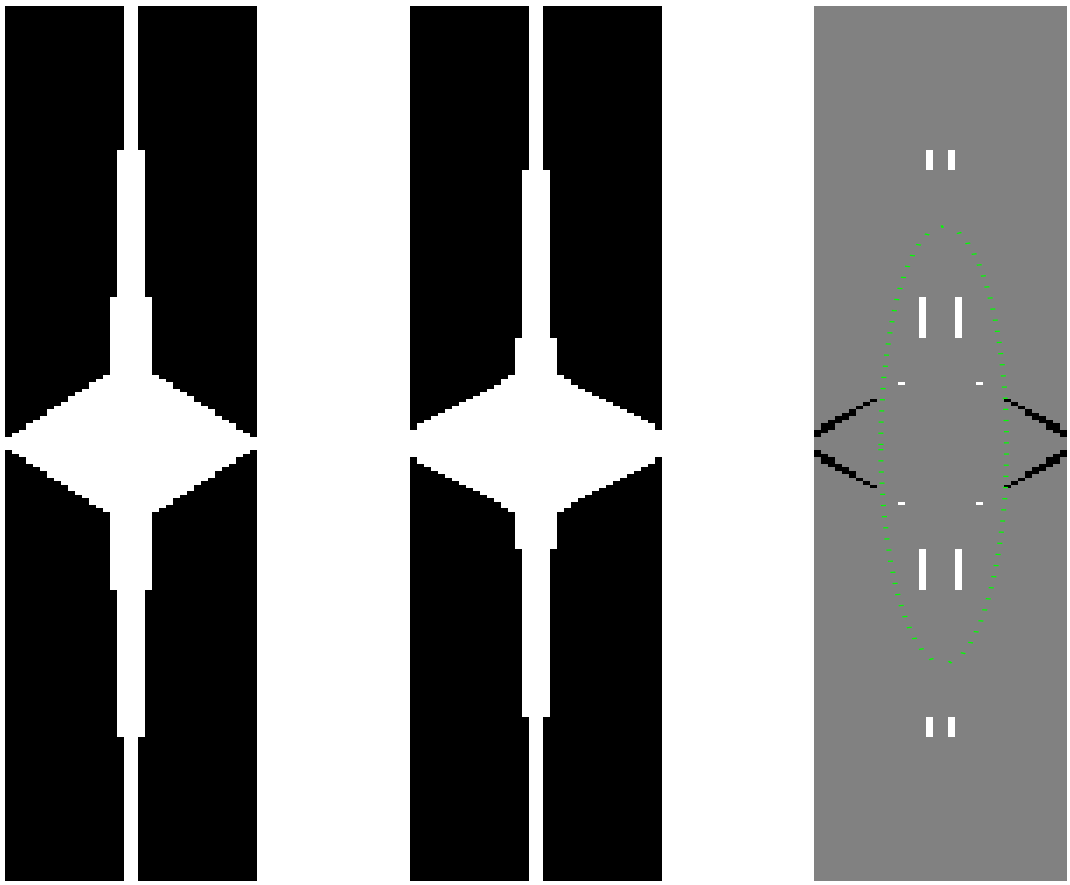

(a) (b) (c)

Figure 2.21: Comparison between SS and GS windows for k-frac of 0.2 and data dimensions along k_y-k_z of 256 $\times$ 36 (a) Star-shaped window (b) Gaussian-shaped window (c) Difference between SS and GS: White region marks the frequency points captured by SS and missed by GS masks; Black region marks the frequency points captured by GS and missed by SS masks. The ellipse separates the lower half k-space from the higher half k-space.

2.8 Conclusion

In this chapter, a novel star-shaped truncation window is proposed that achieves higher acceleration factors. The proposed window monotonically cuts down the number of samples acquired in k-space regions with lesser energy. It samples data within a star-shaped region centered around the origin in the k_y-k_z plane. The missing values are extrapolated using generalized series modeling-based methods. The proposed method is applied to several real and synthetic data sets. The superior performance of the SS window is illustrated using the standard measures of error images and uptake curve comparisons. Average values of enhancement curve slope error are compared over 5 real data sets of breast and abdomen images, for acceleration factor 8. The proposed window results in an error of 5%, while the values obtained using rectangular and elliptical windows are 12% and 10%, respectively.

Chapter 3

Improved k-t BLAST for dynamic imaging

Abstract

Modifications are explored for the popular dynamic imaging technique, k-t BLAST (ktB) for fMR imaging. ktB utilizes both the correlations in k-space and time, to reconstruct the image time series with only a fraction of the data. The algorithm works by unwrapping the aliased Fourier conjugate space of k-t (here called y-f space). The unwrapping process utilizes the estimate of the true y-f space, by acquiring densely sampled low k-space data. The drawbacks of this method include separate training scan, blurred training estimates and aliased phase maps. In this chapter, variations to ktB have been proposed to overcome these drawbacks. The proposed improved ktB incorporates variable-density sampling scheme, phase information from the training map and utilizes generalized-series extrapolated training map. The proposed technique is compared with ktB on real fMRI data. The proposed changes lead to a gain in temporal resolution by a factor of 6. Performance is evaluated by comparing activation maps obtained using reconstructed images. An improvement of up to 10 dB is observed in the PSNR of activation maps. Besides, a 10% reduction in RMSE is obtained over the entire time series of fMRI images. Peak improvement of the proposed method over k-t BLAST is 35%, averaged over 5 data sets.

3.1 Introduction

Images with high spatial and temporal resolution are essential in medical diagnosis involving dynamic contrast-enhanced MRI or functional MRI, where dynamic events are monitored. Today, fMRI has the potential to probe neurophysiological activation in the brain at a much higher spatial resolution than that offered by other non-invasive neuroimaging techniques like PET. The high sensitivity measurement of "Blood Oxygenation Level Dependent" (BOLD) signal modulation points to regions in the cortex responsible for a specific activity. Currently fMRI applications interrogate neural activity changes only on the order of seconds, although neural activity happens on time scales of the order of milliseconds.

In order to facilitate dynamic imaging, one needs to determine the adequate temporal and spatial sampling rates, which has been extensively researched [21, 32, 62]. Enhancement changes that occur in tumors due to contrast uptake, are continuous and aperiodic functions, while dynamic events such as cardiac activity and typical brain-study experiments are periodic or quasi-periodic functions. The periodicity of the dynamic events leads to discreteness in temporal frequency. This sparseness in distribution has been explored, leading to strategies entirely different from the discussions in the previous chapter.

In the work reported in [73], the authors represent the continuously changing object in a multi-dimensional space, as a function of spatial frequencies (k_x,k_y) and a temporal variable (t). The Fourier conjugate of this multi-dimensional space corresponds to x-y-f-space, which is equivalent to the former in terms of energy, based on Parsevals theorem. The sparse energy distribution in x-y-f-space, is explored to determine sampling schemes that can effectively trade-off between spatial and temporal samples. The work reported in [38] utilizes a generalized harmonic model for dynamic imaging of objects with periodic or quasi-periodic time variations. The approach converts the problem to one of parameter identification. "UNaliasing by Fourier-encoding the Overlaps using the temporal Dimension" (UNFOLD) [42] has been proposed by Madore et al. in order to speed up acquisition exploiting the periodicity of the underlying event. The method hinges on

transfer of information from the k axes to the t axis, making it sufficient to acquire a smaller but denser k-t space. UNFOLD involves a reduction of the dynamic FOV. This FOV reduction diminishes the amount of spatial information acquired along the k axes of k-t space. Because of aliasing, spatially distinct points within the object are overlapped at the same spatial position in the images. UNFOLD uses time to label the overlapped components, such that a Fourier transform through time can resolve them. The authors present results on cardiac and fMR imaging, illustrating significant reductions in the acquisition time. Recently, a method for dynamic imaging of periodic and quasi-periodic events, called k-t BLAST has been proposed [67]. In this chapter, we study this method and propose variations for improved performance.

3.2 *k-t BLAST*

k-t BLAST (ktB) was proposed by Tsao et al. [67], for reconstruction of dynamic images using regularly undersampled data acquisitions. The correlations in both k-space and time are exploited for estimating the unacquired data. A missing data point is estimated based on other available points, within its vicinity in both k-space and time. This approach exploits more of the relevant correlations, thus improving the estimation of missing data. This improvement could be used to obtain better reconstructed images or achieve higher reduction in data acquisition leading to better temporal resolution. Several variations of ktB have been proposed to customize the image reconstruction algorithm for applications such as angiography and cardiac imaging [31, 30, 7]

Dynamic MRI can be seen as acquisition of a changing k-space signal at different time instants, which is essentially sampling in a higher dimensional k-t space. Here, k stands for multi-dimensional k-space. Since we are dealing with $2D$ k-space, and it is known that all points along the read-out (k_x) dimension are available, we need to undersample only along phase-encode dimension (k_y). Hence, the mention of k-axis would refer to the actual k_y axis, whose Fourier conjugate axis would be the spatial dimension y. The images in Fig. 3.1 explain the working of the ktB. The lattice along which these points are acquired

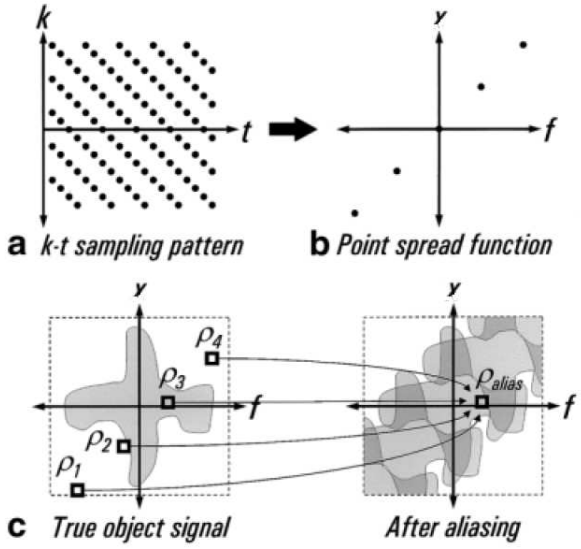

Figure 3.1: Knowledge of the sampling pattern helps in unaliasing the y-f space (Source: [67])

in k-t space is referred to as the k-t sampling pattern. The conjugate space obtained upon Fourier transformation of the k-t space is the y-f space. It is observed that the signal distribution in y-f space is very sparse, especially for fMRI with its temporal periodicity of activated pixels. This feature can be used to pack y-f space densely, allowing higher acceleration factors. Under-sampling in k-t space leads to an aliased signal distribution in y-f space. For instance, at a given location (y_0, f_0) in the aliased y-f space obtained from the sparsely acquired data, the signal value $\rho_{alias}(y_0, f_0)$ is actually the sum of the values at $(y_1, f_1) \ldots (y_n, f_n)$ on the true y-f space signal distribution. The locations $(y_1, f_1) \ldots (y_n, f_n)$ are determined by the k-t sampling pattern.

$$\rho_{alias}(y_0, f_0) = \rho_1(y_1, f_1) + \ldots + \rho_n(y_n, f_n) \tag{3.1}$$

where n is the acceleration factor.

Unaliasing the aliased y-f signal distribution is possible because the aliasing pattern

is completely known, once the sampling pattern is fixed. This under-determined system in equation (3.1) needs to be solved for every set of aliased voxels. Since infinite solutions exist, the most sensible way would be to minimize a well-designed cost function. Here, weighted-minimum norm solution is preferred. This solution makes use of prior information, wherein a low resolution, alias-free signal distribution is obtained by acquiring the low k-space frequencies, forming the "training map". The values of the training map form initial estimates in order to obtain the solution given by,

$$\rho = \mathbf{M}^2.\mathbf{1}^H(\mathbf{1}.\mathbf{M}^2.\mathbf{1}^H)^{-1}.\rho_{alias} \tag{3.2}$$

where, $\mathbf{M}^2 = diag(|m_1|^2, \ldots |m_n|^2)$, and $|m_i|$ is the magnitude of the training y-f map at the ith aliasing location. Here, $\mathbf{1}$ is the row vector of all 1s, at n positions. Note that the acquisition of the training map data slightly reduces the speed-up effected by the under-sampling pattern. However, the DC-value is separately taken care of, since it is the most important component. The temporal average of the sparse acquisitions forms the DC-value of the estimated y-f map.

The new set of equations to be solved is given by,

$$\rho = \underline{\rho} + \mathbf{M}^2.\mathbf{1}^H(\mathbf{1}.\mathbf{M}^2.\mathbf{1}^H + \psi)^{-1}.(\rho_{alias} - \mathbf{1}\underline{\rho}) \tag{3.3}$$

where, $\underline{\rho}$ is the baseline estimate (DC-component) and ψ is the noise variance.

3.3 Improvements proposed

3.3.1 Data acquisition

In the original ktB scheme [67], the training and the actual data are acquired at disjoint instants of time and follow different sampling schemes. The training data contains only the low k-space frequencies, while the actual data acquisition is along a pre-designed sparsely sampled lattice, as shown in Fig. 3.2(a). A variation of data acquisition scheme

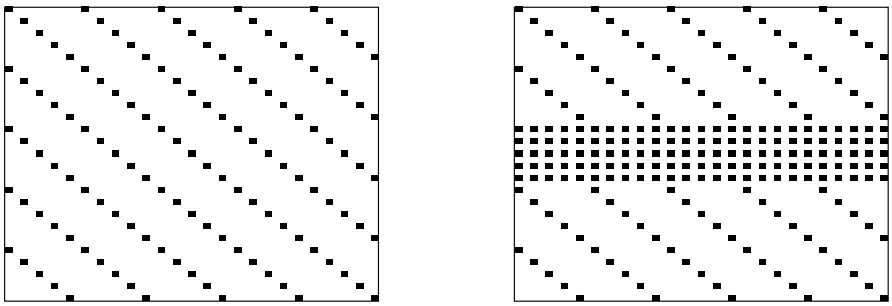

(a) (b)

Figure 3.2: Data acquisition schemes (a) Uniform density (used in ktB). (b) Variable density (utilized by the proposed method)

that couples both the training and actual scans is shown in Fig. 3.2(b). This is a variable density sampling lattice. This scheme has been designed to minimize the mismatch between the training and the data scans. This scheme of acquisition reduces the acceleration factor achievable, but eliminates possible artifacts due to mis-registration. We have utilized the variable-density sampling scheme for our experiments.

3.3.2 Training map

The work reported in [15], deals with how the quality of the training data influences the working of ktB, in contexts where the training and the actual data are acquired at disjoint instants of time. It reports that increasing the number of time frames for which the training data is acquired, results only in a negligible decrease of reconstruction error.

However, in a variable-density acquisition scheme like ours, thetraining data is available at all the time frames of the experiment. We explore the impact of including higher frequencies in the training data, on the working of ktB. We compare ktB reconstructions that use low k-space frequencies in the training data against these using all the k-space frequencies (ideal training data) in the training map. It is seen that the errors can be brought down by a factor of 2, using higher frequencies in the training map. The disparity between the qualities of the two image reconstructions led us to explore the possibility of

obtaining an improved resolution training-map using the acquired low k-space frequencies. It must be observed that at locations in the aliased y-f space, where the signal is dominated by noise, the values from the training map that are chosen as estimates can lead to meaningful results only if the estimate is close to the truth.

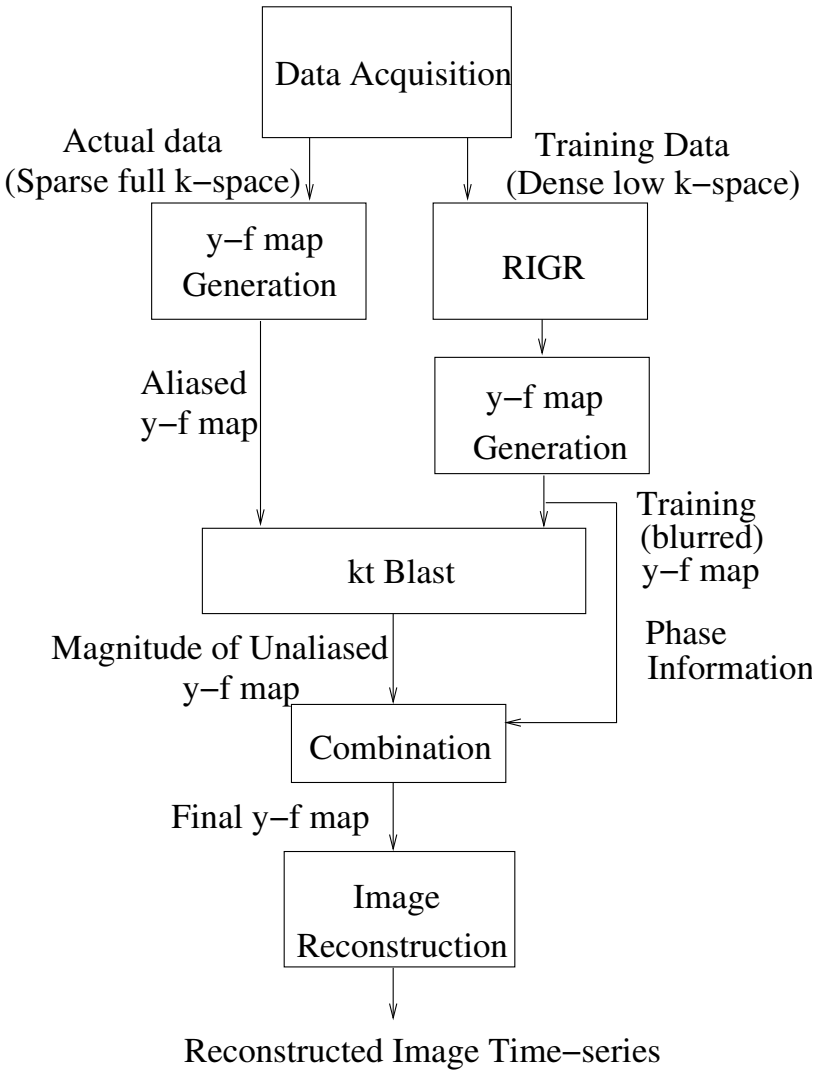

Figure 3.3: Overview of the proposed method (ktB-PR: ktB with unaliased phase (P) and RIGR-extrapolated (R) training map)

Figure 3.3 shows a block diagram of the proposed method, which generates an improved training map, despite acquiring only the lower spatial frequencies. This is achieved by extrapolation using the generalized series-based method called RIGR (Reduced-encoding

Imaging by Generalized-series Reconstruction). ktB with RIGR-extrapolated training map is referred to as ktB-RIGR in this work. In order to utilize RIGR for extrapolation, one static full k-space data acquisition is required. This static acquisition is required for the estimation of the unacquired higher k-space frequencies, as outlined below.

Generalized series modeling

In generalized series modeling, the missing high spatial frequencies are split into two components as follows :

$$d_{GeS}(k) = d_c(k) + \sum_m c_m d_c(k - m.\Delta k) \tag{3.4}$$

where, d_{GeS} is the generalized series estimate, d_c is the Fourier transform of the static image, c_m are the generalized series coefficients and Δk refers to the spatial-frequency resolution. The first term incorporates the apriori static information, whereas the second term comes by adaptively adjusting the coefficients so that data consistency is maintained. We implemented a fast version of this algorithm outlined in [40]. After this extrapolation, the deviation of the training data from the ideal, full k-space training data decreases. We expect better training data to translate to better training maps in y-f space.

3.3.3 Phase constraints

The second change proposed is the incorporation of phase constraints from the training map. The training map, though not of best possible resolution, does contain unaliased signal distributions. In (3.3), as given in the original k-t $BLAST$ proposition, the phase of the aliased y-f map is used, which would be erroneous. Hence, we use the phase information of the training map in estimating the true y-f map. ktB with phase constraints from the training map is referred to as ktB-Ph in this work.

$$\Theta = \angle\rho_{train} \tag{3.5}$$

$$\tilde{\rho} = |\rho| \exp(i\Theta) \tag{3.6}$$

where, $\tilde{\rho}$ is the final estimate of the signal distribution in y-f plane and ρ_{train} is the training map.

3.4 Experiments and results

3.4.1 Data utilized for the study

fMRI data is obtained using "visual stimulus". In the course of the experiments, 3 two-dimensional T_2^*-weighted images, each with 64 scans, are acquired using a gradient-echo FLASH sequence. The acquisition parameters are: TE/TR = 40 msec/80.5 msec, matrix size = 128 × 64; slice thickness = 5-mm and 2-mm gap. The image matrices are zero-filled to obtain images of size = 128 × 128, with a spatial resolution of 1.953 × 1.953 mm; The corresponding two-dimensional anatomical slices are also acquired with a T_1-weighted IR RARE sequence (TI = 900 msec; TE/TR = 3900 msec/40 msec, matrix size = 512 × 512) in the same experiment session. In all the experiments, ON and OFF stimuli are presented at a rate of 5.162 sec/sample. Each stimulation period had four successive ON states followed by four OFF states. The stimulations are repeated for eight cycles, thus resulting in an acquisition time of 5.5 min. The experiments are carried out at different sessions with different subjects. The visual stimulation task comprised an 8-Hz alternating checkerboard pattern with a central fixation point projected on a LCD system. The subjects are asked to fixate on the point during stimulations. Images are acquired at three axial levels of the brain at the visual cortex.

3.4.2 Performance evaluation

fMRI images are mainly studied for the activation maps, which interpret the information contained in the entire time series of images. Hence, to evaluate the reconstruction performance, we compare the activation maps obtained against the reference activation map. Statistical parametric mapping (SPM2) is the most widely used method for fMRI time-series analysis [9]. The primary objective is to detect activated voxels and the resulting

statistical parametric maps represent the activation strength of each voxel. The scale of the activation-strength obtained is important, since the activation maps are eventually thresholded to obtain the truly activated regions. Hence, when drastic changes in the scales of activation-strength are observed, the activation maps are considered degraded. Root mean square error (RMSE), correlation with reference, and mean activation level of the maps are the performance metrics used to quantify the degradation in activation. If we analyze the true image time series A and the reconstructed series B, using same SPM method and parameters, we expect comparable scales in activation strength at similar locations in the resulting statistical parametric maps S_A and S_B.

fMRI time-series are first realigned to remove movement effects using least-squares minimization [9] and then smoothed using 3D Gaussian kernel with full width at half maximum (FWHM) = 4.47 mm, to decrease spatial noise. Canonical hemodynamic response function (HRF) plus time and dispersion derivatives are used as basis function and changes in BOLD signal associated with the task are assessed on a pixel-by-pixel basis, using the general linear model and the theory of Gaussian fields as implemented in SPM2. This method takes advantage of multivariate regression analysis and corrects for temporal and spatial autocorrelations in the fMRI data. Those voxels in the statistical parametric map are identified as activated, that satisfy $p \leq 0.05$, on carrying out the F-test.

3.4.3 Experimental results

MATLAB is used for all simulations. For our trials, the training and the actual acquisitions are generated from the full k-space, by using the appropriate under-sampling masks. The unaliased training as well as aliased sparse y-f maps are shown in Figs. 3.4 (a) and (b), respectively. As claimed earlier, it can be seen that the signal distribution in y-f space is very compact, thus leading to possibilities of achieving higher acceleration factors. In Fig. 3.5 (a), the deviation of the training data from the ideal training data is shown for 2 cases. In the first case, the training data is simply zero-padded as in the baseline ktB, whereas in the second case, the obtained low k-space frequencies are RIGR-extrapolated.

(a) (b)

Figure 3.4: Typical y-f maps obtained from k-space data acquisition for acceleration factor 5 using : (a) Densely sampled low k-space (Training data) (b) Sparsely sampled full k-space (Actual data)

Clearly, the RIGR-extrapolated data is seen to be closer to the ideal training data. In Fig. 3.5 (b), we compare how the gains of Fig. 3.5 (a) translate to the y-f space. It can be observed that the RIGR-extrapolated training map is close to the training map that would have been generated had all the frequencies been available for training (ideal training data) and is more accurate than the zero-padded map that the ktB algorithm uses. In Fig. 3.6(a), we see errors in the reconstructed y-f plane as compared to the true y-f plane. The three cases compared are : The training map being ideal (ktB with ideal training data), zero-padded (ktB) and RIGR-extrapolated (ktB-RIGR). It can be seen that the RIGR-extrapolated case results in errors lower than that of the zero-padded case, consistently for all the instants of the time series. In Fig. 3.6(b), the time series of RMSE, in image reconstruction in all the three cases outlined above, is shown. It can be seen that the RIGR-extrapolated case and the ideal training map case, are quite comparable, while both consistently outperform the baseline ktB reconstruction. Fig. 3.7 shows the decline in correlation of the obtained activation map with the reference map as a function of the acceleration factor. In Fig. 3.8, we observe the activation maps obtained using the two methods, for a gain of factor 5 in temporal resolution. Clearly, the map obtained using baseline ktB displays more artifacts than the proposed method. We also observe that the gain in PSNR goes up to 10 dB. The RMSE of the fMRI time series reduces by

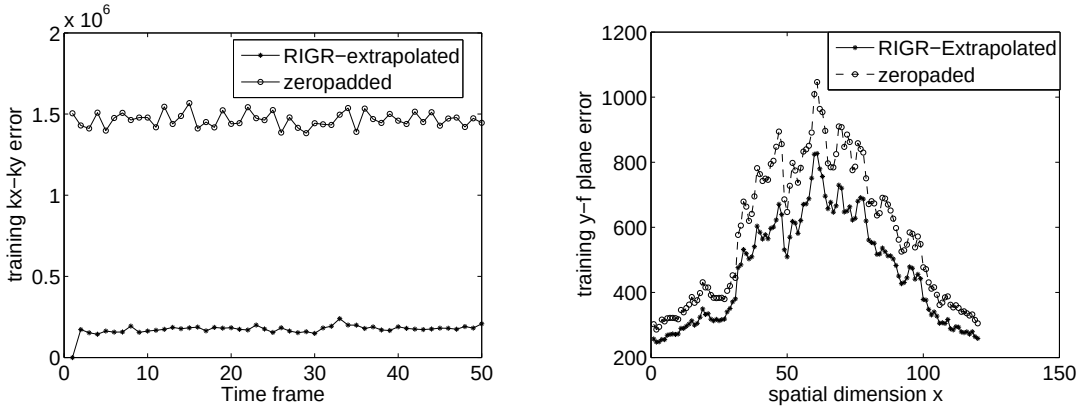

(a) (b)

Figure 3.5: Errors for acceleration factor 5 in : (a) Training k-space data with respect to the ideal training data. (b) y-f training map with respect to the ideal y-f training map.

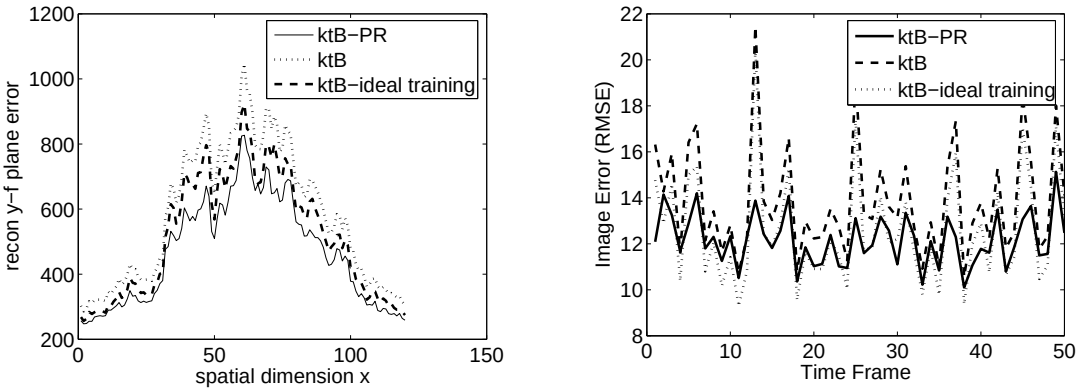

(a) (b)

Figure 3.6: Reconstruction errors for acceleration factor 5 in : (a) y-f map. (b) RMSE of the reconstructed image time series.

about 10% averaged over all the time points, with a peak improvement of 35% compared to the baseline ktB for acceleration factors up to 6. For acceleration factor of 6, we notice that the scales of activation maps obtained using the baseline ktB are lower by a factor more than 10, and hence, it is not possible to threshold them to see activated regions. On the other hand, ktB-PR results in activation maps that are lower by only a factor 2 and hence activated regions can be seen even at lower thresholds. At acceleration factors above 6, we notice significant degradation in the strength of the activation maps, and hence do not consider them.

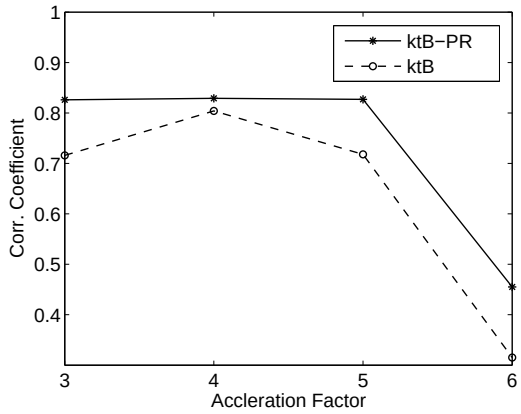

Figure 3.7: Correlation of the obtained activation map with the image time series reconstructed using ktB-PR with accelerated data acquisition, with respect to the reference activation map obtained using the original image time series.

(a) (b) (c)

Figure 3.8: Thresholded activation maps obtained using SPM for acceleration factor 5, with the image time series reconstructed using : (a) Original images (b) ktB-PR (c) ktB

3.5 Discussion

The image shown in Fig. 3.9(a) is a sample from the chosen fMR time series. Applying the ktB algorithm, we obtain the reconstruction shown in Fig. 3.9(b). The corresponding error image is shown in Fig. 3.10(a). Now, the same image is reconstructed with a change in the training data set. We assume the case where all possible data is available for training (ideal training data). The error image for the obtained reconstruction in this case is shown in Fig. 3.10(b). We have also carried out trials where only one of the two proposed changes are made to the existing algorithm. We compare the results (image reconstructions) for each of the following cases separately :

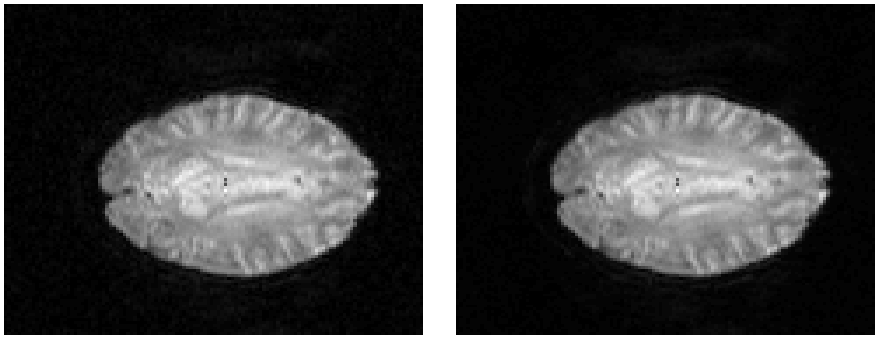

(a) (b)

Figure 3.9: (a) Sample fMR image from a time series of images. (b) Corresponding ktB reconstruction (Color scale for all images : 0 to 255)

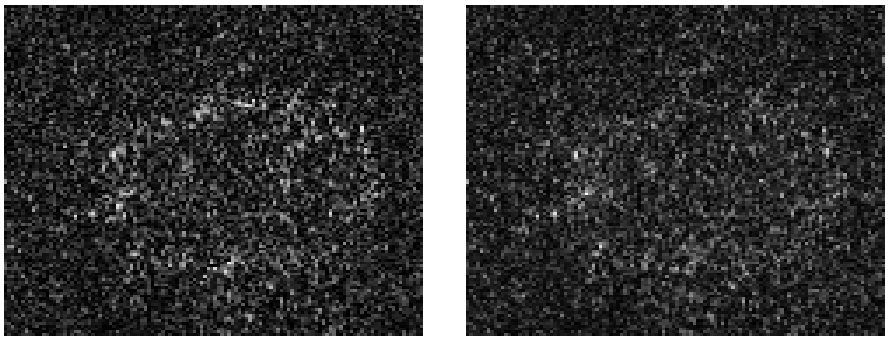

(a) (b)

Figure 3.10: Comparison of reconstruction performance for the image in Fig. 3.9(a). Error image for ktB with : (a) Regular training data (b) Ideal training data (Color scale for all images : 0 to 14)

- Only phase constraints are imposed (ktB-Ph)
- Only generalized series-extrapolated (RIGR) training map (ktB-RIGR)
- Both the above variations incorporated (ktB-PR)

The error images obtained from the three separate cases of image reconstructions are shown in Fig. 3.11. It is observed that incorporating both the proposed variations (ktB-PR) leads to a reconstruction better than the baseline ktB. The plot in Fig. 3.12 shows the RMSE obtained for an entire image time series using the variations of ktB discussed in this chapter, that include ktB with phase constraints but no RIGR-extrapolated training

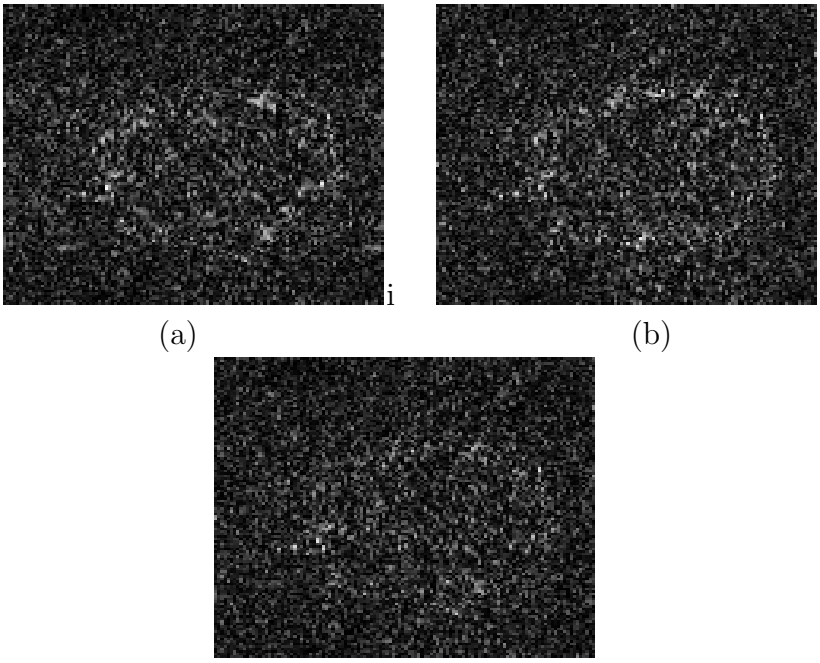

(a) (b)

(c)

Figure 3.11: Reconstruction performance of the proposed improvements on the image shown in Fig. 3.9(a). Error images using ktB with: (a) Only phase constraints (b) Only RIGR-extrapolated training map (c) Variations utilized in both (a) and (b). (Color scale for all images : 0 to 14)

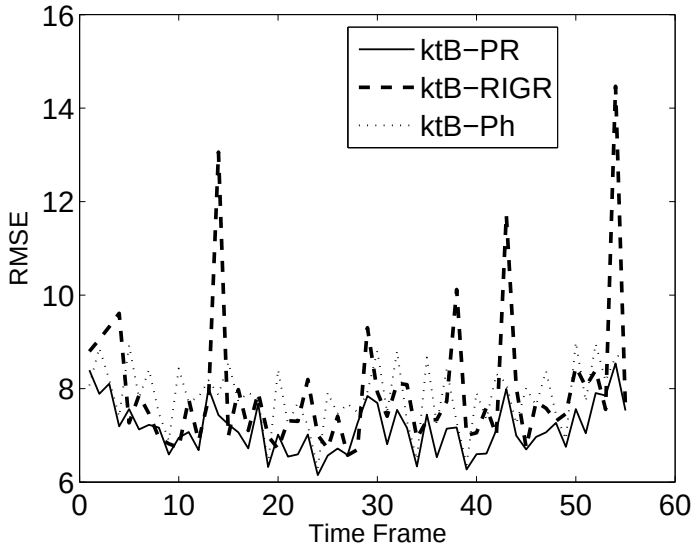

Figure 3.12: Performance comparison of each of the proposed variations to ktB, separately applied. For each of the time series RMS error is plotted from the error images.

map (ktB-Ph), ktB with RIGR-extrapolated training map but no phase constraints (ktB-RIGR) and finally ktB with both the improvements included (ktB-PR). It is observed that ktB-PR results in the least RMSE for the reconstruction of the image time series.

3.6 Conclusion

In this chapter, we have proposed an improved version of the existing dynamic imaging technique ktB. A variable density data acquisition scheme has been proposed, in order to avoid a separate training scan. The generalized-series extrapolated training map is used in place of the zero-padded training map to serve as an estimate of the true signal distribution. Besides, the phase-constraints from the training map rather than from the aliased training map are included in the final solution. All of the above changes are incorporated into the algorithm and applied to real data. Results on fMRI data have shown that these changes together lead to improved reconstructions and acceleration factors of up to 6. The reconstruction performance is evaluated using the activation maps obtained. We observe up to 10 dB improvement in the PSNR of the activation maps. The proposed technique results in more accurate activation maps and also a mean RMSE of less than 10% averaged over the entire time series, for acceleration factors up to 6.

3.7 Acknowledgements

We would like to thank Prof. Jagath Rajpakse, NTU, Singapore for sharing the fMRI and to his student Ms. Juan Zhou for carrying out the SPM analysis.

Chapter 4

CRAUNN for Cartesian parallel MR imaging

Abstract

In rapid parallel MR imaging, image reconstruction is computationally demanding. We propose image reconstruction utilizing the neural network framework, called "Composite image Reconstruction And Unaliasing using Neural Networks" (CRAUNN). Here, variable-density data acquisition is followed, where low k-space frequencies are densely sampled, while the rest are sparsely sampled. The images obtained using the densely sampled low frequencies are used to train the neural network. The densely sampled central k-lines are used to obtain the unaliased but blurred coil images and the corresponding composite image. The dense lines are then undersampled to obtain the corresponding aliased coil images. These aliased blurred images form the input training data set for the neural network. The corresponding output in this phase is the blurred unaliased composite image. The weights needed to generate the unaliased composite image from the aliased coil images are determined. Now the trained neural network is fed with images obtained using regularly undersampled full k-space data. The CRAUNN approach has been applied to phantom as well as real brain MRI data sets, and results have been compared with those of the standard existing parallel imaging techniques in the literature.

4.1 Parallel imaging

Parallel MR imaging is gaining popularity since it enables rapid imaging, leading to images with better spatio-temporal resolution. Parallel imaging was designed [23, 53] as a method to reduce the number of phase-encoding steps, the most time-expensive factor in MR Imaging. Here, multiple receiver coils are used in order to accelerate imaging. Each receiver coil is characterized by its spatial sensitivity function, which conveys information about the relative position of the origin of the received signal. The sensitivity profiles of the receiver coils are used as complementary encoding functions to phase encoding. Each coil provides a coil-weighted version of the image, all of which eventually can be combined to reconstruct the image. The information of the coil-sensitivities is crucial in obtaining the final reconstruction. Coil-sensitivities could vary with the object being imaged, and hence it is preferred to estimate them anew for each new scan. It is well-established that if each of the receiver coils could acquire the entire k-space, then the best estimate of the true k-space would be the "sum of squares" [35]. However, when the k-space at each of the receiver coils is sparsely sampled, then we need to devise better ways to combine the acquired signals, in order to reconstruct the image. Methods like SENSE [51], kt-SENSE [67], SMASH [64], PILS [13], GRAPPA [12], and kt-GRAPPA [56], are the known standard techniques used in parallel imaging.

4.2 Cartesian sampling

The most popular trajectory for sampling k-space is Cartesian shown in Fig. 4.1. Here, k-space is sampled along straight lines parallel to the k_x-axis. The advantage of Cartesian sampling lies in its ability to utilize FFT to obtain the image. To acquire k-space data, samples along k_x are acquired for a fixed value of k_y. This is carried out by clamping k_y to a fixed value by playing out $G_y(t)$ for the required time period, while $G_x(t)$ is kept constant since $k_x(t) = \frac{\gamma}{2\pi} t G_x(t)$. To cover the desired range of values of k_y, prior to acquiring each line, $G_y(t)$ is made to vary within a pre-designed set of values.

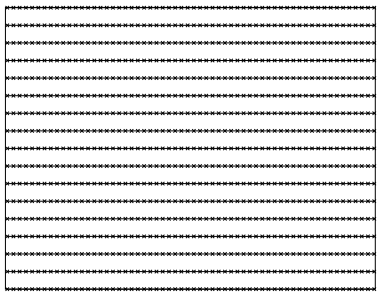

Figure 4.1: Cartesian sampling scheme : Horizontal(k_x) - Readout, Vertical(k_y) - Phase encode

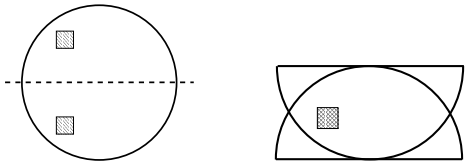

Figure 4.2: Illustration of the effect of downsampling. (a) True image. (b) Aliased image obtained with data downsampled by 2.

4.2.1 Sparse sampling and aliasing

Regular Cartesian sub-sampling of k-space is achieved by reducing the number of phase-encoding steps. This is accomplished by increasing the distance between the equidistantly sampled lines in k-space. The maximal values sampled along the k-axes remain the same. The effect of subsampling in the k-space manifests as aliasing in the image space. This is illustrated in Fig. 4.2.

4.3 Cartesian parallel MR imaging methods

Image reconstruction in parallel MR is computationally intensive, and depends on the sampling trajectory, data reduction factor, as well as the reconstruction approach employed. Some of the reconstruction strategies critically depend on the precision of coil sensitivity estimation. Problems of numerical instability might arise in the event of noisy acquisitions. A brief description follows of the prevalent methods to reconstruct images with undersampled data.

The method called SENSE, proposed by Pruessman et al. [51], has become very popular. SENSE combines the acquired signals in the image domain. Here, the coil sensitivity information is used to combine the coil-weighted aliased images. Let us assume i_1 and i_2 to be the true intensities at the pixels shown in Fig. 4.2(a). Let the sensitivities at these points be c_{11}, c_{12} and c_{21}, c_{22} for coils 1 and 2, respectively. Let the resulting intensity at the pixel in the aliased image (see Fig. 4.2(b)), due to coil 1 be α_1, and coil 2, α_2, respectively. Then we know,

$$\begin{aligned} c_{11}i_1 + c_{21}i_2 &= \alpha_1 \\ c_{12}i_1 + c_{22}i_2 &= \alpha_2 \end{aligned} \tag{4.1}$$

The framework in equation (4.1) is a linear system of equations, which will be over-determined, if the downsampling factor is less than the number of receiver coils. The existence of the solution demands invertibility of the sensitivity matrix, which in turn implies that the coil sensitivities be distinct. Regularized versions of SENSE have also been proposed which attempt at overcoming the problem of numerical instability. *kt*-SENSE makes use of the time-dimension, and exploits sparseness in the conjugate plane of *k*-*t*, referred to as *x*-*f* space. Hence undersampling in *k*-*t* space becomes feasible. Unaliasing is carried out with prior knowledge of the sampling pattern. A linear system of over-determined equations leads to the reconstruction of the image.

Partially parallel Imaging with Localized Sensitivities (PILS) is yet another technique used in parallel MR imaging, which works in the image domain. Here, each of the receiver coils is assumed to have a box-car function coil sensitivity profile over a distinct region of the object and zero elsewhere. In the event of accelerated data acquisition, the subimages periodically repeat due to aliasing. The knowledge of the coil sensitivity helps in extracting the subimages separately from each of the coils in order to generate the composite unaliased image.

Another technique has been recently proposed that works in the image domain utilizing *B*-splines [47, 48] for reconstruction in parallel imaging. The coil sensitivities are assumed

to be distinct, as in SENSE. The coil-weighted aliased images are linearly combined to obtain the final image. The reconstruction operator is determined by using low-frequency acquisitions. The same reconstruction operator is applied to the full k-space acquisition. The coefficients that linearly combine are expressed as a linear combination of B-splines. The parameters are obtained by minimizing the error for the low-resolution acquisition.

SMASH is a k-space technique, where the composite k-space is generated using signals acquired in the entire array of receiver coils. Each receiver coil, say p^{th} coil has a distinct sensitivity $C_p(x, y)$ at location (x, y). Forming appropriate linear combinations of component coil signals, we may generate composite sensitivity $C^{total}(x, y)$ given by,

$$C^{total}(x, y) = \sum_p n_p C_p(x, y) \approx \exp^{i(p\Delta k_y y)} \tag{4.2}$$

where, n_p are complex weight factors, p is an integer, and Δk_y is the resolution along k_y. In other words, the combined signal s^{tot}, generated from linear combinations of component coil signals s_p using the weights n_p from equation (4.2), is shifted in k-space by an amount $(p\Delta k_y)$.

Here, the coils are *designed* such that the linear combinations of their acquisitions generate the missing harmonics. However, it turns out that the harmonic fit may not be exactly sinusoidal, leading to artifacts in reconstruction. In auto-calibrated version of SMASH, called AUTO-SMASH [26] additional low k-space lines are acquired to determine the coefficients for the harmonic fit.

GRAPPA is also a k-space technique, which linearly combines the acquired lines to generate the missing lines. Here, a bunch of lines at the central k-space, called auto-calibration lines (ACS), is acquired along with the usual sparse acquisition. A "block" is defined as a single acquired line and $(A-1)$ missing lines, where, A is the downsampling factor. The concept in GRAPPA is explained in the Fig. 4.3.

Employing blockwise reconstruction, the missing data in coil p at the line $(k_y - m\Delta k_y)$, is obtained as:

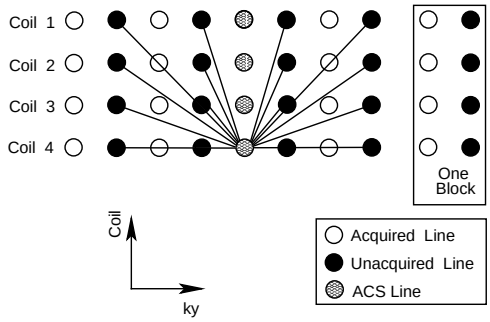

Figure 4.3: GRAPPA Estimation (Source: [[12]])

$$s_p(k_y - m\Delta k_y) = \sum_{l=1}^{L} \sum_{b=0}^{N_b-1} n(p,b,l,m) s_l(k_y - bA\Delta k_y) \tag{4.3}$$

where N_b is the number of blocks used in the reconstruction, l counts through the individual coils and b counts through the individual reconstruction blocks. The N_b lines which are separated by $A\Delta k_y$ are combined using the weights $n(p,b,l,m)$ to form each line, corresponding to a reduction factor A.

This process is repeated for each coil in the array, resulting in L uncombined single coil images, which can be combined using the known optimal ways. The estimation of the missing points depends on the size of blocks and the number of blocks considered. Here the reconstruction errors spread themselves across the image. The coil-design is not so critical, and hence the method brings some flexibility. *kt*-GRAPPA is an extension of GRAPPA that also utilizes information along the time-dimension.

4.4 Proposed image reconstruction

In conventional MRI, a single coil with homogeneous spatial sensitivity (body-coil) is used. The use of multiple receiver coils was originally proposed to improve image SNR. Images from the individual coils are separately reconstructed and then combined to yield a composite image, which serves as a benchmark for image quality comparisons with reduced data parallel imaging reconstruction schemes. The notations used here are adapted from [47]. The composite image (here, root-sum-of-squares) is assumed to be the true image.

The problem formulation is discussed here for Cartesian sampling. It can be seen that the same argument can be extended to non-Cartesian cases too.

For accelerated Cartesian data acquisition, where each coil under-samples the data, the image acquired from the l^{th} coil, S_l is given as,

$$S_l(x,y) = C_l(x,y)S(x,y) \tag{4.4}$$

where C_l is the complex sensitivity of the l^{th} coil, and S is the true image.

It is well-known that sparse sampling in k-space causes aliasing in the image domain. Consider the case where the maximum value of k_y sampled is N_y, and rectangular under-sampling by factor M is carried out. The aliased image obtained at the l^{th} coil, S_l^A is given by,

$$S_l^A(x,y) = \sum_{m=0}^{M-1} S_l(x, y + m\frac{N_y}{M}) \tag{4.5}$$

Substituting equation (4.4) in equation (4.5) we get,

$$S_l^A(x,y) = \sum_{m=0}^{M-1} C_l(x, y + m\frac{N_y}{M})S(x, y + m\frac{N_y}{M}) \tag{4.6}$$

The popular technique SENSE accomplishes image reconstruction by determining the individual unaliased coil images in the framework represented in equation (4.6), utilizing the prior knowledge of the values of coil sensitivities and acquisitions of the aliased coil images. The knowledge of the aliasing pattern determined by the acceleration factor is utilized to obtain the unfolding matrix. The unaliased coil images are finally combined to form the composite image. The solution is obtained in the least squares sense, and requires regularization in the event of noisy acquisitions.

In the proposed CRAUNN approach, the image reconstruction operator is assumed to be a function of the aliased coil images, processed pixel-wise. The reconstruction function,

(a) (b)

Figure 4.4: Illustration that the nature of aliasing does not vary appreciably with the extent of frequency content in the acquisition. PSF obtained using Cartesian undersampling by factor 2. (a) Using the entire range of k-space frequencies. (b) Using only low k-space frequencies.

$\mathcal{F}$, to estimate the composite alias-free image $\hat{S}$, is given as:

$$\hat{S}(x,y) = \mathcal{F}\left(S_l^A(x,y)\right) \tag{4.7}$$

where, $l = 1, 2, \cdots, L$. The function is allowed to be arbitrary in form and complexity, and is determined using neural networks. Thus, both the unaliasing and combining of coil images to generate the composite image are accomplished together by the neural network, without explicitly requiring the coil sensitivity estimation.

Figs. 4.4(a) and (b) illustrate that the nature of aliasing does not depend appreciably on the extent of frequencies available in the acquisition. The PSF obtained with the entire range of k-space frequencies shows sharp, localized peaks. On the other hand, the PSF obtained with low frequency acquisitions exhibit the peaks at precisely the same locations, but are smeared. Hence we deduce that the way to unalias can be determined using low frequency acquisitions and can be applied to the full k-space acquisitions. An overview of the proposed system is shown in Fig. 4.5.

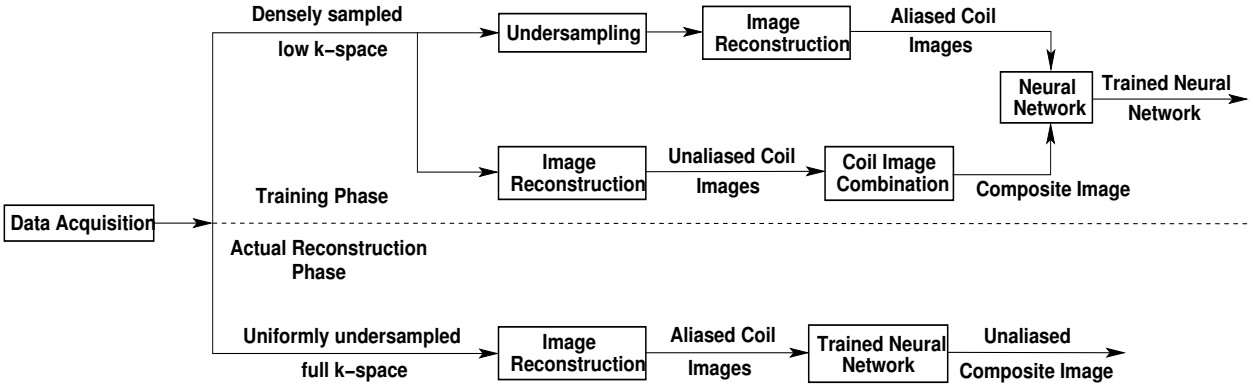

Figure 4.5: Image reconstruction by CRAUNN: The acquired data is selectively used to obtain images employed at different stages of the image reconstruction. The top leg of the block diagram represents the training phase, while the bottom leg represents the actual reconstruction phase.

4.4.1 Multi-layer perceptron (MLP) network

Neural networks have emerged as powerful mathematical tools for solving various problems like pattern classification and medical imaging, due to their ability to map complex characteristics, and learn. Of the many neural network architectures proposed, single hidden layer feed-forward network with sigmoidal or radial basis function is found to be effective for solving a number of real-world problems. The free parameters of the network are learned from the given training samples using gradient descent algorithm.

A typical MLP network consists of three or more layers of processing nodes (neurons): an input layer that receives external inputs, one or more hidden layers, and an output layer which produces the target outputs. Note that unlike other layers, no computation is involved in the input layer. The principle of the network is that when data is presented at the input layer, the network nodes perform calculations in the successive layers until an output value is obtained at each of the output nodes. This output signal should be the appropriate target value for each input data. Using universal approximation property [77], one can say that the single layer feedforward network with sufficient number of hidden neurons (N_h) can approximate any function to any arbitrary level of accuracy. It implies that for bounded inputs to the network, there exist optimal weights (not necessarily unique) to approximate the function. Hence, in our study, we use single hidden layer

network to approximate the functional relationship between the aliased coil images and the true image. Let $\mathbf{U}$ be the n-dimensional input feature vector ($\mathbf{U} \in \Re^n$), which is transformed into an N_h-dimensional vector $\mathbf{Y^h}$ as

$$y_i^h = f_a\left(\sum_{j=1}^{n} w_{ij}u_j\right) \quad i = 1, 2, \cdots, N_h \tag{4.8}$$

where w_{ij} is the connection weight between the j^{th} input neuron and i^{th} hidden neuron and $f_a(.)$ is the sigmoidal activation function. The bipolar sigmoid function is a common choice for the activation function, and is defined as

$$f_a(x) = \frac{1.0 - exp(-x)}{1.0 + exp(-x)} \tag{4.9}$$

The output (T) of the MLP network with N_h hidden neurons has the following form:

$$T = f_a\left(\sum_{j=1}^{N_h} v_j y_j^h\right) \tag{4.10}$$

where v_j is the connection weight between the j^{th} hidden neuron and the output neuron, and $f_a(.)$ is the sigmoidal activation function.

4.4.2 Back propagation learning algorithm

Back propagation (BP) is one of the simplest and most general methods for the supervised training of a MLP [57]. The basic BP algorithm works as follows:

1. Initialize all the connection weights ($\mathbf{W}$ and $\mathbf{V}$) with small random values from a pseudo-random sequence generator.

2. Compute the network output for the given input feature vector $\mathbf{U}$.

3. Let $\hat{T}$ be the target for the given input $\mathbf{U}$.

Calculate the deviation E of the network output from the target value as

$$E = \frac{1}{2}\sum\left(\hat{T} - T\right)^2 \tag{4.11}$$

4. Compute the negative gradient of error to update the network weights

$$\Delta w_{ij} = -\frac{\partial E}{\partial w_{ij}} \tag{4.12}$$

5. Update the weights using negative gradient of error E until the weights converge, i.e., the current error E must be equal to or smaller than the prescribed value.

4.4.3 Acquisition scheme

Full k-space 8-coil data is acquired for the experiments. Points from the acquired data are selectively chosen to form the testing and training data sets. A variable-density [66] sampling scheme is chosen, as shown in Fig. 4.6. Such schemes reduce the achievable acceleration factor, but also eliminate the need for separate training scans. It also reduces the artifacts that could arise due to mis-registration. The "root Sum of Squares"(SoS) image is assumed to be the gold standard image. The central k-space is densely sampled (32 lines in our experiments) at each of the receiver coils. The corresponding SoS reconstruction is the blurred unaliased image. The densely sampled lines are separately undersampled to form the blurred, aliased coil images, which along with the corresponding SoS image, form the training data set to the neural network. This data set establishes the functional relation between the aliased images and the corresponding unaliased version. The weights associated with the neural network topology are now determined. The trained neural network is now fed with full k-space aliased coil images, to obtain the final image reconstruction.

The neural network architecture used here is a single hidden layer feed-forward network with radial basis functions. The input layer consists of 18 nodes, while the output layer is

Figure 4.6: Variable density sampling scheme utilized for the study

made of a single node. The hidden layer has 98 nodes. The system that we aim to build works in two phases : training phase and reconstruction phase, as shown in Figs. 4.7 and 4.8, respectively.

Features

The input layer of the neural network is fed with features extracted from one pixel of all the aliased coil images at a time. The features used here are the spatial coordinates of the pixel and its complex intensity from each of the coil images. Here, since we happen to use 8-coil data, we have 8 complex coil images. At a fixed location, for all the 8 coils, we obtain 8 complex numbers which are split into their real and imaginary parts ($2 \times 8 = 16$). The spatial co-ordinates ((x co-ordinate, y co-ordinate) = 2) for that location, are concatenated, making the length of the feature vector 18. It must be noted that the inclusion of the spatial co-ordinates in the feature vector, facilitates the transformation to be spatially varying. In the training phase, features are extracted from the images constructed using only low frequencies. In this phase, for every feature vector, the corresponding output also needs to be specified. At a given location, corresponding to the feature vector assembled as explained above, the neural network output is the pixel intensity at the corresponding location in the alias-free composite image. In the reconstruction phase, features are extracted from images containing the entire range of frequencies. Unlike the

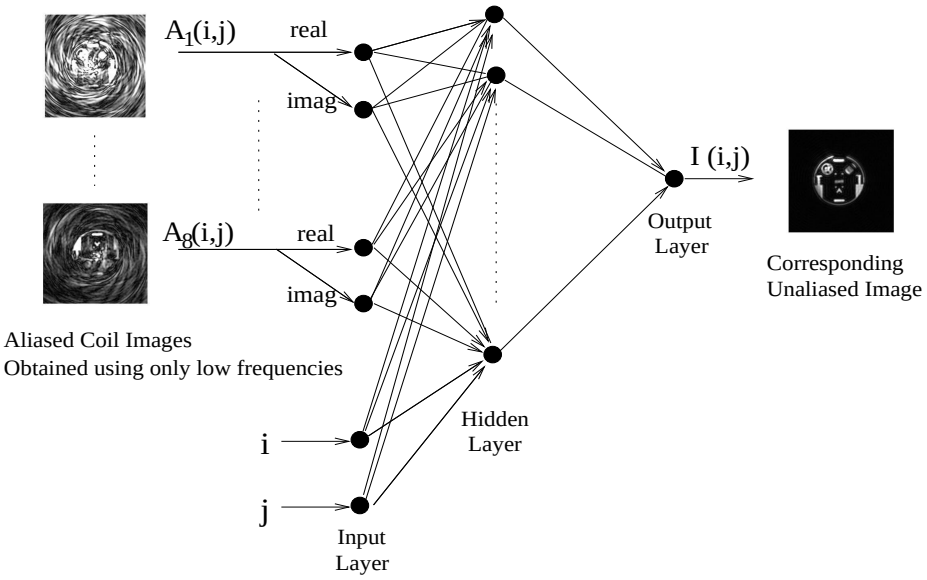

Figure 4.7: Training phase of the proposed system. The inputs are pixel-wise aliased coil image intensities as well as the pixel location, while the output is the corresponding pixel intensity of the composite alias-free image. Images here contain only low frequencies.

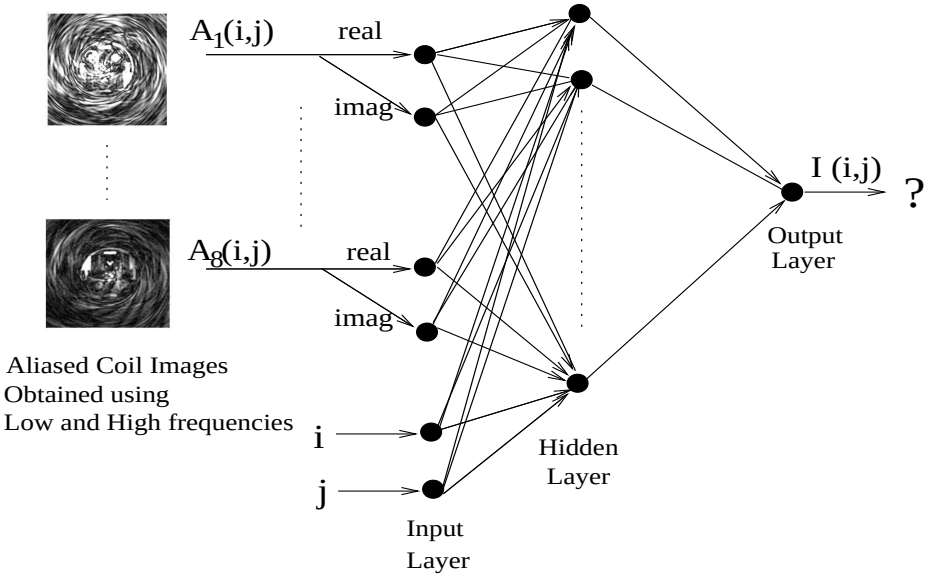

Figure 4.8: Reconstruction phase of the proposed system. The inputs are pixel-wise aliased coil image intensities as well as the pixel location; The output is the estimate of the desired image. The images contain both low and high frequencies uniformly undersampled.

training phase, here, the output is estimated by the network. The outputs put together from each and every location, form the reconstructed image.

Neural Network parameters

The activation functions used are all sigmoidal functions. The learning rate is chosen such that the error between iterations reduces rapidly enough for quicker convergence, but does not get trapped at local minima. Experimentally it was found that setting the learning rate below 10^{-6} resulted in the error between iterations to reduce too slowly, while setting the learning rate greater than 10^{-6} resulted in oscillatory behavior between iterations. Hence, the learning rate was set to 10^{-6}. The choice of the number of hidden neurons decides how smoothly the target function can be modeled. In practical situations, the appropriate number is chosen across several trials, where we start with a fixed number greater than at least four times the length of the feature vector, as a rule of thumb. The number is increased gradually and the corresponding training error is observed. The training error hits a minimum at a point, and thereafter gradually increases. The number of hidden neurons is clamped at the value where the training error is measured to be the least. Here, it turns out to be 98. We assume convergence when the training error reaches 10^{-3}.

4.4.4 Validation criterion

Generally errors in image reconstruction are quantified using error images, with indices like mean square error and PSNR. However, it is also widely acknowledged that these indices do not correlate well with the visual assessment of the images [71]. Hence, we use a similarity index to quantify the closeness of the reconstructed image to the original image, called "Structural SIMilarity" index (SSIM) [70]. This is similar to the evaluation criterion utilized in [59], where human visual perception is considered in order to determine the quality of the MR images.

SSIM

The SSIM index penalizes loss in structural correlation, intensity and contrast. SSIM at location (p, q) is given by, $SSIM(p, q) = [l(p, q)]^{\alpha} c(p, q)]^{\beta} s(p, q)]^{\gamma}$, where l, c and s reward similarities in intensity, contrast and structure, respectively. Since all the three are given the same weightage, α, β and γ are all chosen to be equal to 1. A small local neighbourhood is chosen to determine the point-wise attributes. Here, $l(p, q) = \frac{2\mu_1\mu_2}{{\mu_1}^2+{\mu_2}^2}$, where μ_1 and μ_2 are the average neighbourhood intensities in the two images being compared. The contrast comparison function is given by, $c(p, q) = \frac{2\sigma_1\sigma_2}{{\sigma_1}^2+{\sigma_2}^2}$, where σ_1 and σ_2 are the respective standard deviations around the compared pixels. Standard deviation σ is the square root of variance, and is an unbiased estimate of the signal contrast. The structural comparison function is given by, $s(p, q) = \frac{\sigma_{12}}{\sigma_1\sigma_2}$, which turns out to be the correlation (inner product) between the structures being compared. Structure comparison is carried out only after intensity subtraction and variance normalization.

This is a widely used full-reference image quality metric, given a reference image and its distorted version. The SSIM score ranges from 0 to 1, where 0 represents the worst and 1 stands for the best quality of reconstruction. The index is developed based on the assumption that the structural information of the image is the most critical in determining the perceived quality of the image. This metric is generally used for image/video quality assessment. It is claimed by the authors to correlate well with subjective test results, illustrated for a wide variety of images.

4.5 Data used and results

A typical instance of reconstruction of a point using an undersampled acquisition is shown in Fig. 4.9. The artifacts in the reconstructed point depend on its position, and hence this reconstruction operator is not spatially invariant. The proposed method is applied to synthetic and real data sets. The standard "Shepp-Logan" phantom and its corrupted versions form the synthetic data sets. The real data sets used are a structural brain data set and a functional MR data set.

(a) (b)

Figure 4.9: Reconstruction of a point with an undersampled acquisition using CRAUNN (a) Direct reconstruction (b) Reconstruction using CRAUNN

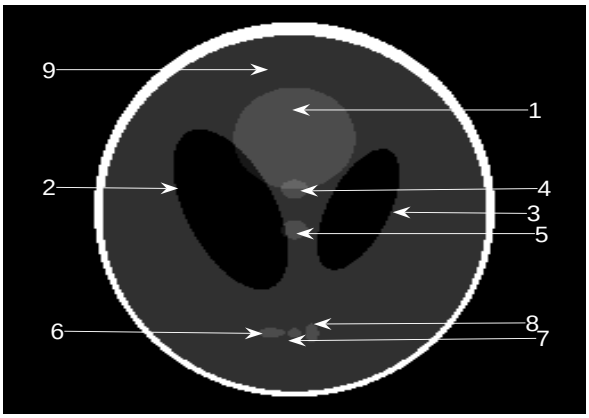

Figure 4.10: Shepp-Logan phantom with distinct regions labelled

4.5.1 Phantom data

The CRAUNN technique is applied to the standard "Shepp-Logan" phantom shown in Fig. 4.10. There are nine distinct regions in the phantom, which are separately labelled. Three separate cases are studied.

1. The standard phantom
2. Phantom corrupted with complex additive Gaussian noise (SNR = 10 dB)
3. Phantom with a fine grid-structure super-imposed.

Table 4.1: Comparison of SSIM indices for distinct regions of the phantom, for image reconstructions obtained using CRAUNN, GRAPPA and SENSE

Region	CRAUNN	GRAPPA	SENSE
1	0.89	0.67	0.46
2	0.52	0.40	0.55
3	0.59	0.41	0.74
4	0.94	0.13	0.39
5	0.89	0.67	0.47
6	0.99	0.67	0.39
7	0.39	0.84	0.19
8	0.74	0.67	0.32
9	0.78	0.67	0.48

In all the 3 cases, the phantom is multiplied with the coil-sensitivity data (8-coil) available on [2], in order to simulate parallel MR data. The size of the image matrix is 256×256. The central 32 lines are densely sampled, while the remaining k-space is sparsely sampled, depending on the down-sampling factor. All the reconstructions are carried out for a downsampling factor of 4. The distinct structures in the reconstructed phantom in Fig. 4.10 are separately assessed. Table 4.1 lists the SSIM indices obtained for the reconstructions (case 1), using CRAUNN, as well as other existing techniques. The comparison of the SSIM indices for the noisy-phantom (case 2) is shown in Table 4.2. A grid of varying thickness and intensities, spread out, was superimposed on the phantom (case 3) to determine the abilities of the techniques to reproduce fine structures. A comparison of the reconstructions for case 3, obtained using CRAUNN, GRAPPA and SENSE is performed in Fig. 4.11 Table 4.4 lists the PSNR values achieved by the different techniques. It can be seen that PSNR values of the CRAUNN and GRAPPA reconstructions are comparable, while that of SENSE is lesser. However, when visually assessed, it can be seen that the image reconstructed by CRAUNN is perceptually better.

Table 4.2: Comparison of SSIM indices of distinct regions of the phantom, corrupted with noise, for image reconstructions obtained using CRAUNN, GRAPPA and SENSE

Region	CRAUNN	GRAPPA	SENSE
1	0.80	0.67	0.46
2	0.55	0.48	0.59
3	0.63	0.51	0.77
4	0.84	0.14	0.39
5	0.93	0.67	0.39
6	0.81	0.78	0.32
7	0.28	0.84	0.18
8	0.66	0.67	0.32
9	0.73	0.69	0.48

Table 4.3: Comparison of SSIM indices for distinct regions of the noisy phantom with super-imposed grid, for images reconstructed using CRAUNN, GRAPPA and SENSE

Region	CRAUNN	GRAPPA	SENSE
1	0.79	0.57	0.40
2	0.56	0.36	0.46
3	0.62	0.44	0.58
4	0.88	0.06	0.37
5	0.92	0.60	0.36
6	0.81	0.63	0.27
7	0.37	0.77	0.22
8	0.66	0.52	0.33
9	0.72	0.58	0.42

Table 4.4: Comparison of PSNR values of the images reconstructed by CRAUNN, GRAPPA and SENSE

Phantom	CRAUNN	GRAPPA	SENSE
Noise-less	26.6	27.3	14.8
Noisy	24.9	27.3	6.9
With Grid	25.2	25.1	15.3

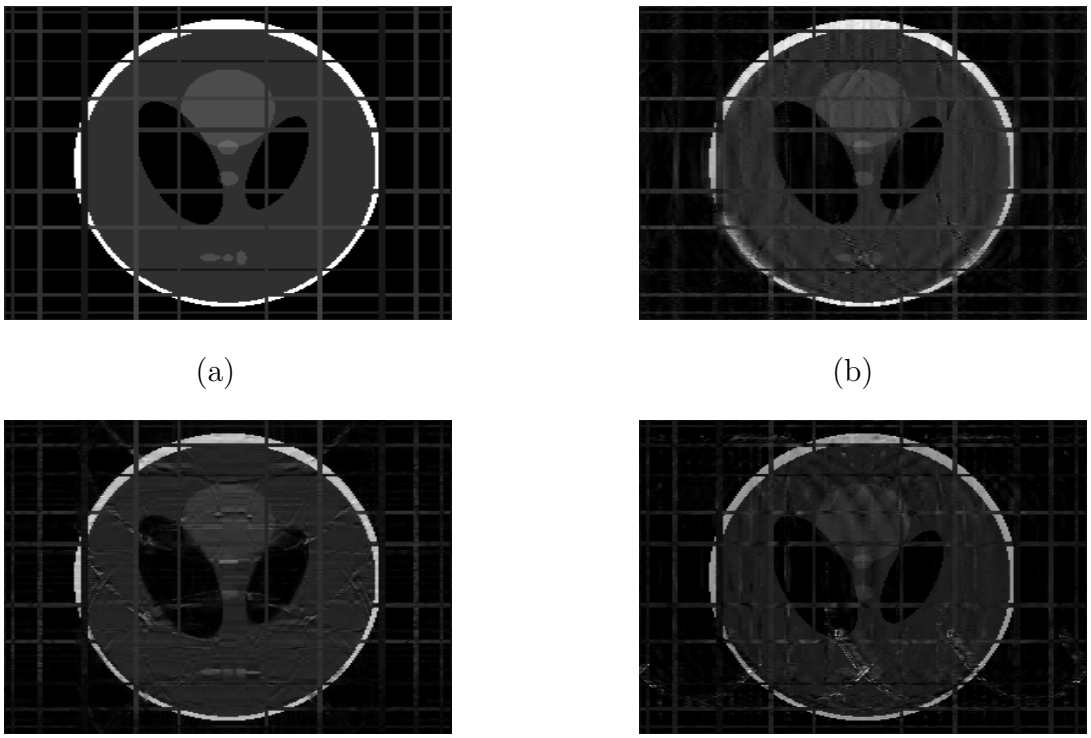

(a) (b)

(c) (d)

Figure 4.11: Comparison of performance of different techniques on the Shepp-Logan phantom super-imposed with a fine grid-like structure, for undersampling by a factor of 4. (a) Original image (b) Image reconstructed using CRAUNN (c) Image reconstructed using GRAPPA (d) Image reconstructed using SENSE [color scale: 0-255]

4.5.2 Real data

Structural brain data

The CRAUNN method is applied on real data sets of brain MR images. A real structural brain data set (8-coil data) available on [2], is utilized. The data matrix is of size 256 $\times$ 256. The central 32 lines are densely sampled, while the remaining k-space is sparsely sampled, depending on the down-sampling factor. Figure 4.13 displays the reconstructed and the corresponding error images, for a downsampling factor of 4, for the structural brain image shown in Fig. 4.12. The same sparsely sampled data is used for reconstruction by the standard parallel imaging techniques, SENSE and GRAPPA. Figure 4.13 clearly shows that the artifacts in error images from SENSE and GRAPPA reconstructions are

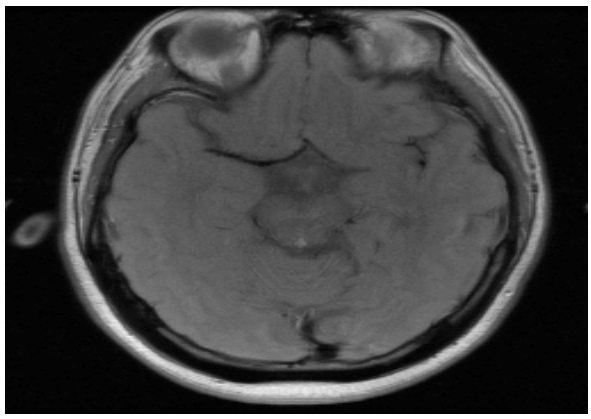

Figure 4.12: Real data : Original image of the structural brain data used for the study [0-255] (Source : [2])

greater than those obtained with the CRAUNN technique. CRAUNN achieves a gain in PSNR of 10 dB over SENSE. The PSNR values obtained using GRAPPA and the CRAUNN approach are almost comparable.

The performance of CRAUNN using a single neural network for the entire image, is compared with that using four identical neural networks for the image (one NN for each quarter of the image) in Figs. 4.14(a) and (b). It is observed that the performances are comparable, with no clear winner. When a single NN is used for the entire image, the number of input feature vectors is four times that in the approach where each NN is used only for a quarter of the image, making the former approach slower. Utilizing 4 NNs in place of 1 NN makes the process parallalizable and faster, but results in no improvement in the quality of reconstruction.

Functional brain (fMR) data

fMRI data is obtained for experiments with "visual stimulus". In the course of the experiment, 3 two-dimensional T_2^*-weighted images, each with 64 scans, are acquired using a gradient-echo FLASH sequence. The acquisition parameters are: TE/TR = 40 msec/80.5 msec, matrix size = 128×64; slice thickness = 5-mm and 2-mm gap. The image

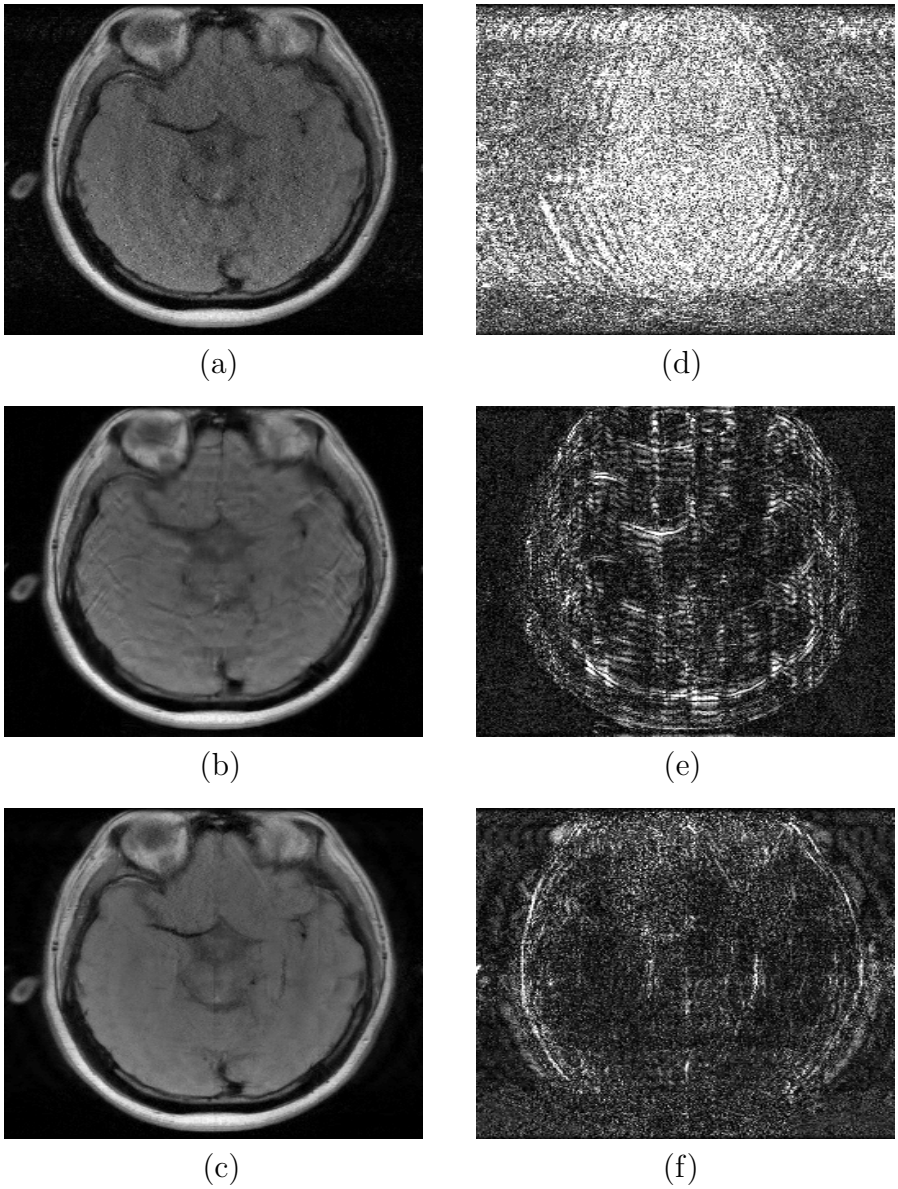

Figure 4.13: Comparison of performance of different techniques on a real brain data set for undersampling by 4. Left Panel : Reconstructed images using (a) SENSE (b) GRAPPA (c) CRAUNN (color scale : 0 to 255) Right Panel : Corresponding error images, for reconstructions using (d) SENSE (e) GRAPPA (f) CRAUNN (color scale : 0 to 34)

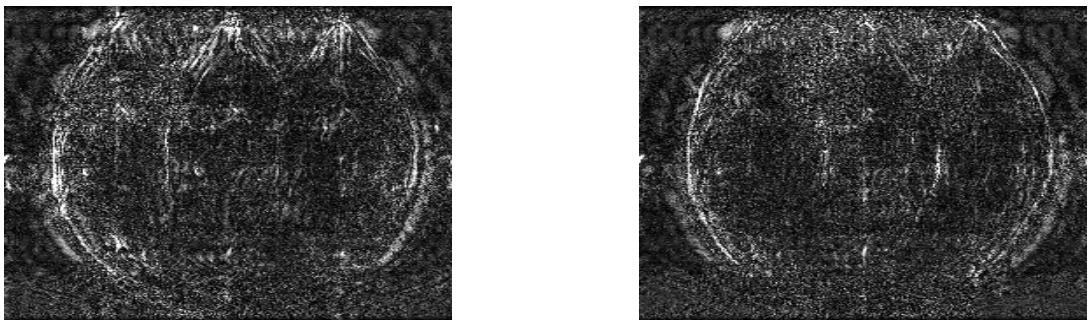

(a) (b)

Figure 4.14: Performance comparison of 1NN and 4NN models using error images : Error image obtained using (a) CRAUNN - 1 NN (b) CRAUNN - 4 NN model [color scale : 0 to 34]

matrices are zero-filled to obtain images of size = 128 × 128, with a spatial resolution of 1.953 × 1.953 mm; The corresponding two-dimensional anatomical slices are also acquired with a T_1-weighted IR RARE sequence (TI = 900 msec; TE/TR = 3900 msec/40 msec, matrix size = 512 × 512) in the same experimental session. In all the experiments, ON and OFF stimuli are presented at a rate of 5.162 sec/sample. Each stimulation period had four successive ON states followed by four OFF states. The stimulations are repeated for eight cycles, thus resulting in an acquisition time of 5.5 min. The experiments are carried out at different sessions with different subjects. The visual stimulation task comprised an 8-Hz alternating checkerboard pattern with a central fixation point projected on a LCD system. The subjects are asked to fixate on the point during the stimulation. Images are acquired at three axial levels of the brain at the visual cortex.

The error image for the splines-based reconstruction is compared with that of CRAUNN method in Fig. 4.15. The PSNR value obtained using the CRAUNN method is about 10 dB greater than that obtained with the splines-approach.

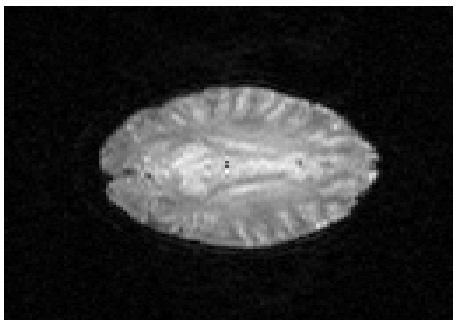

(a)

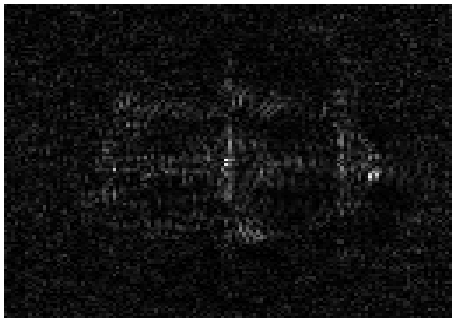

(b)

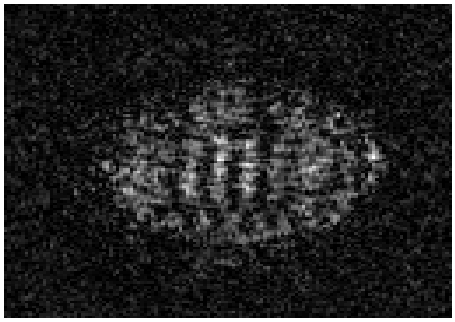

(c)

Figure 4.15: Performance comparison of CRAUNN and the splines-based methods on a real fMR data set using undersampling by a factor of 4. (a) Original image [0-255]. (b) Error image obtained using CRAUNN method [0-50]. (c) Error image obtained using splines method [0-100].

4.6 Discussion

The proposed method, CRAUNN, uses neural networks to determine the desired alias-free image. The transformation required to reconstruct the alias-free composite image is determined using images obtained with low frequency acquisitions. The idea of utilizing low-frequency acquisitions to determine the image reconstruction operator and then using it for acquisitions containing the entire range of k-space frequencies, is similar to the idea reported by Jan Petr et al., in [47]. However, the reconstruction method based on splines heavily relies on the localized nature of the PSF obtained using Cartesian undersampling and also on the assumption of linear form for the transformation function. The technique

reported in [47] determines the image reconstruction operator using a linear combination of B-splines. In both methods, the explicit evaluation of coil sensitivities is not required. However, Fig. 4.15 clearly illustrates that CRAUNN outperforms the splines method.

The CRAUNN method is compared with the standard methods and the performance is found to be superior on the real and synthetic data sets analysed. The function that processes the aliased coil images to yield the composite unaliased image, is estimated with no assumptions of form or complexity. The only underlying assumption is that the transformation that holds for images obtained using only low frequencies, should also hold for images obtained using the entire range of k-space frequencies.

Besides, the fact that the network is solely trained by the same image, leads to fewer artifacts than can occur if features from other images are learnt. The training phase needs about hundred iterations to converge to an error of $\frac{1}{100}^{th}$ of the maximum intensity of the original image.

The results on the standard "Shepp-Logan" phantom, corrupted with noise and super-imposed with a fine grid-like structure, show the superior performance of the CRAUNN approach. A close look at the distinct regions in the phantom labelled in Fig. 4.10 and the associated SSIM indices tabulated in Tables 4.1, 4.2 and 4.3, help us make some observations about the CRAUNN method in comparison with the existing methods. Across the three cases, it is noted that the CRAUNN method as well as GRAPPA outperform SENSE. It must be remarked that region number 7, which happens to be a tiny elliptical region sandwiched between two ellipses is the most challenging for the CRAUNN method as well as SENSE. It must be attributed to the fact that the two methods are image-domain based. GRAPPA, the k-space domain based method performs remarkably well in that region. The average SSIM for the noisy Shepp-Logan phantom using the proposed method is 0.68, while those obtained using GRAPPA and SENSE are 0.6 and 0.42, respectively. For the case of the phantom super-imposed with fine grid-like structure, the average SSIM index obtained with CRAUNN is 0.7, while those for GRAPPA and SENSE are 0.5 and 0.37, respectively. The PSNR values obtained (see Table 4.4) using the three methods show that the CRAUNN method and GRAPPA perform comparably, while the

performance of SENSE lags behind. GRAPPA is found to out-perform the other methods for the case of noisy phantom.

From the error images shown in Fig. 4.13, we observe that the reconstruction obtained using SENSE clearly preserves the structural details. However, the method loses out on account of allowing bright aliases. The replication of larger structures stands out in the reconstruction, as seen in the error image (Fig. 4.13(d)). GRAPPA performs comparably well with the CRAUNN technique, as seen in Figs. 4.13(b) and (c). Figures 4.14(a) and (b) illustrate that parallelizing the reconstruction does not lead to better results. The comparison of artifacts in the error images shown in Fig. 4.15, illustrates that the CRAUNN method outperforms the splines-based approach.

4.7 Conclusion

We have proposed a neural network framework to reconstruct images for parallel magnetic resonance imaging. Variable density data acquisition is carried out at all the receiver coils. Low k-space frequencies (32 central k-space lines) are densely sampled while the rest of the frequencies are sparsely sampled. The densely sampled central k-lines are used to obtain the blurred unaliased image. The same lines are undersampled to obtain the corresponding aliased coil images, which form the input training data set for the neural network. The corresponding target used in training phase is the blurred unaliased composite image. The weights needed to generate the unaliased composite image from the aliased coil images are determined.

The trained neural network is fed with images obtained using regularly undersampled full k-space data, in order to obtain the final image reconstruction. Thus, we do not assume any specific form for the function that combines the aliased coil images. The CRAUNN technique is applied on phantom and real MR data sets. "Shepp-Logan" phantom corrupted with complex Gaussian noise, and super-imposed with a fine grid-like structure is used to verify the credibility of the technique. Besides, the technique is applied to real MR data sets of the brain (both structural and functional). The results are compared with those generated by the techniques like SENSE and GRAPPA. Performance is evaluated using criteria like PSNR and structural similarity index.

4.8 Acknowledgements

We thank Jan Petr for giving us the result on the fMR images, reconstructed using splines method.

We acknowledge Swati Rane and Jim Ji of Texas A&M University for putting up valuable resources on the website [2]. We have utilized the structural brain data and codes for SENSE and GRAPPA from these resources.

We also acknowledge Wang and Bovik of Texas Austin University for making their

papers and codes available on the website [4]. We have utilized their SSIM code.

Chapter 5

CRAUNN for non-Cartesian parallel MR imaging

Abstract

In rapid parallel MR imaging with non-Cartesian trajectories like spiral and radial, the problem of image reconstruction is challenging since undersampling along non-Cartesian trajectories results in aliasing which is not straight-forward to unalias. Here we propose image reconstruction for data sampled along general non-Cartesian trajectories, utilizing the neural network framework, called "Composite Reconstruction And Unaliasing using Neural Networks" (CRAUNN), as discussed in the preceding chapter. Radial and spiral trajectories on real and synthetic data, are utilized. The reconstruction errors depend on the acceleration factor as well as the sampling trajectory. It is found that higher acceleration factors can be obtained when radial trajectories are used. Comparisons against the existing techniques are presented, and the proposed method has been found to result in better-quality images compared to the existing techniques.

5.1 Non-Cartesian sampling trajectories

The simplest sampling trajectory is Cartesian, that leads to image reconstruction using the well-known 2D FFT of the sampled points. However, this trajectory is not preferred

in certain applications for its disadvantages such as sensitivity to motion/flow artifacts and no choice in sampling density along the read-out direction. These disadvantages are overcome by non-Cartesian trajectories like radial and spiral. Image reconstruction with sparse non-Cartesian sampling has been the subject of study by the MR research community [61, 69, 36].

5.1.1 Radial scan

This trajectory is shown in Fig. 5.1(a) and consists of a collection of spokes that are the radii of an imaginary circle in k-space. The PSF obtained for undersampled radial scans, shown in Fig. 5.2(a) illustrates that the center of the image remains alias-free. Hence high under-sampling factors can be achieved since the aliasing artifacts appear as radial streaks away from the center of the image. The disadvantage faced with this trajectory is that during actual acquisitions, the various radial lines may not intersect exactly at the origin of the k-space leading to artifacts like blurring and ghosting.

5.1.2 Spiral scan

Spiral trajectory is shown in Fig. 5.1(b), and in this acquisition the points are sampled along a spiral centered at the origin of the k-space. Most of the spiral imaging sequences realize Archimedean spirals given by $k(t) = A\theta(t)\exp^{j\theta(t)}$, where $\theta(t)$ represents a monotonically increasing function and $k(t) = k_x(t) + jk_y(t)$. The distance between two successive revolutions has to be smaller than $1/FOV$ to avoid aliasing. Archimedean spirals have the property of constant distance between two successive arms, which helps in designing the optimal spiral trajectory for a given value of FOV. The function $\theta(t)$ determines the spacing between the samples along the spiral. The choice of $\theta(t)$ is critical since care must be taken to ensure that the gradient waveforms comply with hardware limitations such as gradient amplitude and slew rate. The optimal choice of function has been shown to be $\theta(t) = \frac{t}{\sqrt{(\alpha+(1-\alpha)t)}}$ [6, 10], where α is used to tune the spiral between constant angular speed and constant orbit speed. The PSF obtained for undersampled

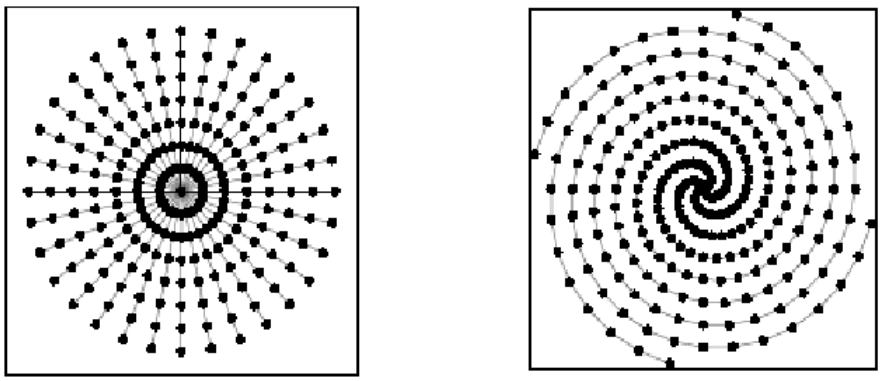

(a) (b)

Figure 5.1: Non-Cartesian trajectories considered here : (a) Radial (b) Spiral

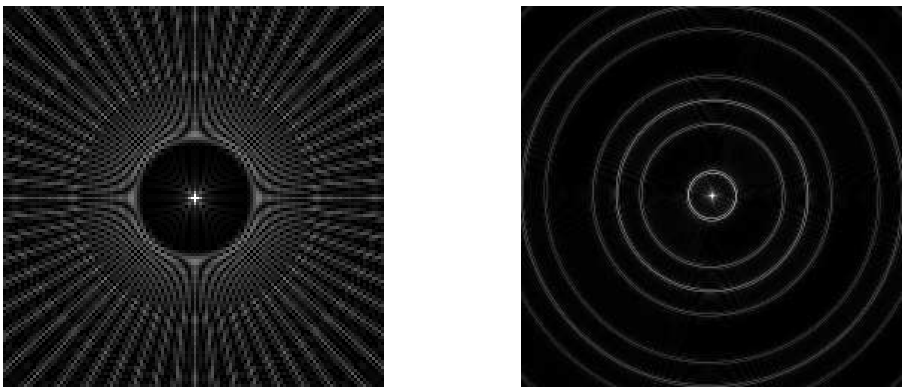

(a) (b)

Figure 5.2: Point Spread Function (PSF) obtained on undersampling : (a) Radial trajectory. (b) Spiral trajectory.

spiral scans is shown in Fig. 5.2(b). The disadvantage of using spiral scan is that it is too sensitive to hardware imperfections. Besides, off-resonance effects, which occur due to signal contributions with resonant frequencies other than the central water proton resonance frequency, lead to blurring.

Apart from these, rosette sampling [45] is also used in fMR imaging for higher temporal resolution especially in applications where data points are acquired from multiple slices simultaneously. It is also found useful in NMR applications such as resolving different spectral components corresponding to various chemicals. Random trajectories have also

been utilized in order to overcome problems caused by coherent accumulation of signal for off-resonance spins.

5.2 Image reconstruction with fully sampled data

This section deals with image reconstruction using data sampled along non-Cartesian trajectories. The issues discussed here are purely those that arise from the non-Cartesian nature of the sampling trajectory. The sampled points need to be "regridded" along Cartesian grids in order to use FFT for image reconstruction since the data lie on an arbitrary sampling grid that is not amenable to FFT. The problem is further complicated because the density of the samples is not uniform all along the k-space. The data acquisition needs to satisfy Nyquist requirements at every location. The higher density of samples in the low k-space needs to be compensated for. This process is called "density compensation". Besides, the non-rectangular region of support of the sampled k-space leads to abrupt truncations at the edges, and needs to be corrected. This process is called "apodization".

5.2.1 Regridding

Regridding of non-Cartesian data to Cartesian grids requires reliable interpolation tools. The choice of the convolution kernel must be made very carefully. Kernels like sinc, Gaussian and their variants have been experimented with. A technique called "Block Uniform ReSampling" (BURS) [14] has been reported, which utilizes the interpolation matrix derived from the trajectory and grid positions using the sinc function. The pseudo inverse of the interpolation matrix multiplied with the given k-space data at arbitrary locations results in the Cartesian regridding of the given data. Jackson et al. [25] proposed a Kaiser-Bessel convolution window for regridding, which has been shown to be optimal in minimizing aliasing as well as leakage.

5.2.2 Density compensation

In order to compensate for variable sampling density, it is required that the data samples be weighted by a suitable density compensation function [20]. One of the prevalent methods utilizes Vornoi diagram [55] for determining the neighborhood associated with each sampled point. Jackson [25] has proposed the convolution of the sampling grid with the Kaiser-Bessel function. Pipe [49] proposed an iterative method to compute the density compensation function, initializing with the function proposed by Jackson. However, research is still on to determine the best possible method for density compensation to get rid of blurring due to over-sampling of low k-space.

5.2.3 Apodization

This is carried out to get rid of the Gibbs ringing that manifests in the reconstructed images due to the abrupt truncations at the boundaries of the non-rectangular region of support of the sampled k-space. The k-space samples are multiplied by a suitable filter so that the transition at the edges of the region of support is smooth. This process however introduces blurring. The user needs to trade-off spatial resolution against truncation artifacts.

5.3 Reconstruction with undersampled acquisitions

This section deals with the image reconstruction schemes that have been in existence, for data sampled along non-Cartesian trajectories, below Nyquist density requirements. Apart from the issues mentioned in the preceding section, the additional issue that needs to be addressed in such acquisitions is that of aliasing. It is well-known that the aliasing arising out of undersampling data along non-Cartesian trajectories is hard to characterize and cannot be put into a closed mathematical expression. Unlike Cartesian regular undersampling, the aliasing pattern is not a simple replication. Also the varying density of samples across the k-space needs to be addressed. As shall be seen in the section ahead,

most of the existing methods can be described as attempts to adapt the existing solutions for Cartesian trajectories to suit non-Cartesian trajectories.

The linear-algebra framework used in [51] was extended to non-Cartesian trajectories by proposing an iterative solution using conjugate-gradient method "CGSENSE" [50]. Although this solution is widely used, it faces the problem of regularization in the event of poor SNR, leading to numerical instabilities. Many regularization techniques have been reported [28] to counter the problem of numerical instability, the most popular of them being Tikhonov regularization scheme [41]. Another strategy for image reconstruction, called POCSENSE has been proposed [60], in the framework of "Projection On Convex Sets" (POCS). The advantage of this method lies in its capability to incorporate prior knowledge into the solution. This solution is also iterative, and unlike CGSENSE, poses the problem in a set-theoretic rather than linear-algebraic framework, making it possible to incorporate non-linear constraints. Both of the above-mentioned methods faced the drawback of needing a separate scan for estimating the coil sensitivities. This drawback was overcome in many later reported works that over-sampled the low k-space, to obtain alias-free low-frequency images. The densely sampled low k-space was used to estimate the coil sensitivities, thus eliminating the need for a separate calibration scan.

Hybrid methods such as "Sensitivity Profiles from an Array of Coils for Encoding and Reconstruction In Parallel" (SPACE-RIP) [34] that work both in image and k-space domains have also been explored. This method too requires estimation of coil sensitivities, which are used to partially encode the image. Reduced acquisition of k-space is carried out and is shown to be adequate enough for image reconstruction.

In works such as [74, 52], the observation that trajectories such as radial/spiral inherently over-sampled the k-space center was exploited. They reported attempts to estimate coil sensitivities, without modifying the sampling trajectories. They utilized acquisitions within a certain region, where the sampling density would be sufficient enough to satisfy Nyquist requirements. However, the question remained on the optimality of the choice of the cut-off k-radius, within which the samples could be assumed to be free of aliasing

artifacts. In [52], the authors obtain the optimal radius for determining the coil sensitivities by examining the PSF visually. They declare that radius to be optimal where the trade-off between blurring and aliasing artifacts is "well-balanced". However, the method only depends on visual inspection and could be subjective. In [74], the cut-off k-space radius is determined by comparison with Nyquist density. The k-space radius, within which the samples are acquired beyond the critical requirement of Nyquist density, is chosen as the cut-off. Samples well within this radius are used to determine coil sensitivities. However, this work acknowledges the fact that for greater acceleration factors (beyond 4), one might have to modify trajectories.

In most of the k-space based techniques, a combination of the acquired points in the vicinity of a missing sample is used to estimate the unknown value. The techniques mainly differ in the method adopted to generate the combining coefficients. The well-known technique "GeneRalized Auto-calibrating Partially Parallel Acquisitions" (GRAPPA) [12], first proposed for uniformly-spaced acquisitions along Cartesian trajectories, was adapted to suit non-Cartesian trajectories. Extension to radial sampling was proposed by laying out the acquired radial data along a pseudo-Cartesian plane [11]. The same idea was adapted for spiral acquisitions too [16]. However, the drawback of this procedure was that it required a complete separate scan to determine the combining weights. This drawback was overcome in works that reported determination of the combining weights using densely sampled low k-space [17] with dual-density spirals. In [18], interpolation kernels are separately generated for each sector that the k-space is divided into. Numerous variations of GRAPPA like PARS [75] and "Direct SENSE" [63] differ in the criterion for the selection of the best neighbourhood. In methods like "Parallel image reconstruction Based On Successive Convolution Operations" (BOSCO) [22], convolution kernels are devised using low k-space, which are then used to generate the missing points in the high k-space. In k-space based techniques, the estimation of coil sensitivities is not very critical, and also they have the advantage that the processing takes place in the same domain as that of data acquisition. However, these methods are computationally more intensive than image-domain methods.

In our work, we employ CRAUNN in the context of non-Cartesian parallel imaging. The proposed technique has been applied to radial and spiral acquisitions of real and synthetic data. Acceleration factors of up to 6 and 4, have been achieved in radial and spiral cases, respectively.

5.4 Proposed method: CRAUNN

5.4.1 PSF observations

The proposed method is based on the observation that for a fixed undersampling factor the nature of the PSF (ie, aliasing) remains the same, irrespective of whether the acquisition contains only low frequencies or entire range of frequencies. It is well-known in the case of Cartesian sampling, that for a fixed undersampling factor the PSF obtained for a low-frequency acquisition contains localized peaks at precisely the same points as the PSF for an acquisition containing both low and high frequencies. In the case of low-frequency acquisition, the peaks get smeared, indicating blurring. The same observations can be made in the spiral and radial cases too, from Figs. 5.3(a-d), which depict the magnitude functions of PSFs for spiral and radial acquisitions for the undersampling factor of 2. Aliases are contributed in proportion to the brightness of the regions seen in the PSFs. Here, the PSFs are not localized unlike the Cartesian case and hence unaliasing is not straightforward. In the spiral case, accelerated scans utilize lesser number of spiral interleaves. As the spacing between two consecutive interleaves increases, the concentric circles seen in the PSF get closer leading to greater aliasing. With radial trajectory, accelerated scans mean utilization of lesser number of radial projections. As the spacing between two consecutive radial projections increases, the streaking artifacts increase. Radial PSF offers an inherent advantage over spiral PSF since the aliasing artifacts occur away from the center.

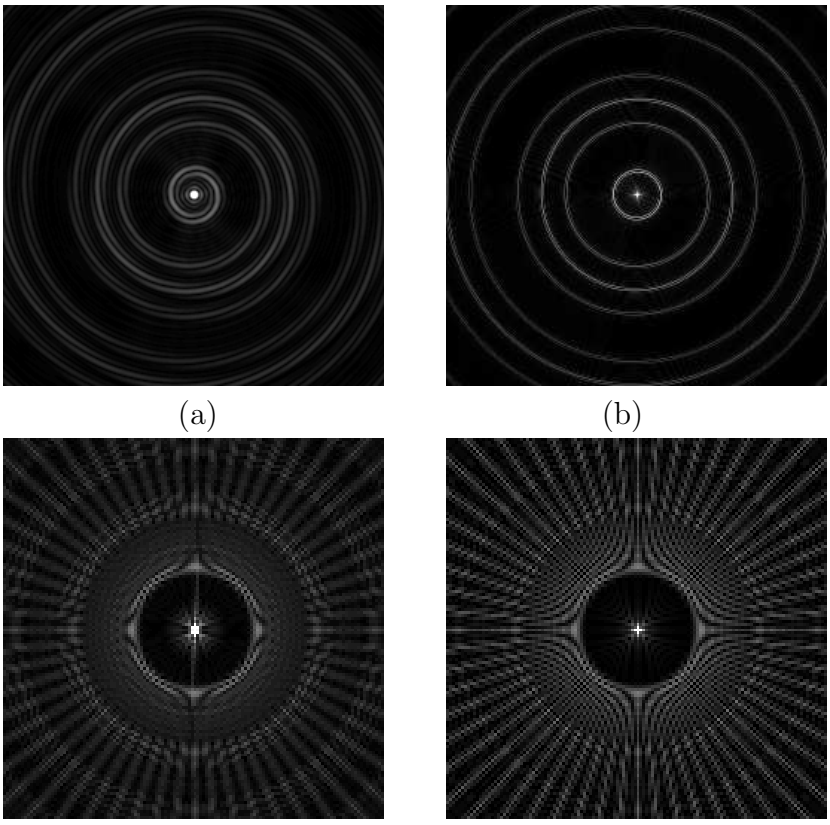

Figure 5.3: Illustration that the nature of aliasing does not depend on the extent of frequency content in the acquisition. PSF obtained on undersampling spiral trajectory for acquisitions containing : (a) Low frequencies only. (b) Both low and high frequencies. PSF obtained on undersampling radial trajectory for acquisitions containing : (c) Low frequencies only. (d) Both low and high frequencies.

5.4.2 Neural network-based reconstruction

As discussed in the previous chapter, in the proposed CRAUNN approach, the image reconstruction operator is assumed to be a function of the aliased coil images, processed pixel-wise. The reconstruction function, $\mathcal{F}$, to estimate the composite alias-free image $\hat{S}$, using the L aliased coil images, (S_l^A) is given as:

$$\hat{S}(x,y) = \mathcal{F}\left(S_l^A(x,y)\right) \quad \text{where } l = 1, 2, \cdots, L \tag{5.1}$$

The function is allowed to be arbitrary in form and complexity, and is determined using neural networks. Thus, both the unaliasing and combining of coil images to generate the composite image are accomplished together by the neural network, without explicitly estimating the coil sensitivity.

In the training phase, the system takes the aliased coil images as input, and learns the transformation required to output the corresponding true alias-free image. In this phase, only the low k-space data is used. At the end of this phase, the interconnecting weights among the nodes in the various layers are frozen, and the system is said to be configured for the image reconstruction.

In the reconstruction phase, the transformation learnt in the training phase is used. Here, the images are constructed using both low and high frequencies, uniformly under-sampled. Aliased coil images are input to the configured system. The output of the system is the estimate of the desired alias-free image.

5.4.3 Images for learning and reconstruction

Alias-free images containing only low frequencies

It is well-known that alias-free acquisitions can be obtained by considering k-samples within low k-space where the sampling density satisfies Nyquist requirements. While Cartesian sampling schemes are modified to variable-density trajectories, non-Cartesian sampling trajectories may not need to be modified since they inherently over-sample low k-space. In the case of spiral sampling, variable density spirals are used, such that a central disk of radius $\frac{k_{max}}{10}$ is densely sampled. This densely sampled disk is used to obtain alias-free acquisitions. However, in radial sampling, variable density sampling is not possible. Hence a separate alias-free low-frequency acquisition scan is required in order to obtain blurred alias-free coil images. The alias-free coil images are combined to obtain the composite alias-free blurred version of the true image. Here, the composite image is taken as the root-sum-of-squares combination.

Aliased coil images containing only low frequencies

During training, the aliased coil images containing only low frequencies form the input to the system, while the corresponding alias-free image obtained as explained in the previous section forms the target of the system. We choose to retain only those low k-space samples that affect under-sampling by the desired acceleration factor, thereby generating aliased coil images with low frequencies alone. Now we have at hand, aliased coil images and the corresponding true image containing the same set of low k-space frequencies, which is what we require in the training phase.

Aliased coil images containing both low and high frequencies

The aliased coil images containing both low and high frequencies are obtained by uniformly undersampling the k-space. The appropriate samples from the densely sampled low k-space are ignored in order to affect aliasing by the required acceleration factor. Features from these aliased coil images are used as inputs to the configured neural network in the reconstruction phase. The output of the neural network is the estimate of the corresponding alias-free image.

5.5 Results

All simulations are carried out in MATLAB. CRAUNN is applied to spiral and radial acquisitions. For all the image reconstructions, regridding on a 2X grid is performed as in [25] using a Kaiser-Bessel window of width 2.5. Errors in image reconstruction are quantified using error images as well as by comparing scan lines that run through the images. Besides, a full-reference image metric called 'Structural SIMilarity' (SSIM) index [76] is used to assess the quality of reconstruction, as in the preceding chapter. The scale of the SSIM indices range from 0 to 1, where 0 implies very poor similarity to the original image, while 1 implies the best similarity to the original image. SSIM is widely used by the image/video processing community in order to evaluate degradations in image/video

reconstruction, based on structural similarities with the original. This is similar to the evaluation criterion utilized in [59], where human visual system is considered in order to determine the quality of the MR images.

5.5.1 Spiral case

Phantom data is obtained using a 8-channel head coil and a gradient echo spiral pulse sequence (16 interleaves, 3096 samples per interleaf) on a GE 1.5T Excite scanner. The spiral trajectory desired is such that the lower k-space up to $\frac{k_{max}}{10}$ is densely sampled, while among higher frequencies fewer interleaves are used. After density compensation and regridding, all reconstructed images were cropped to a 256×256 grid. For accelerated scans, the relevant spiral interleaves are set to zero. The well-known CGSENSE is also used to reconstruct the same data. The obtained reconstruction and error images for both the methods are shown in Fig. 5.4. CRAUNN is also applied on brain data available on [2], shown in Fig. 5.5. This is spirally re-sampled using 24 interleaves, with 4015 points in each interleaf. After density compensation and regridding, all reconstructed images are cropped to a 256×256 grid. For comparison, reconstruction with undersampled data (x4) is obtained using both CRAUNN and CGSENSE methods and are shown in Fig. 5.6.

A standard phantom used in non-Cartesian MR studies is also employed to assess the performance of the CRAUNN method. The reconstruction parameters remained the same as in the preceding data set. The results obtained and the comparison with the performance of CGSENSE are shown in Fig. 5.7. The performance metrics used, namely SSIM and RMSE, are tabulated in Table 5.1.

5.5.2 Radial case

For the radial case, a synthetic phantom is created (180 projections, 128 points). The phantom is multiplied with the 8-coil complex sensitivity data available on [2], and transformed to k-space in order to simulate 8-channel parallel MR data. Complex noise is added to the obtained k-space in order to simulate conditions of real acquisition to result

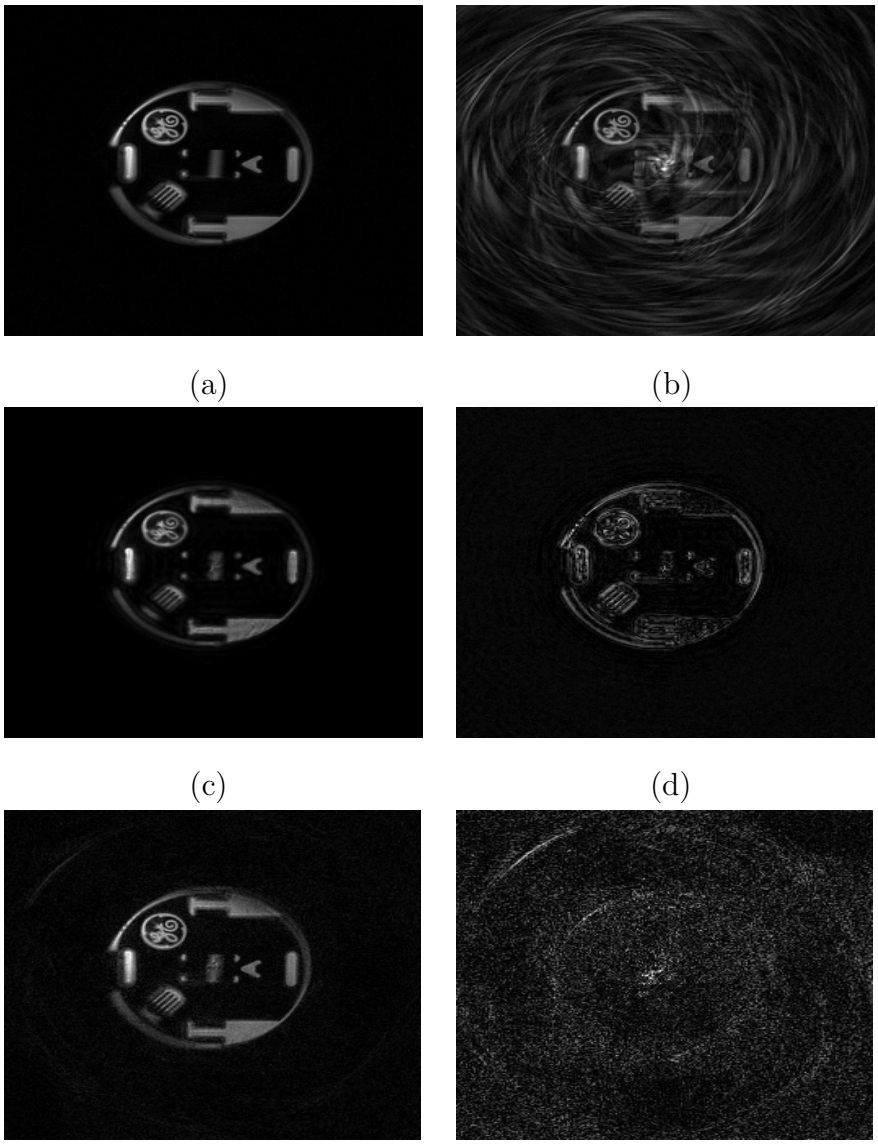

(a) (b)

(c) (d)

(e) (f)

Figure 5.4: Performance comparison on a real phantom data set for spiral undersampling by 4. (a) True image (16 spirals) [0-255]. (b) Direct reconstruction of undersampled data [0-255]. (c) Reconstruction with CRAUNN [0-255]. (d) Corresponding error image [0-60]. (e) Reconstruction using CGSENSE [0-255]. (f) Corresponding error image [0-51].

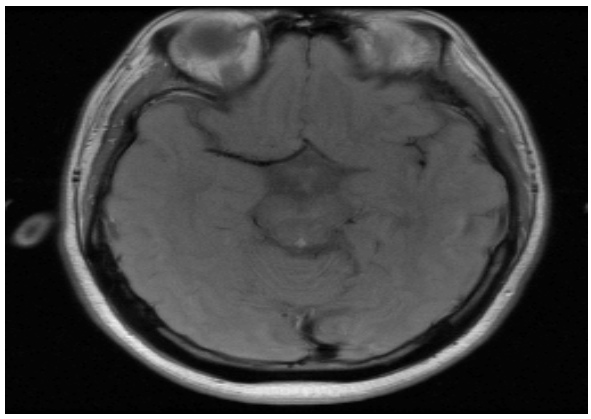

Figure 5.5: Real data : Original image of the brain data used for the study. (Source : [2])

Table 5.1: Performance comparison of CGSENSE and CRAUNN on spirally-sampled images.

	SSIM index		RMS error	
Spirally undersampled Image	CRAUNN	CGSENSE	CRAUNN	CGSENSE
GE phantom (Fig. 5.4(a))	0.81	0.76	6.1	8.1
Brain (Fig. 5.5)	0.85	0.52	12.3	21.7
Spiral phantom (Fig. 5.7(a))	0.82	0.74	14.9	18.1

in SNR of 10 dB. Unlike the previous cases, a pilot scan with unaccelerated acquisition within a certain k-space radius is required. For the simulations carried out, it is assumed that all the samples along all the projections till the frequency $\frac{k_{max}}{10}$ are available. These low frequency acquisitions are used to train the neural network. For the actual reconstruction, undersampling is achieved by discarding projections suitably, determined by the undersampling factor. After density compensation and regridding, all the reconstructed images are cropped to a 128 $\times$ 128 grid. The reconstructed images obtained using both CRAUNN and CGSENSE are shown in Fig. 5.8, along with the error images.

Besides, real brain data (8-channel) found on the web-site [2] (shown in Fig. 5.5) is used, by radially re-sampling (180 projections, 385 points) in k-space. After density compensation and regridding, all the reconstructed images are cropped to a 256 $\times$ 256

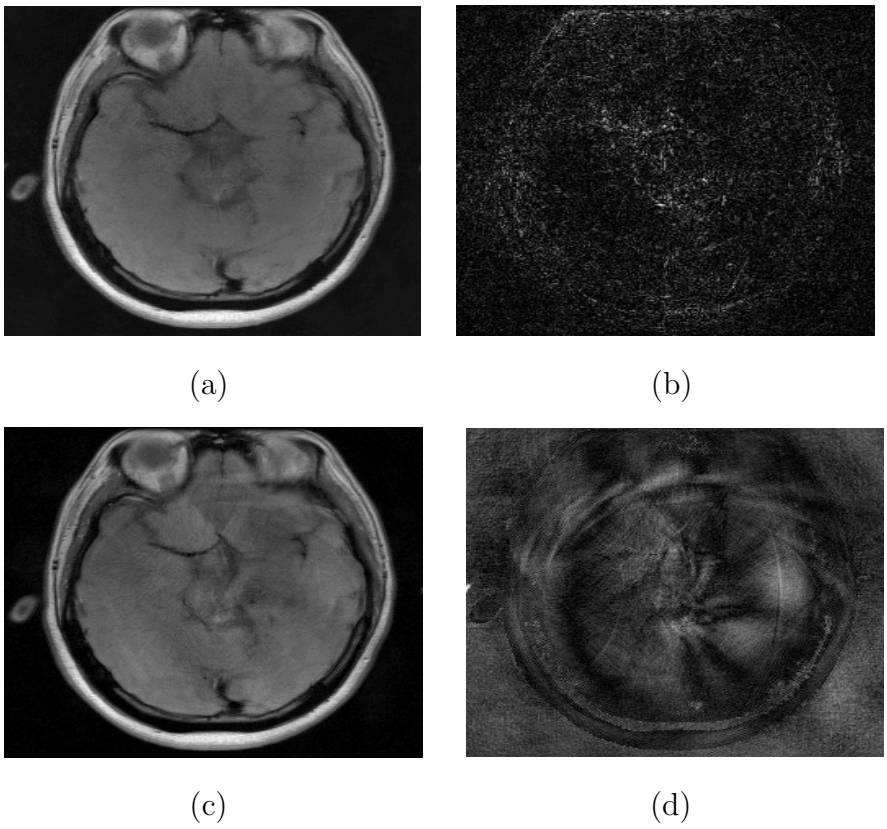

(a) (b)

(c) (d)

Figure 5.6: Performance comparison of CRAUNN with CGSENSE on real brain data shown in Fig. 5.5 for spiral undersampling by 4. (a) Reconstruction with CRAUNN [0-255]. (b) Corresponding error image [0-25.5]. (c) Reconstruction using CGSENSE [0-255]. (d) Corresponding error image [0-46].

grid. For comparison, reconstruction using undersampled data (x6) is performed using both CRAUNN and CGSENSE. The reconstructions obtained are shown in Fig. 5.9. The performance metrics evaluated, namely, SSIM and RMSE are tabulated in Table 5.2.

5.6 Discussion

The proposed method makes no assumptions about the nature of the sampling trajectory and hence can be generalized to any arbitrary trajectory. Also, the function that processes the aliased coil images to yield the alias-free true image, is estimated with no assumptions of form or complexity. The only underlying assumption is that the transformation that holds for acquisitions containing low frequencies alone also hold good for acquisitions that

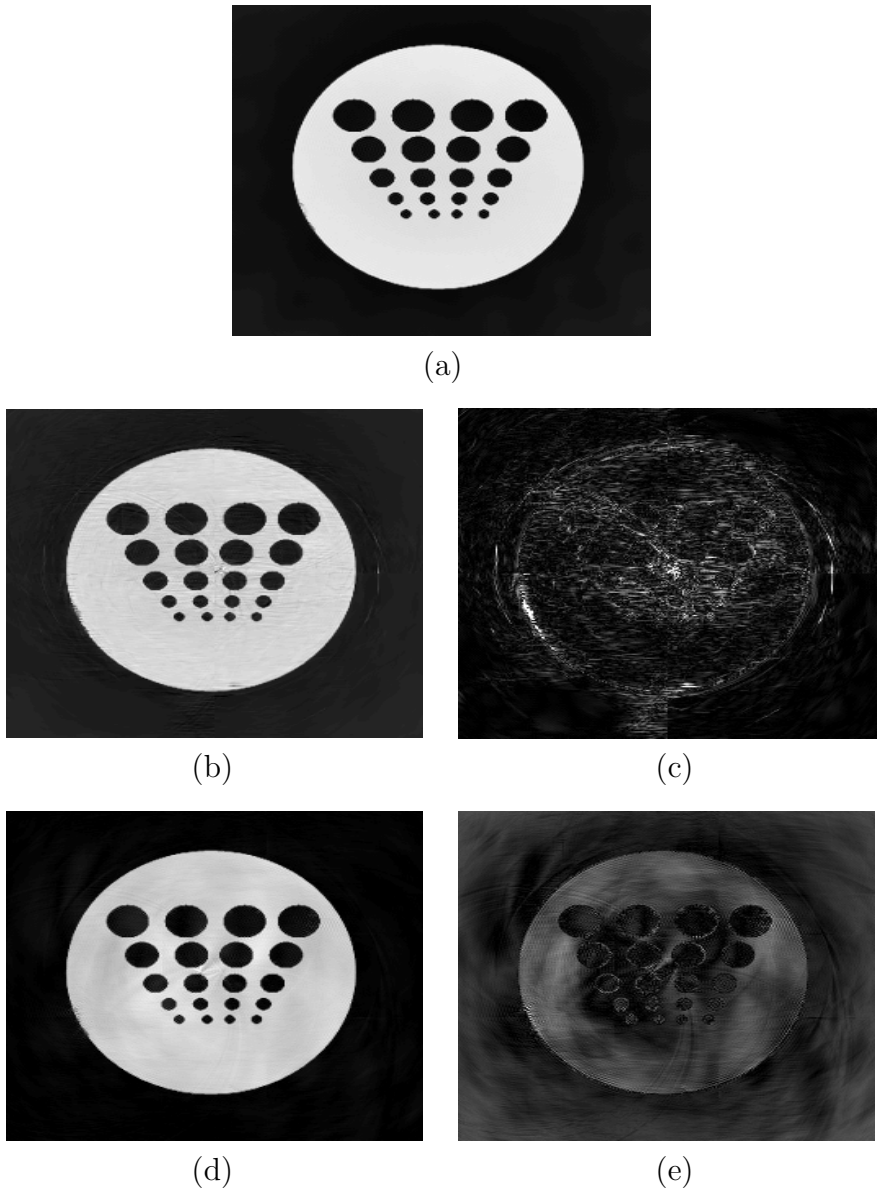

(a) (b) (c) (d) (e)

Figure 5.7: Performance comparison of CRAUNN and CGSENSE on a simulated data set for spiral undersampling by 4. (a) Original image [0-255]. (b) Image reconstructed by CRAUNN [0-255]. (c) Corresponding error image [0-92]. (d) Reconstruction using CGSENSE [0-255]. (e) Corresponding error image [0-92].

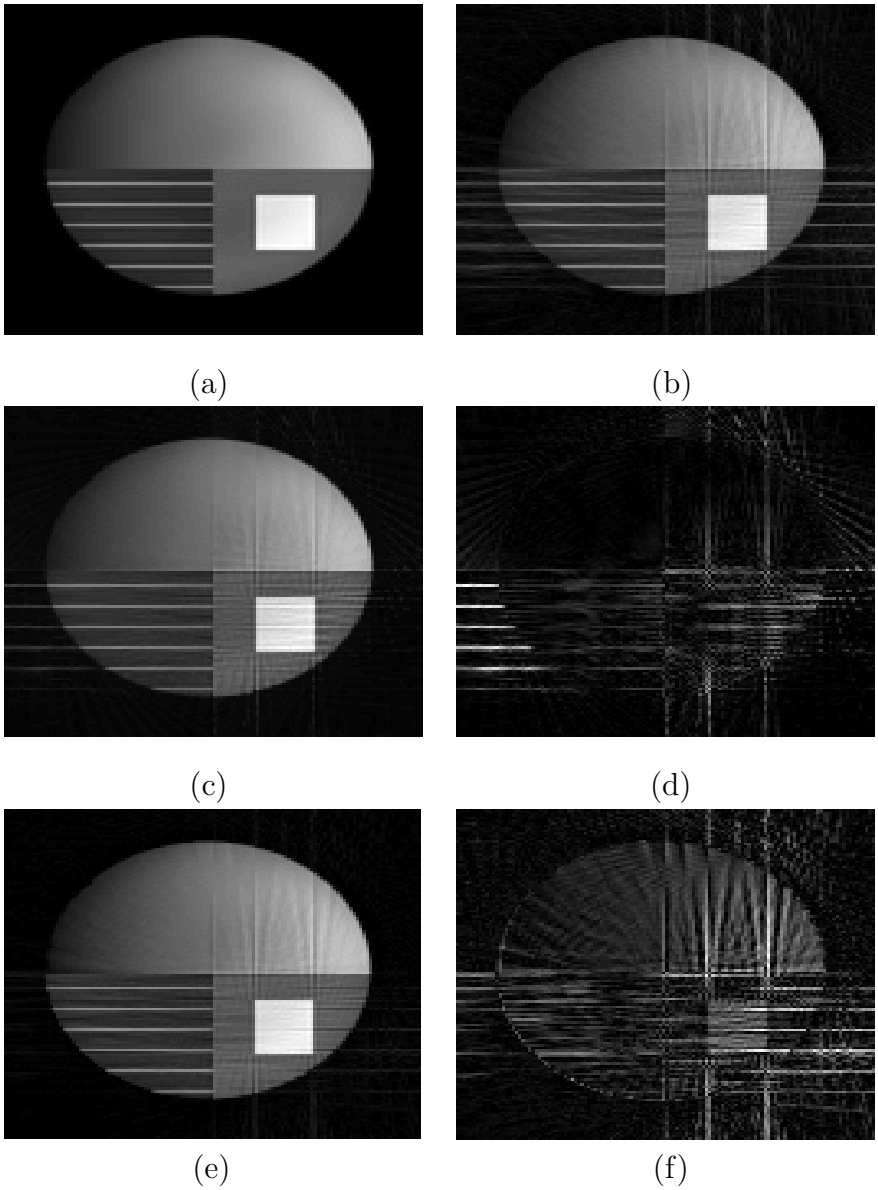

Figure 5.8: Comparison of performance of CRAUNN with CGSENSE on a simulated phantom using radial undersampling by 6. (a) Simulated phantom reconstructed using 180 radials [0-255]. (b) Direct reconstruction using data undersampled by 6 [0-255]. (c) Image reconstructed with CRAUNN [0-255]. (d) Corresponding error image [0-50]. (e) Image reconstructed using CGSENSE [0-255]. (f) Corresponding error image [0-55].

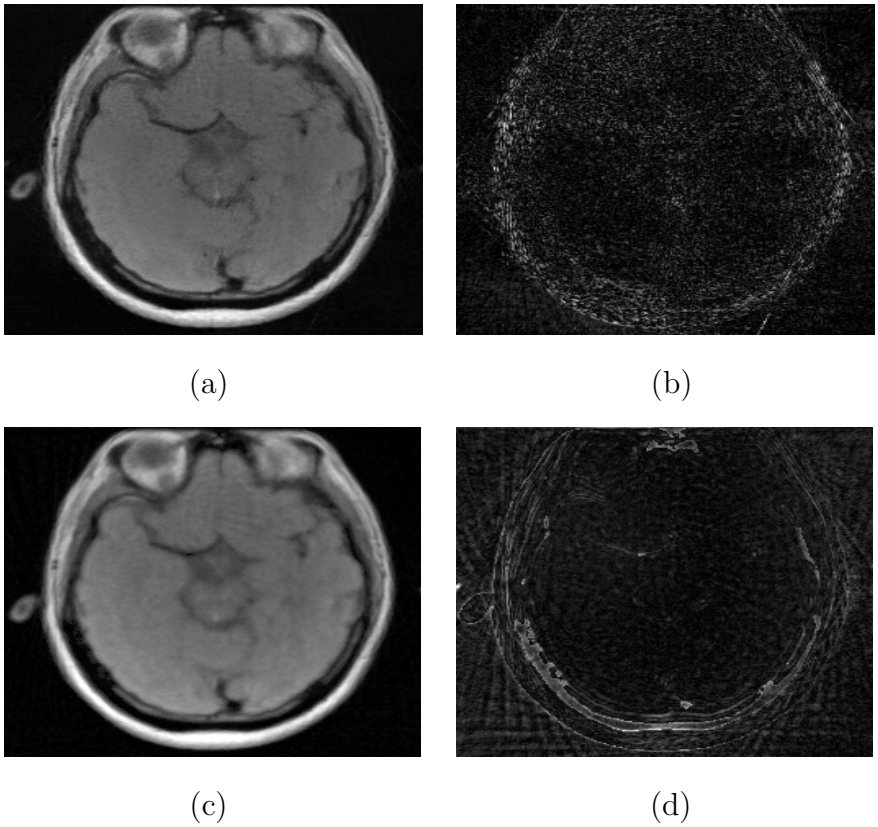

(a) (b)

(c) (d)

Figure 5.9: Performance comparison of CRAUNN versus CGSENSE on brain data shown in Fig. 5.5 using radial undersampling by 6. (a) Image reconstructed using CRAUNN [0-255]. (b) Corresponding error image [0-38]. (c) Image reconstructed using CGSENSE [0-255]. (d) Corresponding error image [0-46].

contain the entire range of frequencies, as seen from the observations made using the PSF images. The fact that the network is solely trained by the same image, leads to fewer artifacts than could have occurred if features from other images were also learnt. Here the explicit evaluation of coil sensitivities is not required, which is a great advantage, compared to existing methods like CGSENSE.

Since spiral and radial trajectories inherently over-sample the central k-space, the direct reconstruction without any intermediate processing of the sparsely acquired data also preserves the broader details of the image. However, the differences in reconstruction appear more prominently in the finer details. Comparison of the profile lines for the reconstructed images are shown in Fig. 5.10. Fine image details are zoomed into, and

Table 5.2: Comparison of performance of CGSENSE and CRAUNN, on radially-sampled images

	SSIM index		RMS error	
Image	CRAUNN	CGSENSE	CRAUNN	CGSENSE
Brain (Fig. 5.5)	0.83	0.72	6.1	9.5
Radial phantom (Fig. 5.8)	0.92	0.66	6.1	8.8

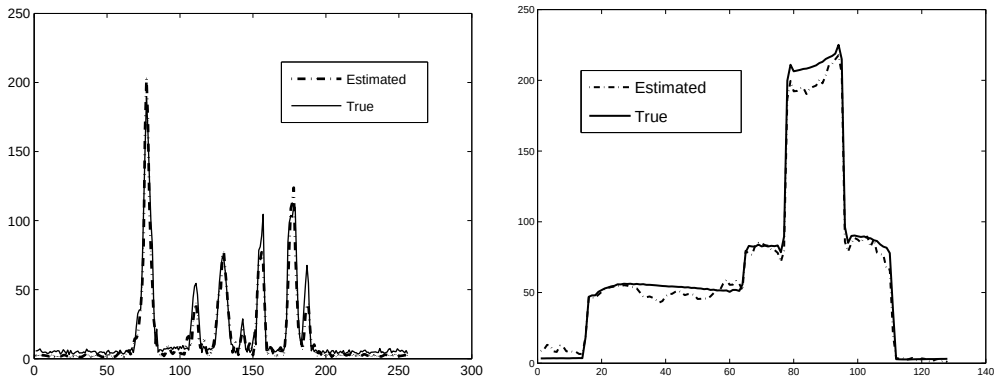

(a) (b)

Figure 5.10: Evaluation of the effectiveness of CRAUNN by comparison of scan lines through the original and the reconstructed images. (a)Spiral sampling (undersampled by 4) for the data used in Fig. 5.4. (b) Radial sampling (undersampled by 6) for the data used in Fig. 5.8.

compared in Figs. 5.11 and 5.12.

In the results obtained for the spirally re-sampled brain image, we compare the reconstructions obtained using the proposed method and CGSENSE. The error images clearly show the residual aliasing in the image obtained using CGSENSE, which is not seen in the image obtained by CRAUNN. In the case of radial sampling, greater acceleration factors are possible since the nature of aliasing leads to artifacts away from the center of the FOV. Most of the artifacts encountered here are mainly the streaking artifacts towards the image corners.

The SSIM indices for the phantom image reconstructed using CGSENSE and CRAUNN are compared in Fig. 5.13. It can be seen that the proposed method results in greater similarity to the reference image, as the SSIM indices show greater brightness than the

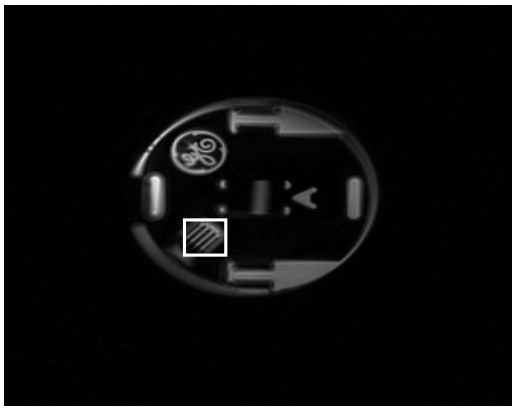

(a)

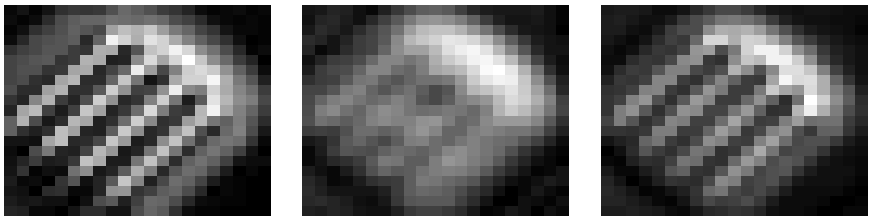

(b) (c) (d)

Figure 5.11: Comparison of details in the reconstructed images using the data shown in Fig. 5.4. (a) Original phantom image. The detail being observed is a comb-like structure marked by a rectangle (spiral data used is undersampled by 4). (b) Comb in the original image. (c) Comb in the direct reconstruction. (d) Comb in the reconstruction using CRAUNN.

one obtained using CGSENSE.

The average SSIM index for reconstructions using CRAUNN with spirally and radially undersampled data, are comparable at 0.83 and 0.87, respectively. The same measure for reconstructions using CGSENSE are 0.67 and 0.69, respectively. The average RMSE for reconstructions using CRAUNN with spirally and radially undersampled data, are 11.1 and 6.1, respectively. The same measure for reconstructions using CGSENSE are 16 and 9.18, respectively. Both the performance measures indicate the superiority of CRAUNN over CGSENSE.

In the proposed method, variable density sampling is utilized, where the low k-space is densely sampled and the high k-space is sparsely sampled. Dense sampling of low

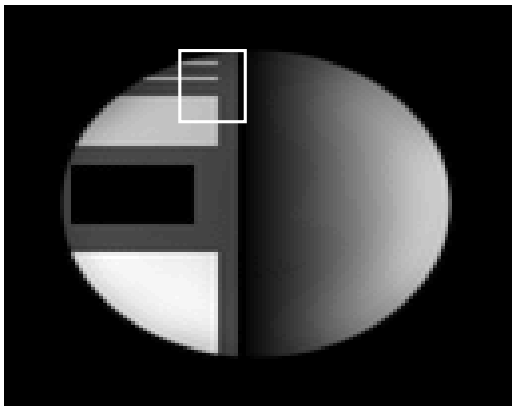

(a)

(b) (c) (d)

Figure 5.12: Comparison of details in the reconstructed images of a synthetic phantom. (a) Original phantom image. The detail being observed is marked by a rectangle (radial data used is undersampled by 6). (b) Detail in the original image. (c) Detail in the direct reconstruction. (d) Detail in the reconstruction using CRAUNN.

k-space leads to alias-free images required for the training phase of the system. It is necessary to check if the disk in the k-space that is densely sampled can be reduced in size, so as to affect more savings in time. An experiment was carried out where the low k-space area that is densely sampled, is reduced to half the size. Fig. 5.14 shows that the resulting images, in this case, are blurred. This is because, using very low frequency acquisitions for training the neural network, teaches the network to yield smoothened images. The fine features in the image do not get registered with the network, thus leading to blurring artifacts in the reconstructed image. The neural network topology, learning parameters and feature vectors used, have been the same all through, for the different sampling trajectories used. Since the number of feature vectors is equal to the number of pixels in the image, each feature vector being independent of all others, the

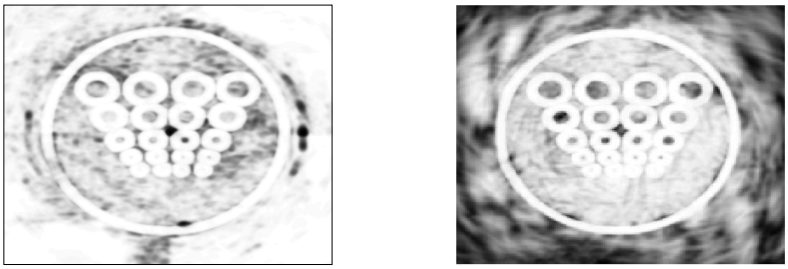

(a) (b)

Figure 5.13: Comparison of SSIM indices for reconstruction of the phantom shown in Fig. 5.7 using (a) CRAUNN [0-1] (b) CGSENSE [0-1]

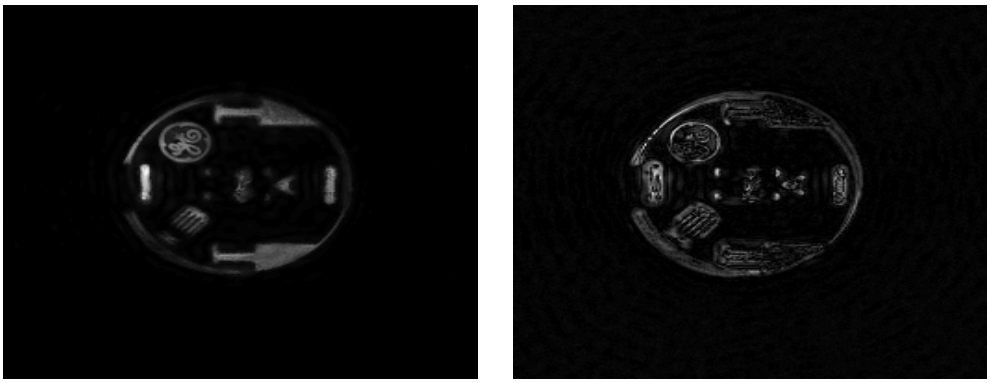

(a) (b)

Figure 5.14: Reconstruction using reduced low k-space acquisition for training (Spiral data used in Fig. 5.4 undersampled by 4). (a) Reconstructed image [0-255]. (b) Corresponding error image [0-70].

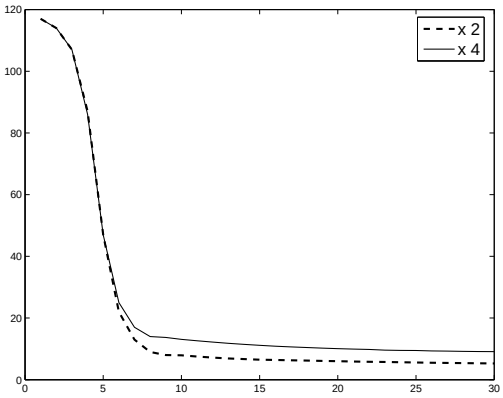

Figure 5.15: Typical plot of training error (along Y-axis) vs. number of iterations (along X-axis), observed for different acceleration factors.

image was cut into four equal quarters. Four identical neural networks were used, one for each of the quarters, whose input vectors were now $(1/4)^{th}$ of the total number of feature vectors. This approach results in faster processing, parallelizing the process. It must be noted however, that parallelizing the problem does not lead to results different from the situation when only one NN is used in place of 4.

As in the Cartesian case, here too, it is hard to predict the nature of artifacts that might appear in the reconstructed images. The training phase needs about hundred iterations to converge to an error of $(1/100)^{th}$ of the maximum intensity. For larger acceleration factors, the reconstruction errors are larger. One of the reasons is that the training error itself saturates at a higher value for larger acceleration factors, as shown in the plots in Fig.5.15. The plot shows that the training error at acceleration factor 2 saturates at a much lower value than that at acceleration factor 4.

5.7 Conclusions

We have proposed a neural network framework to reconstruct images for non-Cartesian parallel magnetic resonance imaging. Here, the observations about the nature of artifacts being similar irrespective of whether the acquisition contains low frequencies alone, or include higher frequencies too, is exploited. Images obtained using low k-space frequencies

are used to learn the model needed for image reconstructions using the entire range of k-space frequencies. The proposed method is demonstrated to work well for spiral and radial trajectories. The proposed method can be applied to arbitrary trajectories in general. No assumptions are made about the transformation that is sought. Acceleration factors up to 6 are achieved with radial trajectories, while spiral trajectories result in acceleration factor up to 4.

5.8 Acknowledgements

We would like to acknowledge the efforts of the group at Harvard University that put up valuable resources on the web-site [5]. We have utilized the code for CGSENSE applicable to Cartesian trajectories from the resources made available at their web-site. For image reconstruction using data sampled along spiral and radial trajectories, routines for density compensation and re-gridding had to be added to the existing code.

We also acknowledge Wang and Bovik of Texas Austin University for making their papers and codes available on the website [4]. We have utilized their SSIM code.

Chapter 6

Conclusion

The focus of this thesis is to obtain high-quality MR images using reduced data, technically called "Rapid MR Imaging". The term "rapid" is used because acquiring less volume of data results in faster scans. Rapid MR imaging is employed to study the dynamics of organs. Such studies require a time-series of images to be acquired with adequate spatial and temporal resolutions. In order to achieve this, strategies are proposed for image reconstruction with reduced data, in the context of conventional as well as parallel MR scanners. The factor by which data acquisition can be reduced, without compromising the image quality is called "acceleration factor". One would look for techniques that result in higher acceleration factors.

Reduced data acquisition in conventional (sequential) MR scanners, where a single homogeneous receiver coil is used for data acquisition, can be achieved either by acquiring only certain k-space regions using suitable data truncation windows or by regularly undersampling the entire data in k-space. In chapter 2, the former approach is explored, where the issues involved are selection of the optimal sampling region in k-space followed by estimation of unacquired samples. A novel star-shaped truncation window is proposed to increase the achievable acceleration factor. The proposed window monotonically cuts down the number of low energy k-space samples acquired. The truncation window samples data within a star-shaped region centered around the origin in the $k_y - k_z$ plane. The

missing values are extrapolated using generalized series modeling-based method. The proposed method is applied to several real and synthetic data sets. The superior performance of the proposed method is illustrated using the standard measures of error images and uptake curve comparisons. Average values of slope error in estimating the enhancement curve are obtained over 5 real data sets of breast and abdomen images, for an acceleration factor of 8. The proposed method results in a slope error of 5%, while the values obtained using rectangular and elliptical windows are 12% and 10%, respectively.

In dynamic imaging methods, where regular undersampling is used, aliasing needs to be corrected, to obtain good-quality images. The technique to undo aliasing needs to be chosen with care to ensure that no residual aliasing remains. *k-t BLAST*, a popular method used in cardiac and functional brain imaging, is investigated and improvements are proposed in chapter 3. *k-t BLAST* suffers from drawbacks such as separate training scan, blurred training estimates and aliased phase maps. To overcome these drawbacks, the proposed improved *k-t BLAST* incorporates variable-density sampling scheme, phase information from the training map and utilization of generalized-series extrapolated training map. The advantage of using a variable density sampling scheme is that the training map is obtained from the actual acquisition instead of a separate pilot scan. Besides, phase information from the training map is used, in place of phase from the aliased map; generalized series extrapolated training map is used instead of the zero-padded training map, leading to better estimation of the unacquired values. The existing technique and the proposed variations are applied on real fMRI data volumes. Improvement in PSNR of activation maps of up to 10 dB is observed. Besides, RMSE reduction of 10% is obtained over the entire time series of fMRI images. The peak improvement of the proposed method over *k-t BLAST* is 35%, averaged over 5 data sets.

Another way to achieve rapid imaging is to use parallel MR scanners, where multiple receiver coils are used to acquire data. Parallel MR scanners achieve better SNR and greater acceleration factor. Reduced data acquisition is accomplished using regular undersampling, which introduces aliasing in images. The existing image reconstruction techniques in parallel MR imaging mainly differ in their approach to unaliasing, which

could be carried out either in the image domain or k-space domain or both. Image reconstruction techniques also vary with the sampling trajectory utilized for data acquisition. Although Cartesian trajectories are the simplest to handle, non-Cartesian trajectories such as radial and spiral, are being explored for their inherent advantages such as robustness to motion and relatively denser sampling of the high-energy low k-space.

Most techniques in parallel MR imaging utilize the knowledge of coil sensitivities along with assumptions of image reconstruction functions. In chapter 4, a new technique (CRAUNN) is proposed that neither needs to estimate coil sensitivities nor makes any assumptions on the image reconstruction function. The proposed Cartesian parallel imaging is a novel approach based on the observation that the aliasing patterns remain the same irrespective of whether the k-space acquisition consists of only low frequencies or the entire range of k-space frequencies.

Data acquisition follows a variable-density sampling scheme, where low k-space frequencies are densely sampled, while the rest of the k-space is sparsely sampled. The blurred, unaliased images obtained using the densely sampled low k-space data are used to train the neural network. Image reconstruction is carried out by feeding the aliased images, obtained using the regularly undersampled k-space containing the entire range of k-space frequencies, to the trained network. The proposed approach has been applied to the Shepp-Logan phantom as well as real brain MRI data sets. A visual error measure for image quality estimation in compression literature, called SSIM (Structural SIMilarity) index is employed. This measure is not used for the works discussed in the preceding chapters, because they deal with a sequence of images. The assessment of the reconstructed time series is carried out using measures relevant to the given context.

The average SSIM for the noisy Shepp-Logan phantom (SNR = 10 dB) using CRAUNN is 0.68, while those obtained using GRAPPA and SENSE are 0.6 and 0.42, respectively. For the case of the phantom superimposed with fine grid-like structure, the average SSIM index obtained with CRAUNN is 0.7, while those for GRAPPA and SENSE are 0.5 and 0.37, respectively.

Image reconstruction is more challenging with reduced data acquired using non-Cartesian

trajectories since aliasing introduced is not localized. A popular technique for non-Cartesian parallel imaging, CGSENSE, suffers from drawbacks like sensitivity to noise and requirement of good coil estimates, while radial/spiral GRAPPA requires complete identical scans to obtain reconstruction kernels for specific trajectories. In chapter 5, the proposed CRAUNN method has been shown to work for general non-Cartesian acquisitions such as spiral and radial too. In addition, the proposed method does not require coil estimates, or trajectory-specific customized reconstruction kernels.

Experiments are performed using radial and spiral trajectories on real and synthetic data, and the results are compared with those of CGSENSE. Comparison of error images shows that the proposed method has lesser residual aliasing than CGSENSE. The average SSIM index for reconstructions using CRAUNN with spirally and radially undersampled data, are comparable at 0.83 and 0.87, respectively. The same measure for reconstructions using CGSENSE are 0.67 and 0.69, respectively. The average RMSE for reconstructions using CRAUNN with spirally and radially undersampled data, are 11.1 and 6.1, respectively. The same measure for reconstructions using CGSENSE are 16 and 9.2, respectively.

List of symbols and acronyms

B_0	:	Homogeneous magnetic field
B_1	:	RF magnetic field
M	:	Induced magnetization vector
ω_0	:	Larmor frequency
h	:	Planck's constant
γ	:	Gyromagnetic constant
m	:	Number of magnetic spins
s	:	MR signal
t	:	Time instant
f	:	Temporal frequency
k	:	Spatial frequency (space of MR data acquisition)
(k_x, k_y, k_z)	:	Spatial frequencies along spatial axes X,Y and Z
W	:	Maximum sampling width in k-space
δ	:	Spatial resolution obtained in MR image
k_{max}	:	Maximum extent of the spatial frequency sampled
d	:	Data acquired in k-space
I	:	MR Image
G	:	Gradient magnetic field
k-t	:	Temporally changing k-space.
ρ	:	Complex value at a given location in the y-f space
C	:	Complex coil sensitivity profile
S_l	:	Image obtained at l_{th} coil
S_{l_A}	:	Aliased image obtained at l_{th} coil
S	:	True image
$\hat{S}$	:	Estimated value of S

$\mathcal{F}$	:	Function estimated by neural network to combine aliased coil images to generate the alias-free composite image
U	:	Feature vector input to the neural network
w	:	Connection weights between input and hidden layers
v	:	Connection weights between hidden and output layer
f_a	:	Sigmoidal activation function
T	:	Obtained output of the neural network
$\hat{T}$	:	Target output of the neural network
E	:	Training error of the neural network
BLAST	:	Broad-Use Linear Acquisition Speed-up Technique
BURS	:	Block Uniform ReSampling
CGSENSE	:	Conjugate Gradient Sensitivity Encoding
CRAUNN	:	Composite image Reconstruction And Unaliasing using Neural Networks
DCE-MRI	:	Dynamic Contrast Enhanced MRI
ELL	:	Elliptical Shaped Window
fMRI	:	Functional MRI
FOV	:	Field of View
GRAPPA	:	Generalized autocalibrating partially parallel acquisitions
GeS	:	Generalized Series
GS	:	Gaussian Shaped window
ktB	:	kt-BLAST
ktB-Ph	:	kt-Blast with Phase Constraints
ktB-R	:	kt-Blast with RIGR-Extrapolated Training Map
ktB-PR	:	kt-Blast with Phase Constraints and RIGR-Extrapolated Training Map
MLP	:	Multi Layer Perceptron
MRI	:	Magnetic Resonance Imaging
NN	:	Neural Networks
PILS	:	Partially Parallel Imaging with Localized Sensitivities

PSF : Point Spread Function

PSNR : Peak Signal to Noise Ratio

RIGR : Reduced encoding Imaging by Generalized series Reconstruction

RMSE : Root Mean Square Error

ROI : Region of Interest

RS : Rectangular Shaped window

SENSE : Sensitivity Encoding

SMASH : Simultaneous Acquisition of Spatial Harmonics

SNR : Signal to Noise Ratio

SPM : Statistical Parametric Mapping

SoS : Sum of Squares

SS : Star Shaped window

SSIM : Structural Similarity

TRIGR : Two-reference RIGR

Publications related to thesis

1. Neelam Sinha, Manojkumar Saranathan, K.R.Ramakrishnan and S. Suresh, " Parallel Magnetic Resonance Imaging using Neural Networks" in the 14th IEEE International Conference on Image Processing (ICIP) , Vol. 3, pages 149-152, Texas, U. S. A., 2007.

2. N. Sinha, S. Jana and Manojkumar Saranathan " A neural network approach for non-Cartesian k-space parallel imaging reconstruction", in the Joint ISMRM-ESMRMB meet at Berlin, page 336, Germany, 2007.

3. Neelam Sinha, Manojkumar Saranathan, A.G.Ramakrishnan, Juan Zhou, and Jagath C. Rajapakse, "Ultra-Fast fMRI Imaging with High-Fidelity Activation Map ", in the Proceedings of 13th International Conference on Neural Information Processing (ICONIP) 2006 held at Hong Kong, Part 2, LNCS 4233, pages 361-368

4. Neelam Sinha and Manojkumar Saranathan, "Improved generalized series reconstruction for 3D MRI using shaped data", in the Proceedings of 14th International Society for Magnetic Resonance in Medicine (ISMRM) 2006, Seattle, Washington, page 373, USA.

5. Neelam Sinha, Manojkumar Saranathan and A. G. Ramakrishnan, "Generalized series model-based 3D reconstruction for dynamic magnetic resonance imaging", in Proceedings of European Society for Magnetic resonance in Medicine and Biology (ESMRMB) 2005, Basel, page 341, Switzerland.

6. Neelam Sinha, A. G. Ramakrishnan and Manojkumar Saranathan, "Composite MR image reconstruction and unaliasing for general trajectories using Neural Networks", submitted to IEEE Transactions on Medical Imaging.

References

[1] Scanner Image : http://www.imaginginformatics.ca.

[2] SENSE, GRAPPA codes and brain data :
http://www.ece.tamu.edu/~mrsl/JIMJI_TAMU/pulsarweb/index.htm.

[3] Table of typical values of MR constants :
http://www.lems.brown.edu/~msj/cs292/assign2/mr.html.

[4] SSIM code :
http://www.ece.uwaterloo.ca/~z70wang/research/ssim.

[5] CG-SENSE code:
http://www.nmr.mgh.harvard.edu/~fhlin/tool_sense.htm.

[6] P. Bornert, H. Schomberg, B. Aldefeld, and J. Groen. Improvements in spiral MR imaging. *MAGMA*, 9:29–41, 1999.

[7] R. Boubertakh, N. M. Noble, S. R. Hegde, D. L. Hill, and R. S. Razavi. Automatic training for k-t BLAST reconstruction. *Proceedings of 13th ISMRM*, page 2439, 2005.

[8] Felix Breuer. *Application of Efficient Strategies for Parallel Magnetic Resonance Imaging.* PhD thesis, Wurzburg University, 2006.

[9] K. J. Friston and A. P. Holmes. Statistical parametric maps in functional imaging: A general linear approach. *Human Brain Mapping*, 2:189–210, 1995.

[10] H. G. Glover. Simple analytic spiral k-space algorithm. *Magnetic Resonance in Medicine*, 42:412–415, 1999.

[11] M. A. Griswold, R. M. Heidemann, and P. M. Jakob. Direct parallel imaging reconstruction of radially sampled data using GRAPPA with relative shifts. *Proceedings of 11th ISMRM*, page 2349, 2003.

[12] M. A. Griswold, P. M. Jakob, R. M. Hedemann, M. Nittka, V. Jellus, J. Wang, B. Keifer, and A. Haase. Generalized autocalibrating partially parallel acquisitions (GRAPPA). *Magnetic Resonance in Medicine*, 47(6):1202–1210, 2002.

[13] M. A. Griswold, P.M. Jakob, R. M. Hedemann, and A. Haase. Parallel imaging with localized sensitivities (PILS). *Magnetic Resonance in Medicine*, 44(4):602–609, 2000.

[14] H. Moriguchi H and J. L. Duerk. Modified block uniform resampling (BURS) algorithm using truncated singular value decomposition: fast accurate gridding with noise and artifact reduction. *Magnetic Resonance in Medicine*, 46:1189–1201, 2001.

[15] Michael S. Hansen, Sebastian Kozerk, Klaas P. Pruessmann, Peter Boesiger, Erik M. Pedersen, and Jeffrey Tsao. On the influence of training data quality in k-t BLAST reconstruction. *Magnetic Resonance in Medicine*, 52:1175–1183, 2004.

[16] K. A. Heberlein, Y. Kadah, and X. Hu. Segmented spiral parallel imaging using GRAPPA. *Proceedings of 12th ISMRM*, page 328, 2004.

[17] Keith Heberlein and Xiaoping Hu. Self-calibrated parallel imaging using dual-density spirals. *Proceedings of 2nd International Workshop on Parallel MRI*, page 59, 2005.

[18] Keith Heberlein and Xiaoping Hu. Auto-calibrated parallel spiral imaging. *Magnetic Resonance in Medicine*, 55:619–625, 2006.

[19] R. Edward Hendrick. Breast MRI: Using physics to maximize its sensitivity and specificity to breast cancer. Technical report, Northwestern University Feinberg School of

Medicine, 2004. 46th The American Association of Physicists in Medicine (AAPM) Annual Meeting.

[20] R. D. Hoge, R. K. S. Kwan, and G. B. Pike. Density compensation functions for spiral MRI. *Magnetic Resonance in Medicine*, 38:117–120, 1997.

[21] W. S. Hoge. *An Adaptive Signal Processing Approach to Dynamic Magnetic Resonance Imaging*. PhD thesis, Northeastern University, Boston, 2001.

[22] P. Hu and C. H. Meyer. BOSCO: Parallel image reconstruction based on successive convolution operations. *Proceedings of 14th ISMRM*, page 751, 2006.

[23] M. Hutchinson and U. Raff. Fast MRI data acquisition using multiple detectors. *Magnetic Resonance in Medicine*, 6(1):87–91, 1998.

[24] Z. P Liang J. M. Hanson, E. C. Wiener, and P. C. Lauterbur. Fast dynamic imaging using two reference images. *Magnetic Resonance in Medicine*, 36:172–175, 1996.

[25] J. J. Jackson, C. H. Meyer, D. G. Nishimura, and A. Macovski. Selection of a convolution function for Fourier inversion using gridding. *IEEE Transactions of Medical Imaging*, 10(3):473–478, 1991.

[26] P. M. Jakob, M. A. Griswold, R. R. Edelman, and D. K. Sodickson. AUTOSMASH : A self-calibrating technique for SMASH imaging. simultaneous acquisition of spatial harmonics. *MAGMA*, 7:42–54, 1998.

[27] Peter Kellman. Parallel imaging : The basics. ISMRM 2004 Presentation.

[28] T. Kidane, T. P. Eagan, Y. C. Cheng, T. N. Baig, V. Taracila, and R. W. Brown. Matrix regularization for SENSE imaging. *Magnetic Resonance in Medicine*, 46:638–651, 2003.

[29] F. R. Korosec, R. Frayne, T. M. Grist, and C. A. Mistretta. Time-resolved contrast-enhanced 3d MR angiography. *Magnetic Resonance in Medicine*, 36:345–351, 1996.

[30] S. Kozerke, J. Tsao, R. Hoogeveen, J. Puginier, P. Boesiger, and K. U. Wentz. Accelerating time-resolved 3D contrast-enhanced angiography using k-t BLAST. *Proceedings of 13th ISMRM*, page 382, 2005.

[31] Sebastian Kozerke, Jeffrey Tsao, Reza Razavi, and Peter Boesiger. Accelerating cardiac cine 3D imaging using k-t BLAST. *Magnetic Resonance in Medicine*, 52:19–26, 2004.

[32] Sumati Krishnan. *K-Space Acquisition Method for Dynamic Contrast-Enhanced MRI: Application to Breast Tumors*. PhD thesis, University of Michigan, 2004.

[33] Y. Kurihara, Y. K. Yakuushiji, I. Tani, Y. Nakajima, and M. V. Cauteren. Coil sensitivity encoding in MR imaging : Advantages and disadvantages in clinical practice. *American Journal of Roentgenology*, 178:1087–1091, 2002.

[34] W. E. Kyriakos, L. P. Panych, D. F. Kacher, C. F. Westin, S. M. Bao, R. V. Mulkern, and F. A. Jolesz. Sensitivity profiles from an array of coils for encoding and reconstruction in parallel (SPACERIP). *Magnetic Resonance in Medicine*, 44:301–308, 2000.

[35] E. G. Larsson, D. Erdogmus, R. Yan, and J. C. Principe. SNR-optimality of sum-of-squares reconstruction for phased-array magnetic resonance imaging. *Journal of Magnetic Resonance*, 163:121–123, 2003.

[36] Sangwoo Lee. *Iterative reconstruction methods for rosette trajectories in functional MRI*. PhD thesis, The University of Michigan, 2006.

[37] Z. P. Liang. Generalized series dynamic imaging. *Proceedings of International Workshop on Medical Imaging and Augmented Reality*, pages 145–151, 2001.

[38] Z. P. Liang, H. Jiang, C. P. Hess, and P. C. Lauterbur. Dynamic imaging by model estimation (DIME). *International Journal of Imaging Systems and Technology*, 8:551–557, 1997.

[39] Z. P. Liang and P. C. Lauterbur. An efficient method for dynamic Magnetic Resonance Imaging. *IEEE Transactions on Medical Imaging*, 13(4):677–686, 1994.

[40] Z. P. Liang, Bruno Madore, Gary H. Glover, and Norbert J. Pelc. Fast algorithms for GS-model-based image reconstruction in data-sharing Fourier imaging. *IEEE Transactions on Medical Imaging*, 22(8):1026–1030, 2003.

[41] F. Lin, K. K. Kwong, J. W. Belliveau, and L. L. Wald. Parallel imaging reconstruction using automatic regularization. *Magnetic Resonance in Medicine*, 51:559–567, 2004.

[42] B. Madore, G. H. Glover, and N. J. Pelc. Unaliasing by Fourier-encoding the overlaps using the temporal dimension (UNFOLD), applied to cardiac imaging and fMRI. *Magnetic Resonance in Medicine*, 42:813–828, 1999.

[43] N. Mistry, J. Pollaro, J. Song, and G. A. Johnson. Interleaved radial imaging with sliding window-keyhole reconstruction to image pulmonary perfusion in rats. *ISMRM Workshop on Non-Cartesian Imaging*, 2007.

[44] D. G. Nishimura. *Principles of Magnetic Resonance Imaging*. Stanford University, 1996.

[45] D. C. Noll, S. J. Peltier, and F. E. Boada. Simultaneous multislice acquisition using rosette trajectories (SMART): A new imaging method for functional MRI. *Magnetic Resonance in Medicine*, 39:709–716, 1998.

[46] T. Parrish and X. Hu. Continuous update with random encoding (CURE): A new strategy for dynamic imaging. *Magnetic Resonance in Medicine*, 33:326–336, 1995.

[47] Jan Petr, Jan Kybic, Vaclav Hlavac, Sven Muller, and Michael Bock. Fast parallel MRI reconstruction using B-spline approximation (PROBER). *SPIE Proceedings of Medical Imaging*, 6142:1251–1262, 2006.

[48] Jan Petr, Jan Kybic, Sven Muller, Vaclav Hlavac, and Michael Bock. Parallel MRI

reconstruction using B-spline approximation. *Proceedings of 13th ISMRM*, page 2421, 2005.

[49] J. G. Pipe and P. Menon. Sampling density compensation in MRI: rationale and an iterative numerical solution. *Magnetic Resonance in Medicine*, 41:179–186, 1999.

[50] K. P. Pruessmann, M. Weiger, P. Bornert, and P. Boesiger. Advances in sensitivity encoding with arbitrary k-space trajectories. *Magnetic Resonance in Medicine*, 46:638–651, 2001.

[51] K. P. Pruessmann, M. Weiger, M. B. Scheidegger, and P. Boesiger. SENSE : Sensitivity encoding for fast MRI. *Magnetic Resonance in Medicine*, 42:952–962, 1999.

[52] Y. Qian, Z. Zhang, V. A. Stenger, and Y. Wang. Self-calibrated spiral sense. *Magnetic Resonance in Medicine*, (3):688–692, 2004.

[53] J. B. Ra and C. Y. Rim. Fast imaging using subencoding data sets from multiple detectors. *Magnetic Resonance in Medicine*, 30:142–145, 1993.

[54] S. D. Rane. Parallel magnetic resonance imaging: Characterization and comparison. Master's thesis, Texas A M University, 2005.

[55] V. Rasche, R. Proksa, R. Sinkus, P. Bornert, and H. Eggers. Resampling of data between arbitrary grids using convolution interpolation. *IEEE Transactions in Medical Imaging*, 18:385–392, 1999.

[56] P. B. Roemer and W. A. Edelstein. The NMR phased array. *Magnetic Resonance in Medicine*, 16(2):195–225, 1990.

[57] D. E. Rumelhart, G. E. Hinton, and R. J. Williams. Learning representations by back-propagating errors. *Nature*, 323:533–536, 1986.

[58] T. L. Chenevert S. Krishnan. Spatio-temporal bandwidth-based acquisition for dynamic contrast-enhanced magnetic resonance imaging. *Journal of Magnetic Resonance Imaging*, 20(1):129–137, 2004.

[59] K. A. Salem and D. L. Wilson. A human vision model for the objective evaluation of perceived image quality applied to MRI and image restoration. *Proceedings of SPIE*, 4791:180–191, 2002.

[60] A. A. Samsonov, G. Eugene, Kholmovski, L. Dennis, Parker, and C. R. Johnson. POCSENSE:POCS-based reconstruction for sensitivity encoded magnetic resonance imaging. *Magnetic Resonance in Medicine*, (6):1397–1406, 2004.

[61] J. Sandeep. Reconstruction techniques for non-cartesian acquisitions in MRI. Master's thesis, Department of Electrical Engineering, Indisn Institute of Science, Bangalore, India, 2007.

[62] S. K. Shripad. Dynamic contrast-enhanced magnetic resonance imaging. Master's thesis, Department of Electrical Engineering, Indisn Institute of Science, Bangalore, India, 2004.

[63] J. Sngas, T. Knopp, and H. Eggers. dSENSE: direct k-space reconstruction for non-cartesian parallel MR imaging. *Proceedings of 14th ISMRM*, page 3652, 2006.

[64] D. K. Sodickson and W. J. Manning. Simultaneous acquisition of spatial harmonics (SMASH): ultra-fast imaging with radio frequency coil arrays. *Magnetic Resonance in Medicine*, 38(4):591–603, 1997.

[65] Y. Sun, D. Yang, Q. Ye, M. Williams, J. M.F. Moura, F. Boada, Z. P. Liang, and C. Ho. Improving spatiotemporal resolution of USPIO-enhanced dynamic imaging of rat kidneys. *Magnetic Resonance Imaging*, 21:593–598, 1994.

[66] Chi-Ming Tsai and Dwight G. Nishimura. Reduced aliasing artifacts using variable-density k-space sampling trajectories. *Magnetic Resonance in Medicine*, 43:452–458, 2000.

[67] Jeffrey Tsao, Peter Boesiger, and Klaas P. Pruessmann. k-t BLAST and k-t SENSE: Dynamic MRI with high frame rate exploiting spatiotemporal correlations. *Magnetic Resonance in Medicine*, 50:1031–1042, 2003.

[68] J. J. van Vaals. Keyhole method for accelerating imaging of contrast uptake. *Journal of Magnetic Resonance Imaging*, 3:671–675, 1993.

[69] F.T.A.W. Wajer. *Non-Cartesian MRI Scan Time Reduction through Sparse Sampling*. PhD thesis, Delft University of Technology, 2001.

[70] Z. Wang, A. C. Bovik, H. R. Sheik, and E. P. Simoncelli. Image quality assessment: from error measurement to structural similarity. *IEEE Transactions on Image Processing*, 13(4):600–612, April 2004.

[71] Z. Wang, H. R. Sheikh, and A. C. Bovik. No-reference perceptual quality assessment of JPEG compressed images. In *Proceedings of the IEEE International Conference on Image Processing*, volume 1, pages 477–480, September 2002.

[72] M. J. White, M. Bourgeois, D. M. Koh, A. Degenhard, L. Moore, D. Collins, and M. O. Leach. Rapid dynamic contrast-enhanced MRI using reduced acquisition and constrained reconstruction: pilot work for dynamic liver study. *Proceedings of Medical Image Understanding and Analysis (MIUA)*, pages 37–40, 2002.

[73] Qing-San Xiang and R. Mark Henkelman. K-space description for MR imaging of dynamic objects. *Magnetic Resonance in Medicine*, 29:422–428, 1993.

[74] E. Yeh, M. Stuber, C. McKenzie, R. Botnar, T. Leiner, M. Ohliger, A. Grant, J. W. Onwuachi, and D. K. Sodickson. Inherently self-calibrating non-cartesian parallel imaging. *Magnetic Resonance in Medicine*, (1):1–8, 2005.

[75] E. N. Yeh, C. A. McKenzie, D. Lim, M. A. Ohliger, A. K. Grant, J. Willig, N. M. Rofsky, and D. K. Sodickson. Parallel imaging with augmented radius in k-space (PARS). *Proceedings of 10th ISMRM*, page 2399, 2002.

[76] H. R. Sheikh Z. Wang, A. C. Bovik and E. P. Simoncelli. Image quality assessment: From error visibility to structural similarity. *IEEE Transactions on Image Processing*, 13(4):600–612, 2004.

[77] T. Zhang. Statistical behavior and consistency of classification methods based on convex risk minimization. *Annals of Statistics*, 32(1):56–85, 2004.